Magnetization reversal mechanism in strongly exchange-coupled double layers of Co/Pt and TbFe

Inauguraldissertation

zur

Erlangung der Würde eines Doktors der Philosophie
vorgelegt der
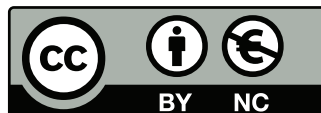Philosophisch-Naturwissenschaftlichen Fakultät
der Universität Basel
von

Xue Zhao

aus China

Basel, 2018

Genehmigt von der Philosophisch-Naturwissenschaftlichen Fakultät
auf Antrag von

Prof. Dr. Hans J. Hug

Prof. Dr. Manfred Albrecht

Basel, den 17 Oktober 2017

Prof. Dr. Martin Spiess, Dekan

Dedication

To my parents Jianhua and Liping, my husband Zhao, and my son Chuanshuo

– for all of their love.

Acknowledgments

I would first like to thank my supervisors Dr. Miguel A. Marioni and Prof. Dr. Hans J. Hug for their support and guidance throughout the past years, and also for giving me the opportunity to work on challenging projects from both the scientific and instrumentation perspectives. The insightful discussions have inspired me to learn more about physics.

I would like to thank all my colleagues at EMPA for contributing to the great atmosphere in the lab, as well as in the coffee room. Many thanks go to Dr. Manfred Parschau, Dr. Marcos Penedo, Sasa Vrankovic and Günther Hobi for helping me assemble the LT-MFM instrument at the initial phase of my PhD. My special thanks go to Dr. Johannes Schwenk for all the work we have accomplished together in the lab, from whom I've learned a whole lot about lab physics. I also would like to thank Dr. Andra O. Mandru for her useful tips in scientific presentations and writing.

Last but not least, I would like thank my parents who supported my studies abroad. I also would like to thank my husband Zhao and my son Chuanshuo. This dissertation would never have been possible without your love and support.

4

Table of contents

1   Introduction

Since the pioneering work in rare earth-transition metal (RE-TM) by Mimura et al. [1] and K.H.J. Buschow et al. [2], amorphous TbFe ferrimagnets and other rare earth-transition metal (RE-TM) films gained attention for their strong perpendicular magnetic anisotropy (PMA) and good magneto-optical properties [3] [4] [5]. Recently, the development of all-optical switching has triggered a renewed interest in rare earth-ferrimagnets. For example, Radu et al. reported X-ray Magnetic Circular Dichroism (XMCD) measurements that probe the optically excited non-equilibrium spin dynamics on nanometre length scales and femtosecond timescales in GdFeCo [6]. Liu et al. demonstrated that single femto-second optical laser pulses of sufficient intensity were able to reproducibly reverse the magnetization in TbFeCo thin films, which can be a model system for all-optical switching-based recording technologies [7].

The focus of my thesis is on the study of the RE-TM ferrimagnet Tb_xFe_y thin films and the ferri/ferro-magnet $Tb_xFe_y/[Co/Pt]_{\times n}$ exchange-coupled systems, where x and y designate the atomic ratio of Tb and Fe, and n designate the number of [Co/Pt] bi-layers in the multilayer. These exchange-coupled double-layer structures have many potential applications, e.g. as candidate systems for a hard RE-TM storage layer coupled to a softer read/write layer for heat-assisted magnetic recording (HAMR). The details of the exchange-coupling and the magnetization reversal mechanism are not fully studied and understood in this strong coupling regime. This thesis is a first study of these systems with high spatial resolution to understand the physics that determines the reversal.

The samples were fabricated using DC magnetron sputtering at room temperature under ultra high vacuum (UHV) conditions. For the imaging of the stray

fields emanating from a sample surface and the magnetization reversal of magnetic thin films, magnetic force microscope (MFM) is the technique of choice since it probes the local stray field of materials with high spatial resolution and in applied magnetic fields [8]. Therefore MFM is used as a main technique in my work to investigate the micro-magnetic state of the sample.

An outline of this thesis is given below, with each chapter giving a short overview providing the necessary context.

Chapter 2 provides an introduction to the principles of MFM. For the quantitative analysis and modeling of MFM data, a transfer function relating the MFM contrast to the stray field emanating from the sample surface is necessary. It is obtained through the tip calibration procedures. Our MFM instrumentation and the important aspects of sample and probe preparation and handling are discussed as well.

The measured MFM magnetic contrast arises from the magnetic forces between tip and sample, due to the stray field emanating from the sample surface. The stray field decays rapidly with increasing distance from the surface. In order to obtain high resolution MFM images and the subsequent quantitative analysis, the magnetic tip needs to scan very close to the sample surface and be kept at a constant (average) distance during image scan even in a large applied magnetic field. Therefore, a robust method for active tip-sample distance control based on frequency modulation of the cantilever oscillation has been developed. With this method, a tip-sample distance of the order of 10 nm can be controlled with a precision better than ± 0.4 nm. This frequency-modulated capacitive tip-sample distance control method is presented in Chapter 3.

Chapter 4 presents the results for the study of TbFe thin films. The magneti-

zation reversal was studied by MFM measurements, and the magnetization loops measured by vibrating sample magnetometry (VSM) and superconducting quantum interference device (SQUID) magnetometry. The MFM-scans were performed at $10.5\,\mathrm{K}$ and in external magnetic fields ranging from 0 to $7\,\mathrm{T}$, at a constant average tip sample distance of $7\,\mathrm{nm}$. The topographical and magnetic contributions in the MFM frequency shift contrast were separated by scanning with up and down tip magnetizations. Magnetic contrast and magnetic pattern evolution as function of field were evaluated for the original and the zoomed MFM images. We used the transfer function to simulate the MFM contrast measured on TbFe thin films. In addition, Rutherford backscattering spectrometry (RBS) and transmission electron microscopy (TEM) were used for composition and chemical analyses of the samples.

The magnetization reversal of exchange-coupled $\mathrm{TbFe}/[\mathrm{Co}/\mathrm{Pt}]_{\times n}$ double layers is addressed in Chapter 5. The magnetometry and MFM measurements, as well as the quantitative MFM data analysis were carried out in a similar way to the TbFe thin films presented in Chapter 4. The reversal processes can be classified into three field regions, e.g. the rotation of $[\mathrm{Co}/\mathrm{Pt}]_{\times n}$ local magnetic moments in low fields, the reversal of $[\mathrm{Co}/\mathrm{Pt}]_{\times n}$ via nucleation of 'sub-domains' accompanied by the formation of interfacial domain walls (iDW) in intermediate fields, and the compression of the iDW in high fields. In addition, $\mathrm{Tb}_x\mathrm{Fe}_y/[\mathrm{Co}/\mathrm{Pt}]_{\times n}$ samples with Pt interlayers exhibit lower exchange-bias field with larger interlayer thickness, showing the possibility of tuning the exchange-coupling by the Pt interlayer.

The above studies attempted to understand the micromagnetic state of the amorphous TbFe alloy thin films and the magnetization reversal of $\mathrm{TbFe}/[\mathrm{Co}/\mathrm{Pt}]_{\times 5}$ based exchange-coupled double-layer structures. Chapter 6 gives a summary of the

presented work and provides an outlook on the envisaged experiments and simulations on the above mentioned systems and methods.

2   Principles and Instrumentation

This chapter gives a short introduction to the principles of MFM, and presents the instrumentation as well as cantilever and sample preparation methods.

2.1   Introduction to magnetic force microscope (MFM)

A magnetic force microscope (MFM) is a type of scanning force microscope (SFM) that is used for the measurement of tip-sample forces mediated by a magnetic field [8]. The MFM utilizes a tip with a magnetic moment so that it becomes sensitive to magnetic fields emanating from a sample of interest.

The pioneering work on MFM dates back to the late 1980s [9, 10, 11, 12, 13, 14], and reviews on MFM can be found in refs. [15, 16, 17] and more recently in [8]. MFM has become one of the most widely used magnetic imaging techniques, especially to image magnetic patterns in magnetic recording media [13, 14].

The measurement of magnetic forces is challenging for various reasons. Like other SFMs, MFM measures the sum of all the forces between the probe (e.g. cantilever, tunning fork) and the sample. Hence an important task in MFM is to separate the magnetic from the non-magnetic forces contributing to the measured signal. Due to the small magnitude of the magnetic force and its decay with increasing distance from the sample, measuring close to the sample surface improves the signal to noise ratio. At the same time, the probe should not get so close to the sample surface that spatial variations of the van der Waals forces dominate the measured signal. A constant average tip-sample distance between about 5 and 20 nm needs to be maintained. These requirements imply the need for an accurate tip sample distance control. Two methods have recently been developed [18, 19]

but are found to be inadequate for the measurement conditions (e.g. applied fields up to $7\,\mathrm{T}$) that we encounter in our experiments. To overcome this difficulty, we developed a new single-passage capacitive tip-sample distance control method which is presented in Chapter 3.

2.1.1 Magnetic force microscope (MFM) contrast formation

2.1.1.1 Forces acting on MFM tip

The signal measured by MFM arises from the sum of all forces acting on the MFM tip:

$$F_{\mathrm{ts}} = F_{\mathrm{cap}} + F_{\mathrm{vdW}} + F_{\mathrm{mag}}, \tag{2.1}$$

where F_{cap} represents the capacitive forces, F_{vdW} the van der Waals forces and F_{mag} the magnetic forces.

The *capacitive* or *electric* force F_{cap} is given by the z-derivative of the energy stored in the capacitor (with capacitance C) that is formed by tip and sample (with distance z) [20]:

$$F_{\mathrm{cap}} = -\frac{1}{2}\frac{\partial C}{\partial z}\left(U_{\mathrm{Bias}} - U_{\mathrm{CPD}}\right)^2, \tag{2.2}$$

where U_{Bias} is an externally applied bias potential and U_{CPD} is the contact potential difference (CPD) between tip and sample materials. The capacitive force is always attractive. Note that the overall capacitive force is usually nulled in the measurements by applying a bias equal to the contact potential, but local variations of the topography can still give rise to the frequency shift of the cantilever.

The van der Waals force F_{vdW} between the MFM tip and the sample is described for a conical tip as [21]:

$$F_{\text{vdW}}(z) = -\frac{H}{6}\left(\frac{R}{z^2} + \frac{(\tan\vartheta_0)^2}{z + R'} - \frac{R'}{z(z + R')}\right),\tag{2.3}$$

where R', ϑ_0 are the height and conical angle of the spherical tip apex, and H is an effective Hamaker constant, and z is the tip-sample distance.

The magnetic tip-sample force F_{mag} can be calculated from the tip magnetization $\mathbf{M}_{\text{tip}}(\mathbf{r}, z)$ and the stray field emanating from the sample surface $\mathbf{H}(\mathbf{r}, z)$ [22]:

$$F_{\text{mag}}(\mathbf{r}, z) = \mu_0 \int_{V'} \mathbf{M}_{\text{tip}}(\mathbf{r}', z') \cdot \frac{\partial}{\partial z}\mathbf{H}(\mathbf{r} + \mathbf{r}', z + z')\, d\mathbf{r}' dz'\,,\tag{2.4}$$

with the coordinate vector $\mathbf{r} = (x, y)$, the tip-sample distance z and the vacuum permeability μ_0. The integral is carried out over the tip's volume V' for each position $\mathbf{r}$ of the tip. This makes expression 2.4 inconvenient for the simulation of the measured image contrast. Furthermore, the magnetization distribution of the tip $\mathbf{M}_{\text{tip}}(\mathbf{r}', z')$ is generally not known and not accessible experimentally. For these reasons it is convenient to express the magnetic force in 2D Fourier space with wave vector $\mathbf{k}$ and the coordinate vector in Fourier space $(\mathbf{k}, z) = (k_{\text{x}}, k_{\text{y}}, z)$:

$$\hat{\mathbf{F}}(\mathbf{k}, z) = \mu_0 \int \begin{pmatrix} -ik_{\text{x}} \\ -ik_{\text{y}} \\ \frac{\partial}{\partial z} \end{pmatrix} \hat{\mathbf{M}}_{\text{tip}}^*(\mathbf{k}, z') e^{-\mathbf{k}z'} dz' \cdot \hat{\mathbf{H}}_{\text{sample}}(\mathbf{k}, z),\tag{2.5}$$

where $\hat{\mathbf{M}}_{\text{tip}}^*(\mathbf{k}, z')$ is the complex conjugate of tip magnetization in Fourier space, and $\hat{\mathbf{H}}_{\text{sample}}(\mathbf{k}, z)$ is the stray field in Fourier space. Equation 2.5 expresses the

magnetic force (in 2D Fourier space) as the product of the sample stray field with an unknown tip magnetization integral. This integral is specific to the microscopic magnetic details of the particular tip employed. Determining it therefore requires a measurement, which in essence constitutes the MFM tip calibration procedure that is discussed in more detail in the sections below.

2.1.1.2   Magnetic stray fields

It is convenient to express the sample stray field $\hat{H}$ also in Fourier space. For a film which is uniformly magnetized throughout the film thickness d, the magnetization pattern in Fourier space $\mathbf{M}_z(\mathbf{k})$ determines the stray field above the sample ($z>0$) with

$$\hat{H}(\mathbf{k}, z) = -\frac{1}{2k} \left[e^{-kz} \left(1 - e^{-kd} \right) \right] \begin{pmatrix} ik_x \\ ik_y \\ -k \end{pmatrix} \mathbf{M}_z(\mathbf{k}), \qquad (2.6)$$

where the *distance loss* factor e^{-kz} describes the exponential decay of the magnetic stray field as function of tip-sample distance z, and the *thickness loss* factor $(1 - e^{-kd})$ accounts for the reduction of the stray field arising from the partial compensation from opposite equivalent magnetic charges at the top and bottom surfaces of the magnetic film, which are located at a finite distance d from each other.

For a domain pattern of a $[\text{Co}_{0.6nm}/\text{Pt}_{1.0nm}]_{\times 5}$-multilayer with PMA (see also Section 2.2.1, sample for the tip calibration procedure), the stray field for different distances z above the sample surface is illustrated in Fig. 2.1.

For the thin film sample, the amplitude of the stray field close to the sample surface [Fig. 2.1 a)] is lower in the center of the domains than at the locations of the domain walls. This reflects the influence of the *thickness loss* factor $(1 - e^{-kd})$,
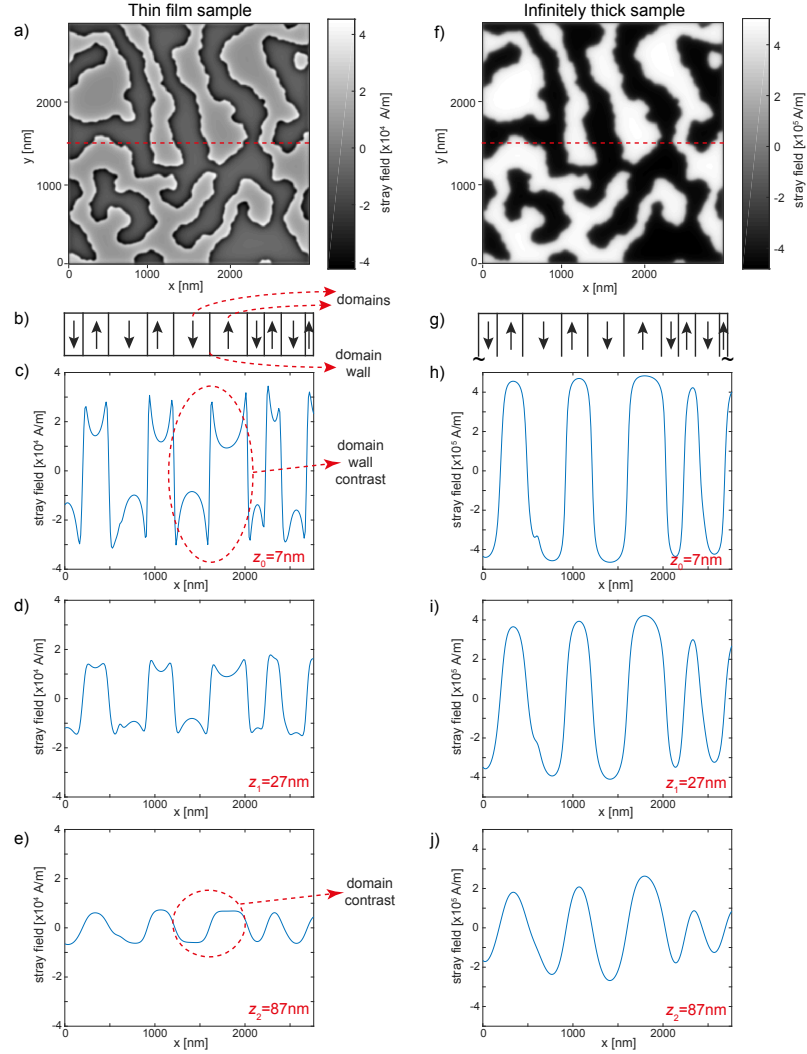
Figure 2.1: Magnetic stray field of a thin sample [panels a)-e)] and an infinitely thick sample [panels f)-j)]. For the two columns of panels: a) and f) Stray field image at a distance of $z_0 = 7\,\text{nm}$ from the thin film and bulk sample, respectively. b) and g) Up and down magnetic domains at the location of the horizontal red lines in image a) and f), respectively. c) and h), d) and i), and e) and j) Profiles of the horizontal red lines in image a) and f) at distances from the sample surface of $z_0 = 7\,\text{nm}$, $z_1 = 27\,\text{nm}$, and $z_2 = 87\,\text{nm}$, respectively. The red dotted ellipses in images c) and e) highlight domain wall contrast and domain contrast, respectively.

which tends to zero with the wavelength tending to infinity. This behavior is well known from the electrostatic field of a uniformly charged plane capacitor, which

is formally equivalent to the limit wavelength case. We refer to the contrast that decreases in amplitude toward the domain center as a *domain wall contrast* type. Conversely, it is said to be more *domain contrast* like if the decrease in contrast amplitude is absent. This case takes place for infinite thickness d or for sufficient distance to the sample (Fig. 2.1). Because of this, the stray field of a saturated film of constant thickness and a homogeneous magnetization vanishes. Figures 2.1 c) to e) show a cross-section of the stray field at the position of the dashed line in Fig. 2.1 a) for different distances z above the surface. The stray field at the location of the domain walls decays faster than that above the domains (e.g. marked in Fig. 2.1 b)), because the *distance loss* factor e^{-kz} decays faster for smaller spatial wavelengths.

For a sample with the same magnetization but infinite thickness [Fig. 2.1 f)-j)], the stray field is high in the center of the domains and low at the locations of the domain walls. This is due to the fact that the *thickness loss* factor $(1 - e^{-kd})$ equals to one for infinitely large d, while the *distance loss* factor e^{-kz} is lower for larger k (smaller wavelength) at the same distance z. Panels h) through j) depict the decrease of domain contrast with increasing distance from the surface.

For thin films, the stray field pattern emanating from the sample surface shows 'domain wall contrast' (with high stray field at the locations of the domain walls and low in the center of the domains) at small distances [Figs. 2.1 c) and d)], and 'domain contrast' (with low stray field at the locations of the domain walls and high in the center of the domains) at small distances [Fig. 2.1 e)]. For example, the red dotted ellipses in Figs. 2.1 c) and e) highlight typical domain wall contrast and domain contrast, respectively. For bulk samples, the stray field shows only domain contrast [Figs. 2.1 h)-j)].

18

2.1.1.3   MFM signal

In MFM experiments, we measure the change of the cantilever's first mode frequency arising from the tip's interaction with the stray field emanating from the sample surface.

For an infinitesimally small cantilever oscillation amplitude, the first mode frequency shift is given by:

$$\Delta f_1 = -\frac{f_1}{2k_1}\frac{\partial F_z(z)}{\partial z}, \tag{2.7}$$

where f_1 and $2k_1$ are the first mode resonance frequency and force constant (stiffness) of the cantilever, respectively, and $k_{ts}(z) = \frac{\partial F_z(z)}{\partial z}$ is the z-derivative of the sum of all forces acting on the tip.

If the latter can not be approximated as constant in the z-range covered by the oscillating tip (oscillation amplitude comparable to the decay length of the force), expression 2.7 does not hold, and the frequency shift has to be calculated as:

$$\Delta f_1 = -\frac{f_1}{2k_1}\langle k_{ts}\rangle, \tag{2.8}$$

where $\langle k_{ts}(z)\rangle$ is a weighted average of $k_{ts}(z)$.

Since we are measuring solely the first mode resonance frequency shift of the cantilever in this thesis work, the notation Δf_1 becomes Δf for simplicity.

As discussed in Section 2.1.1.1, magnetic force, van der Waals force, and capacitive force act on the cantilever at the same time. The first arises from magnetic structures of the sample, and the later two arise from the topography. Hence the frequency shifts, as the derivative of all the forces acting on the tip [Eq. 2.7], comprise three parts: Δf_{mag} accounting for the magnetic tip-sample interactions (arising from magnetic domains), Δf_{topo} for the topography-induced interactions,

and Δf_{bgnd} accounting for the signal arising from a magnetic 'roughness' (due to the thickness variations of a film with uniform magnetization) and the topo-magnetism (due to the topography of a film with uniform thickness and uniform magnetization).

2.1.2   Achieving high lateral resolution in MFM

Each spatial Fourier component of the magnetic fields decays exponentially with increasing distance from the sample surface with a decay constant that is inversely proportional to its spatial wavelength (see Eq. 2.6). The Fourier components with small spatial wavelengths providing the high spatial resolution signal can thus be obtained with greater amplitudes if the MFM data is acquired at the small tip-sample distances, provided the MFM has a sufficiently high sensitivity. Maintaining small tip-sample distances requires a feedback method to compensate drifts. We discuss this further below and in Chapter 3.

As for high measurement sensitivity, it can be obtained if the mechanical properties of the cantilever are appropriately tuned. For a deflection sensor with a sufficiently high signal-to-noise ratio, the sensitivity of the MFM measurements is limited by the thermal noise of the cantilever. In a cantilever-based MFM, the thermodynamic limit for the minimally measurable force derivative on the n-th cantilever oscillation mode is given by [23]:

$$\left.\frac{\partial}{\partial z}F_z\right|_{min} = \frac{1}{A_n}\sqrt{\frac{4k_{\text{B}}Tk_nB}{Q_n\omega_n}},\tag{2.9}$$

where A_n is the oscillation amplitude, Q_n the quality factor, ω_n the resonance frequency and k_n the equivalent stiffness of the n-th cantilever oscillation mode, with B the bandwidth, k_{B} the Boltzmann constant, and T the temperature.

Rugar et al. [24] have shown that long and thin cantilevers are advantageous for obtaining high sensitivity, because the ratio of k_n and ω_n is inversely proportional to the cantilever length, and the quality factor Q is high for long, thin and narrow cantilevers. In their work, cantilevers with a spring constant of $3\,\mu N/m$ which gives rise to a force sensitivity of $1.4{\times}10^{-18}\,N/\sqrt{Hz}$ at $2.6\,K$ have been presented. Such ultra-soft cantilevers can only be approached to the sample with their long axis normal to the sample surface. These cantilevers are not suitable for MFM because of their low resonance frequency (e.g. a few kHz).

For conventional MFM experiments performed in air, a double-passage operation mode is typically used. The magnetic interaction is measured with the tip lifted off the surface of the sample after the topography of the sample has been scanned in an intermittent contact mode. The latter requires cantilevers with a sufficient stiffness, typically a few N/m.

In my thesis, cantilevers with a force constant between $0.7\,N/m$ and a resonance frequency of about $50\,kHz$ were used. These cantilevers have a high quality factor (typically 50 000), provided that the reflective coating on the cantilever backside and the magnetic coating on the tip side are appropriately fabricated (see Section 2.4). In addition, we performed the experiments in ultra high vacuum (UHV) and at $10.5\,K$.

2.2   Quantitative MFM

Asserting the quantitative nature of the MFM measurements presupposes that the measurements can be compared quantitatively with models thereof. Achieving it, therefore, necessitates a physical description of the image formation process, such that we can connect magnetization-, stray field-, and frequency shift-patterns

among each other uniquely. In Section 2.1.1.1, we expressed the magnetic tip-sample force in Fourier space as the product of the stray field of the sample and the effective magnetization of the tip (Eq. 2.5).

More succinctly, the first mode frequency shift caused by magnetic interactions can be expressed as [25]:

$$\Delta \hat{f}_{\text{mag}}^{A_1>0}(\mathbf{k}, z) \;\; = \;\; TF(\mathbf{k}) \cdot \frac{d\hat{H}_{\text{n}}^{A_1}(\mathbf{k}, z)}{dn}\bigg|_{\text{eff}}, \tag{2.10}$$

where the transfer function $TF(\mathbf{k})$ describes the imaging properties of the MFM cantilever in Fourier space, and the effective stray field derivative along the n-axis (see Fig. 2.2) canted $12°$ (typically) with respect to the z-axis is defined as:

$$\frac{d\hat{H}_{\text{n}}^{A_1}(\mathbf{k}, z)}{dn}\bigg|_{\text{eff}} := \frac{2}{A_1} LCF(\mathbf{k}, \eta) I_1(\tilde{z}) \frac{1}{-k} \frac{\partial \hat{H}_{\text{z}}(\mathbf{k}, z)}{\partial z}, \tag{2.11}$$

where A_1 is the first mode cantilever oscillation amplitude, $LCF(\mathbf{k}, \eta) := -\frac{1}{k}\mathbf{n} \cdot \hat{\nabla}$ defines the lever-canting-Function, $I_1(\tilde{z})$ is the first order Bessel function, and $\frac{\partial \hat{H}_{\text{z}}(\mathbf{k}, z)}{\partial z}$ denotes the stray field derivative along the z-axis.
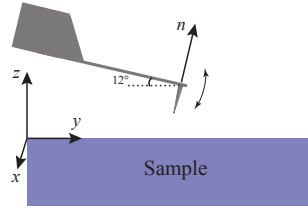

Figure 2.2: Schematic of the n-axis normal to long axis of the cantilever, with respect to the sample coordinates x-, y-, and z-axes.

Note that from Eqs. 2.5 and 2.6, the transfer function $TF(\mathbf{k})$ includes the effective tip magnetization which is generally unknown, and thus cannot be calculated directly but must be obtained through a tip calibration process.

2.2.1 Tip calibration

With Eq. 2.10, the transfer function $TF(\mathbf{k})$ can be obtained from the cantilever frequency shift and the effective stray field derivative that gave rise to it. In practice, it is possible to find the pattern of through thickness, homogeneous domains giving rise to the a domain MFM signal (Δf_{dom}). However, the magnetic background giving rise to Δf_{bgdn} cannot be obtained accurately. Therefore, we must instead remove Δf_{bgdn} from Δf – as well as any frequency shift pattern contribution not generated by the domains (e.g. Δf_{topo} from the topography). The stray field derivative can be calculated from Eqs. 2.6 and 2.11, given the domain pattern (estimated from the MFM image), the sample magnetization (determined from the magnetometry data), the tip-sample distance z (set and kept by the control method in Chapter 3), the cantilever oscillation amplitude A (maintained by phase-locked loop (PLL)) and the film thickness d (known from the sample fabrication). For accuracy of the tip calibration, the stray field calculation from the magnetization pattern we determined must accurately represent the sample. Hence we require a thin film sample with perpendicular magnetic anisotropy (PMA), sharp domain walls (containing magnetic structures of short spatial wavelength) and preferably domains size similar to the sample of interest (e.g. the TbFe thin films presented in Chapters 4 and 5).

The tip calibration process of determining the the transfer function $TF(\mathbf{k})$ is illustrated in Fig. 2.3. Note the measured MFM data consists of cantilever frequency shift induced by magnetic domains, a magnetic background, and the topography (see Section 2.2.1.2).

It is worth noting that noise in the determination of Δf can be reduced by averaging over different individual calculations of $TF(\mathbf{k})$ [26]. For this purpose,

Figure 2.3: Flow chart of the tip calibration process.

we utilize sub-images from a measurement on the calibration, that have the same size and pixel resolution as the MFM-scans on the sample of interest.

Here a $Si_{ox}/Pt_{10nm}/ [Co_{0.6nm}/Pt_{1nm}]_{\times 5} /Pt_{3nm}$ sample with an in-plane demagnetized (see Section 2.5.2) domain pattern was used for the tip calibration. The layer structure is illustrated in Fig. 2.4.

Figure 2.4: Illustration of the layer structure of the calibration sample, where the curved lines present the interaction between the tip and each of the 5 Co layers.

The sample magnetization of 1.04×10^6 A/m is determined from the vibrating sample magnetometry (VSM) data by attributing the measured total magnetic moment solely to the Co layers (the polarization of the Pt layers are not considered, see Fig. 2.4). The sample exhibits a strong PMA, and the domain wall width can be calculated from the known magnetic anisotropy and exchange stiffness of

the material. MFM scans were carried out on this calibration sample under the same conditions as the TbFe thin films as described in Section 4.3.2. An area of 3.75 μm×3.75 μm with 320×320 pixels was scanned. From this data 1400 256×256 pixels-images of 3 μm×3 μm size were extracted and used to obtain 1400 transfer functions $TF(\mathbf{k})$. From these an average transfer function $TF(\mathbf{k})$ was obtained.

2.2.1.1   Calculating the effective stray field derivative

As a first step toward obtaining the transfer function (TF) [see Eq. 2.10 and Fig. 2.3], the magnetization and the effective stray field derivative are calculated from the MFM data measured on the calibration sample in zero field [Fig. 2.5].
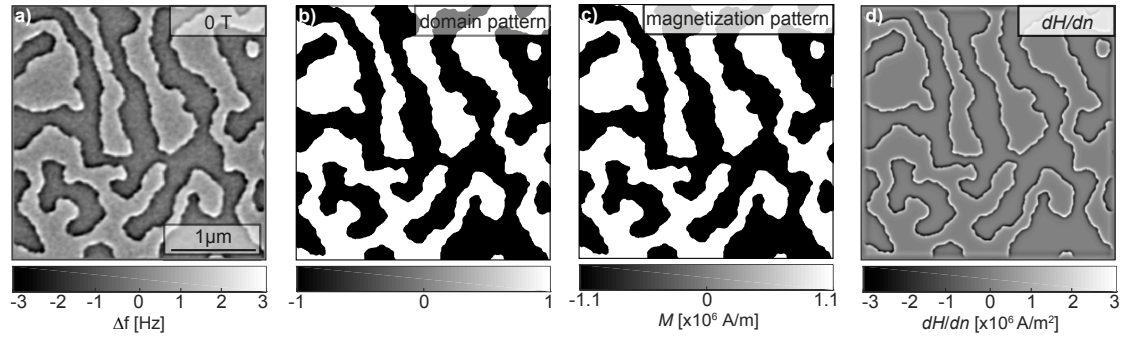

Figure 2.5: a) Frequency shift image obtained on the calibration sample with an in-plane demagnetized domain structure. b) Domain pattern estimated from the measured frequency shift data in panel a). c) Magnetization pattern. d) The effective stray field derivative $\frac{dH_n}{dn}$ calculated from panel b).

Figure 2.5 a) shows a 3 μm×3 μm sized frequency shift image of the calibration sample in an in-plane demagnetized domain state. The domain pattern [Fig. 2.5 b)] is estimated from the Fig. 2.5 a). For the domain wall location to be estimated accurately from thresholding the frequency shift pattern, the canting effect of oscillating cantilever (Fig. 2.2), which would otherwise lead to some vertical shift of the domain wall positions, is removed from the frequency shift image. Note that

the stray field (thus the frequency shift) is lower in the center of the domains [see Section 2.1.1.2], hence small variations of the stray field inside the domain could lead to artifacts in the domain pattern when fixed levels are used to discriminate whether a given spot belongs to up or down domains. To avoid this problem, a new frequency shift pattern is calculated from the measured one assuming an infinitely large thickness d and a smaller tip-sample distance z, which attenuate the *thickness loss* factor $(1 - e^{-kd})$ and the *distance loss* factor e^{-kz}, respectively. A threshold is then applied to this frequency shift image to determine the positions of the up and down domains. A domain wall width estimated from the magnetic anisotropy and the exchange stiffness of the sample is taken into account in the domain pattern [Fig. 2.5 b)]. The model magnetization pattern [Fig. 2.5 c)] is obtained as the product of the sample magnetization with the domain pattern [Fig. 2.5 b)].

Given the magnetization pattern [Fig. 2.5 c)], the film thickness d, and the tip-sample distance z, the effective stray field derivative $\frac{dH_n}{dn}$ can be calculated from Eqs. 2.6 and 2.11. The stray field is the sum of all stray fields arising from the Co layers, taking into account the distance loss factors for each of the 5 Co layers (Fig. 2.4).

2.2.1.2 Separating the magnetic frequency shift from the measured MFM data

As Fig. 2.3 indicates, the stray field derivative obtained in Section 2.2.1.1 does not correspond to the full Δf but to a part of it, Δf_{dom}, which needs to be separated from the measured Δf.

Figures 2.6 a) and b) show MFM data acquired on the calibration sample in

demagnetized domain state (in 0 T) and in remanence. Note that a background contrast ("roughness") is present in the MFM data for the sample in the remanent state [Fig. 2.6 b)]. This contrast can either arise from locally varying topography or the inhomogeneous distribution of the magnetic moment of the sample. To address this question, the difference and the sum of the MFM data shown in Figs. 2.6 a) and b) are displayed in Figs. 2.6 c) and d), respectively. In the difference image [Fig. 2.6 c)], the down domains appear rough while the up domains are smooth. In the sum image [Fig. 2.6 d)], it's the other way around. These observations prove, in addition to the topography-induced contrast, the presence of some contrast that switches sign with the relative tip-sample magnetization. This magnetic contrast Δf_{bgnd} ("magnetic roughness") is attributed to a magnetic background arising either from the inhomogeneous distribution of the magnetic moment areal density or from the variations of the magnetic layer thickness with a homogeneously distributed magnetic moment areal density.
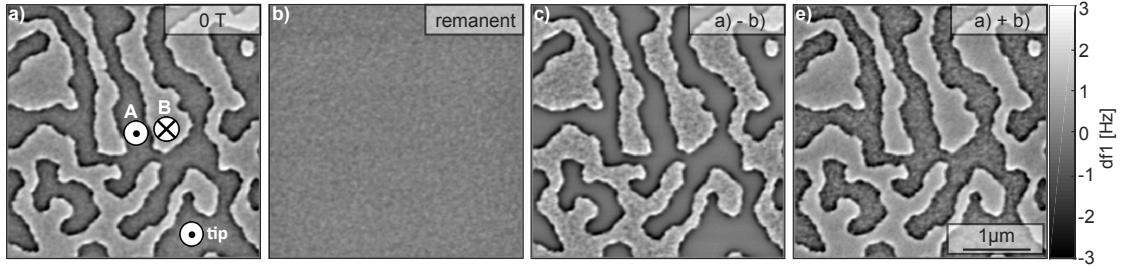

Figure 2.6: a) MFM-scan of the calibration sample in 0 T. b) MFM-scan of the calibration sample in saturated state. c) Difference of panels a) and b). d) Sum of panels a) and b). The frequency shift images are displayed with the same color-scale of -3 to 3 Hz given on the right of the figure.

Therefore, apart from the topography-induced frequency shift Δf_{topo}, the magnetic frequency shift Δf_{mag} in Fig. 2.6 a) consists of Δf_{dom} from the magnetic domains and Δf_{bgnd} from a magnetic background.

27

Figure [2.7](#) illustrates the frequency shift arising from the magnetic domains Δf_{dom}, the topography Δf_{topo}, and the magnetic background Δf_{bgnd}. For a sample in (as-grown or demagnetized) multi-domain state with the tip magnetization up, the up (attractive) and down (repulsive) magnetic domains contribute negative and positive frequency shifts [panel a)], respectively. The topography-induced frequency shift [panel b)] is in general negative due to the attractive nature of the van der Waals and capacitive interactions. The magnetic background leads to a small variation of Δf_{bgnd} around $0\,\mathrm{Hz}$ [panel c)].
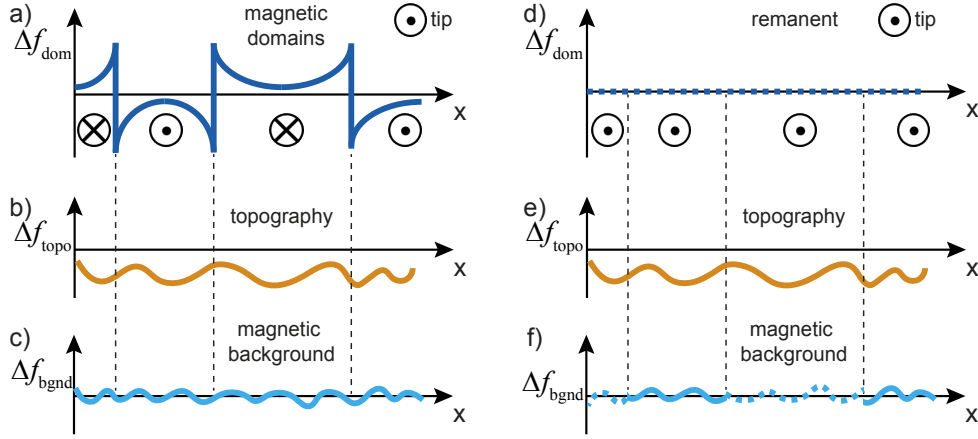
Figure 2.7: Cartoons illustrating the frequency shift arising from a) d) the magnetic domains Δf_{dom}, b) e) the topography Δf_{topo}, and c) f) the magnetic background Δf_{bgnd}. The sample is in as-grown or demagnetized multi-domain state in the left column, and in saturated or remanent (one-domain) state in the right column where the frequency shift is illustrated in dotted lines if altered and in solid lines if unaltered.

For a sample in the saturated (or single-domain remanent) state [right column of Fig. [2.7](#)], the magnetization is up over the entire sample, hence $\Delta f_{\mathrm{dom}} = 0$ [panel a)]. The topography-induced frequency shift [panel e)] is the same as that of panel b). The sign of the magnetic background-induced frequency shift Δf_{bgnd} is flipped within the previously existent repulsive domains [dashed lines in panel f)] while it remains the same as that of panel c) within the other domains [solid lines

in panel f)].

These three main contributions to the measured frequency shift, i.e. topography, magnetic domains, and magnetic background, are summarized in Table 2.1, for different sample and tip states. Positions "A" and "B" are marked in Fig. 2.6 a). As alluded to previously, the topography-induced frequency shift is in general negative, and it stays the same in cases 1 through 6. The magnetic interaction is attractive if the magnetizations of the tip and the sample are parallel and repulsive if anti-parallel.

Case	Sample state	Tip state	Sample region	Magneti-zation	Contributions to Δf		
					Δf_{topo}	Δf_{dom}	Δf_{bgnd}
1	multi-domain state	up	A	up	+1	+1	+1
2			B	down	+1	+1	+1
3		down	A	up	+1	−1	−1
4			B	down	+1	−1	−1
5	one-domain state	up	A	up	+1	0	+1
6			B	up	+1		−1

Table 2.1: Contributions to measured frequency shift for different tip and sample conditions. The regions A and B are marked in Fig. 2.6 a), representing the areas at the location of the up and down domains, respectively. The Δf_{topo} , Δf_{dom} , and Δf_{bgnd} contribute to the measured Δf multiplied with the sign indicated in the table for each case (+1, -1 or 0). For example, the measured total frequency shift is $\Delta f = \Delta f_{\text{dom}} + \Delta f_{\text{topo}} + \Delta f_{\text{bgnd}}$ for cases 1 and 2.

For a sample in a multi-domain state (as-grown or demagnetized state, cases 1-4), the frequency shifts arising from the domains Δf_{dom} and from the magnetic background Δf_{bgnd} change their signs if the tip magnetization is flipped [compare states 3 to 1, and 4 to 2].

The sample is in a one-domain state (saturated or remanent state, cases 5-6) after applying an up magnetic field H above its coercive field. The domain-induced frequency shift Δf_{dom} vanishes. The frequency shift arising from the magnetic

background changes its sign in regions where down domains existed previously (case 6), and stays the same in regions where previously the domain was magnetized up (case 5).

As a result, the topography-induced frequency shift can be obtained from the half-sum of the MFM data measured in zero field with up and down tip magnetizations (see Table 2.1, sum of cases 1 and 3 for up domains, and cases 2 and 4 for down domains). Further, the contribution from the magnetic background can be separated from the MFM data measured on the sample in the remanent state (cases 5 and 6 in Table 2.1) by subtracting the topography from it.

Figure 2.8 depicts the frequency shift Δf measured on the calibration sample in zero field with up [Fig. 2.8 a)] and down [Fig. 2.8 b)] tip magnetization and in remanent state after saturating the sample with an applied field of 500 mT in the up direction [Fig. 2.8 d)]. The non-magnetic contribution to the measured frequency shift arising from the sample topography induced spatial variation of the van der Waals force can be calcualted from the half-sum of Figs. 2.8 a) and b). Apart from the a granular variation of the frequency shift, a pattern of faint lines reminiscent of the domain walls is visible in Fig. 2.8 c). We attribute these e.g. to a small change of the domain wall magnetization distribution in the field of the tip or conversely to a (reversible) modification of the tip magnetization structure in enhanced field at the location of the domain wall. Before the MFM data acquired with different tip magnetizations or in different applied fields can be compared or used for pixel-wise linear combinations, images must be aligned and mutual image distortions must be minimized. Here we use a simple phase correlation method [27] for the alignment of different images.

For the sample in remanent state [Fig. 2.8 d)], the magnetic background [Fig. 2.8 e)]
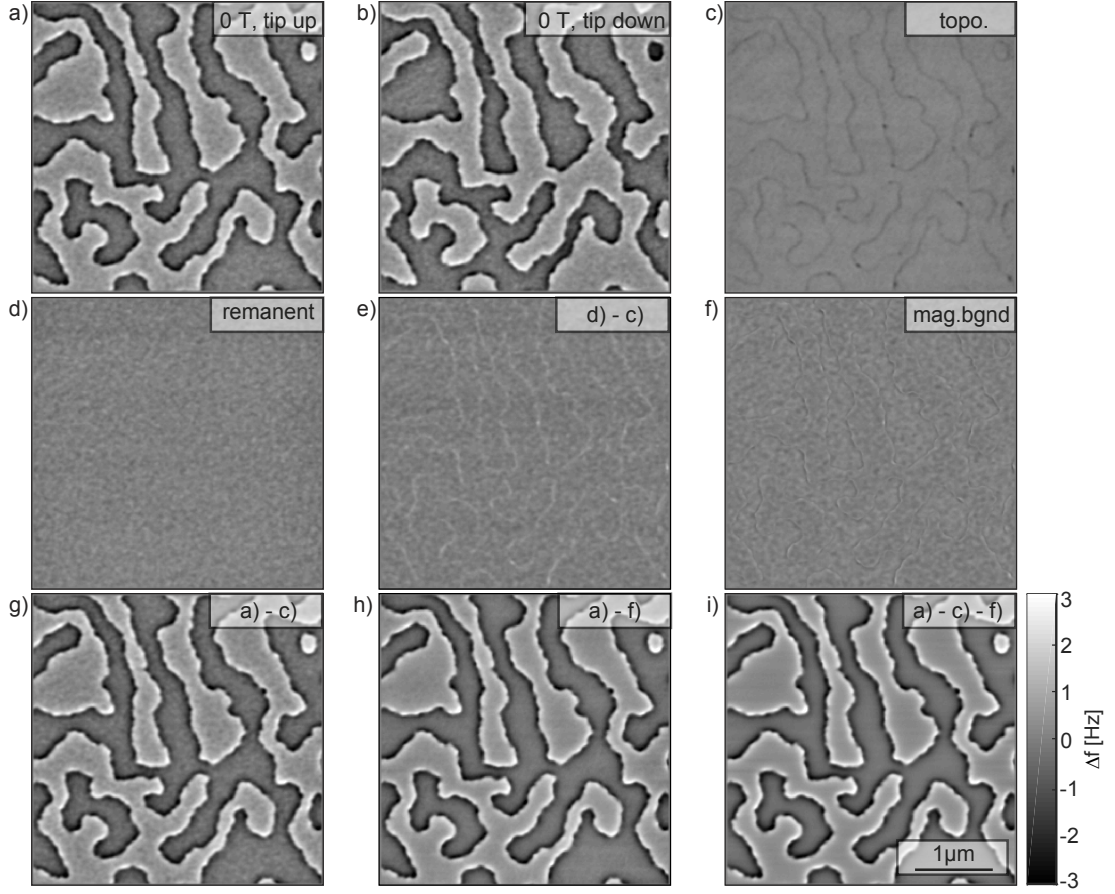
Figure 2.8: a) and b) MFM images acquired in 0 T with up and down tip magnetizations, respectively. c) Half-sum of data shown in a) and b), representing the topographic contribution in Δf. d) MFM-scan of the calibration sample in saturated state. e) Difference of panels d) and c). f) Panel e) multiplied by the inverted domain pattern. g) h) Difference of panels a) and c). h) Difference of panels a) and f). i) Subtracting of panels a) and f) from panel a). The frequency shift images are displayed with the same color-scale of -3 to 3 Hz given on the bottom right of the figure.

is obtained by subtracting the topography [panel c)] from it. Figure 2.8 e) shows small variations of frequency shift in both domains, which is illustrated as the solid blue line in Fig. 2.6 c)]. To obtain the magnetic background for the sample in the multi-domain state [Fig. 2.8 a)], Fig. 2.8 e) is multiplied pixels-wise by the inverted binary domain pattern [Fig. 2.5 b)]. The resulting image, i.e. the frequency shift arising from the magnetic background, is displayed in Fig. 2.8 f).

Note that the faint lines of Fig. 2.8 e) are masked out before the multiplication. The topography [Fig. 2.8 c)] and magnetic background [Fig. 2.8 f)] are subtracted from the measured frequency shift image [Fig. 2.8 a)], resulting in Figs. 2.8 g) and h), respectively. They appear smoother than Fig. 2.8 a), but still contain some granularity within the domains. The frequency shift arising solely from the magnetic domains, i.e. excluding the contribution from topography and magnetic background, is depicted in Fig. 2.8 h). This is the MFM data to be used in Eq. 2.10 for the tip calibration, since the corresponding stray field derivative can be calculated for it (Section 2.2.1.1).

2.2.1.3 Obtaining the transfer function $TF(\mathbf{k})$

The TF can be obtained from the division of the frequency shift by the effective stray field derivative [Eq. 2.10]. However, this division is an ill-posed problem, because the denominator (i.e. the effective stray field derivative) can be very small especially for short spatial wavelengths [see Section 2.1.1.2] and in the presence of noise. Therefore, the Tikhonov regularization method [28, 29, 30] is used to determine the transfer function:

$$TF(\mathbf{k}) \approx \Delta \hat{f}_{\text{mag}}^{\text{subtr}}(\mathbf{k}) \cdot \frac{\left. \frac{d\hat{H}_{\text{n}}^{\text{A}_1}(\mathbf{k},z)}{dn} \right|_{\text{eff}}}{\delta + \left| \left. \frac{d\hat{H}_{\text{n}}^{\text{A}_1}(\mathbf{k},z)}{dn} \right|_{\text{eff}} \right|^2}, \tag{2.12}$$

where the Tikhonov parameter δ defines a penalty for diverging solutions, effectively limiting the amplitudes of the TF when the stray field derivatives are smallest, normally at small spatial wavelengths.

Figure 2.9 depicts the decay of the transfer function amplitude with decreasing spatial wavelength λ and its dependence on the Tikhonov parameter δ. Higher

32

values of δ give rise to a smoother transfer function (green and purple lines in Fig. 2.9), but the TF is accordingly reduced for small spatial wavelengths. Smaller values of δ lead to transfer functions of higher amplitudes, especially at small wavelengths, but also allow more noise at those wavelengths (kinks in the blue and red lines in Fig. 2.9). Recall that MFM images are $3\,\mu\mathrm{m}\times3\,\mu\mathrm{m}$ sized with 256×256 pixels, so the minimally measurable wavelength $\lambda_{\min}$ can be estimated as twice the pixel resolution, i.e. $23.4\,\mathrm{nm}$. In practice, $\lambda_{\min}$ is usually larger due to the noise in the measured data. Based on Fig. 2.9, we deem the transfer function noise to be tolerable for wavelengths larger than $33\,\mathrm{nm}$, and so $\lambda_{\min}$ is set to be $33\,\mathrm{nm}$. The best choice for the Tikhonov parameter is the highest value that does not have a significant influence on the transfer function in the range of signal wavelength $\lambda > \lambda_{\min}$ [25]. In practice, this means that the numerical noise is suppressed sufficiently for the MFM contrast to be simulated with the correct amplitude and no artifact for $\lambda > \lambda_{\min}$. In our case, $\delta = 10^{16}$ gives an accurate transfer function for wavelengths larger than $\lambda_{\min} = 33\,\mathrm{nm}$.
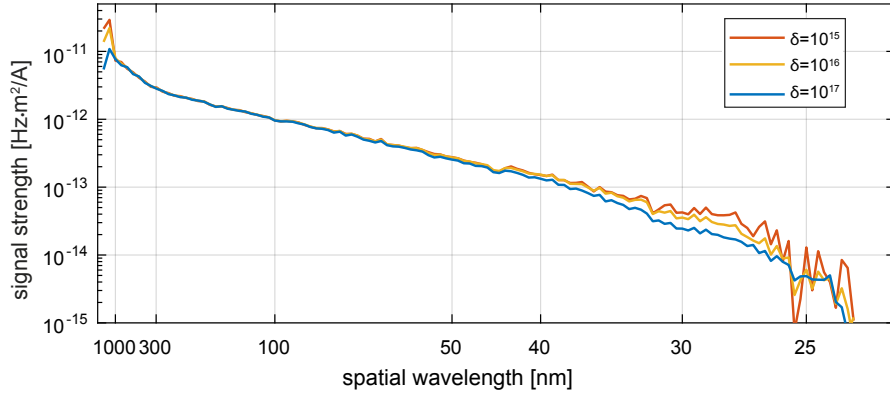
Figure 2.9: The dependence of the transfer function on spatial wavelength for different Tikhonov paremeters, where $\delta = 10^{16}$ gives the optimal TF.

The transfer function in real space for a Tikhonov parameter $\delta = 10^{16}$ is depicted

in Figs. 2.10. We will use this transfer function to accurately model magnetization features corresponding to wavelengths larger than $\lambda_{\min} = 33\,nm$, i.e. sizes down to 16.5 nm.
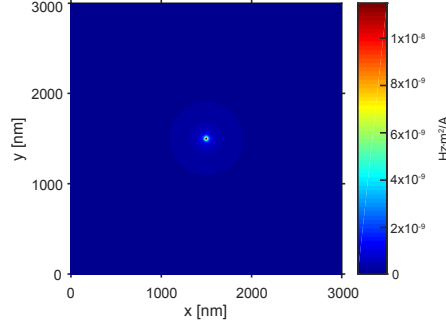
Figure 2.10: The transfer function in real space.

2.2.2 Modeling of the MFM data

Once the transfer function is determined (the tip is calibrated), it can be used to calculate a frequency shift pattern from the stray field pattern arising from a model magnetization pattern. This allows to test the matching of different model magnetization structures quantitatively. Conversely the stray field at different distances z from the sample surface can be deconvolved from measured frequency shift data, providing quantitative values of the field, rather than the frequency shift.

2.2.2.1 Simulation of the MFM frequency shift image

To provide an example of the comparison between experiment [Fig. 2.11 a)] and simulation [Fig. 2.11 b)], Fig. 2.11 c) shows the difference of the simulated and the measured magnetic frequency shift. The simulated frequency shift was calculated [see Eq. 2.10] from the effective stray field derivative $\frac{dH_n}{dn}$ [Fig. 2.5 d)] and the

transfer function for a Tikhonov parameter $\delta = 10^{16}$ [Fig. 2.9].
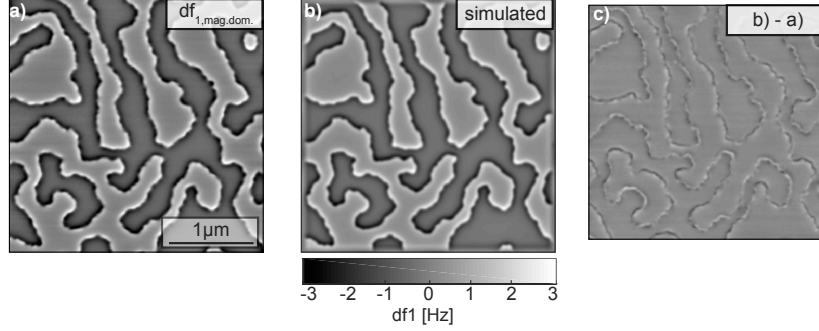
Figure 2.11: a) Domain-induced frequency shift image Δf_{dom} [already shown in Fig. 2.8 i)]. b) Simulated frequency shift image. c) Difference image of b) - a).

In the difference image [Fig. 2.11 c), where 10 pixels on each of the 4 edges are cut off], the frequency shift inside both the up and down domains are close to zero, while the main contrast arises from the domain walls due to the mismatch between the estimated and the actual domain wall width. This shows that the domain-induced frequency shift [Fig. 2.11 a)] can be simulated with the correct magnitude.

2.2.2.2 Recovery of the sample magnetization

The magnetization pattern $M_{\mathrm{z}}^{\mathrm{avg}}$ can be deconvolved from the frequency shift with:

$$\hat{M}_{\mathrm{z}}^{\mathrm{avg}}(\mathbf{k}) = \frac{\Delta \hat{f}_{\mathrm{meas}}(\mathbf{k})}{TF(\mathbf{k}) \cdot \alpha(\mathbf{k}) \cdot (1 - e^{-kd})} \left(\frac{1}{A_1} LCF(\mathbf{k}, \eta) I_1(\tilde{z}) \right)^{-1}, \qquad (2.13)$$

where d is the magnetic layer thickness, A_1 is the first mode oscillation amplitude of the cantilever, $I_1(\tilde{z})$ is the Bessel function, $LCF(\mathbf{k}, \eta)$ defines the canted tip oscillation path, and $\alpha(\mathbf{k})$ is a wavelength dependent distance loss factor taking into account the distance from the tip to the magnetic layer(s).

There are generally two major difficulties for the recovery of the sample mag-

netization. Firstly, because of the *distance loss* factor e^{-kz} and the *thickness loss* factor $(1 - e^{-kd})$ (see Section 2.1.1.2), the stray field is suppressed for large spatial wavelengths, and thus the frequency shift in the middle of (large) domains may be pushed below the measurement noise. Practically, the k-amplitudes of the noise will be amplified by the inverse distance loss at exponential rates, particularly for the small wavelengths. Secondly, the transfer function $TF(\mathbf{k})$ is more noisy at shorter wavelengths. This noise also enters the division (Eq. 2.13) which would give rise to artifacts in the deconvolved magnetization. To limit these problems, we implement a cutoff frequency k_{limit} defined as $1/k_{\mathrm{limit}} = \lambda_{\mathrm{min}}$, where $\lambda_{\mathrm{min}} = 33 \, \mathrm{nm}$.

Recall that the transfer function is calculated with a multilayer calibration sample. Because we ascribe the stray field to one same magnetization pattern on each of the discrete Co layers in the multilayer, the transfer function must account for as many different distance loss factors. These space propagators can be lumped together in a single factor which is implicit in TF. When using the TF to simulate single layers, that propagator factor needs to be removed. Consequently, the transfer function obtained in Section 2.2.1.3 cannot be used directly to recover the magnetization of our multilayer calibration sample, because its 5 Co layers are located at different distances from the surface [see Fig. 2.4] but these distance losses are not contained in Eq. 2.13. To address this problem, an effective transfer function, equivalent to the propagation of the tip stray field to the positions of each of the 5 Co layers, is calculated. This propagated transfer function is then used to recover the magnetization of the multilayer.

Figure 2.12 shows the propagated transfer function for $\delta{=}15$, and the TF with cutoff frequency k_{limit}.

Figure 2.13 a) and b) depict the model magnetization pattern for the calibration
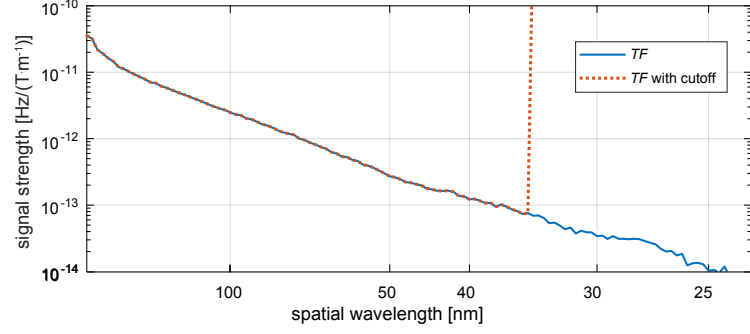
Figure 2.12: The dependence of the propagated transfer function on spatial wavelength for $\delta = 10^{16}$ (blue solid line). The red dashed line is the TF with cutoff frequency k_{limit}, where $1/k_{\text{limit}} = 33\,nm$.

sample in remanent state [previously shown in Fig. 2.5 c)] and the deconvolved magnetization pattern. For comparison, the difference of Figs. 2.13 a) and b) is displayed in Fig. 2.13 c). It can be seen that the magnitude of the deconvolved magnetization is slightly higher than that from the model magnetization. This can be attributed to cutting off the high frequency components of the transfer function (red dashed line in Fig. 2.12).
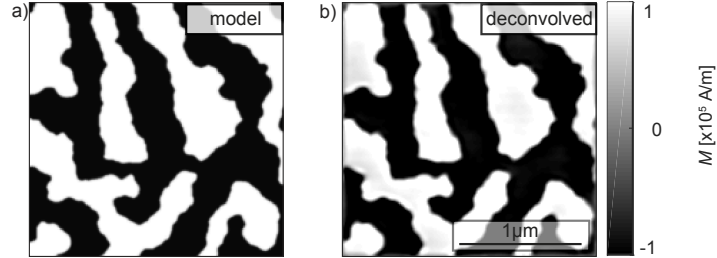
Figure 2.13: Magnetization pattern M for the calibration sample, displayed with the scale of -110000 to 110000 A/m. a) Model magnetization pattern. b) Deconvolved M in zero field.

The tip whose calibration has been carried out to furnish TF, is used for the MFM measurements on the TbFe-based samples, and therefore the transfer function TF is employed for the modeling of the MFM data in Chapters 4 and 5.

2.3 Low-temperature MFM system (LT-MFM) instrumentation

2.3.1 System description

A home-built ultra-high vacuum (UHV) low-temperature MFM system (LT-MFM), designed and built by Prof. Hug in 1998 [31], is used for the MFM experiments performed in this thesis. The LT-MFM system was transferred from a lab at the University of Basel to Empa, updated and re-installed at the beginning of my thesis work. Furthermore, a new control system was implemented and a control software *Scanit* was designed in collaboration with the Paul Scherrer Institute (PSI) and implemented by Semafor Informatik und Energie AG[1] .

A picture of the LT-MFM system is displayed in Fig. 2.14. The scanning force microscope is located in an UHV chamber with base pressure of about 1×10^{-10} mbar. An external field perpendicular to sample surface, up to 7 T, can be applied by means of a superconducting solenoid located inside the cryostat.

The LT-MFM system consists of two UHV chambers and a load-lock system. The vacuum chamber on the right, the so-called preparation chamber, allows the in-situ preparation of samples and cantilevers. For the work presented in this theis, the preparation chamber was only used for the transport of the sample and cantilever holders, because all cantilevers and samples were prepared in an separate UHV sputter deposition system (see Sections 2.4 and 2.5). A manipulator transports the sample and cantilever holders between the load-lock chamber and the scanning force microscope chamber (main chamber). Typically, many samples and cantilevers are kept in the main chamber on storage carousels. A VG me-

---

[1]Sperrstrasse 104 B, CH - 4057 Basel Tel. +4161 690 98 88, Fax. +4161 690 98 80, Email info@semafor.ch
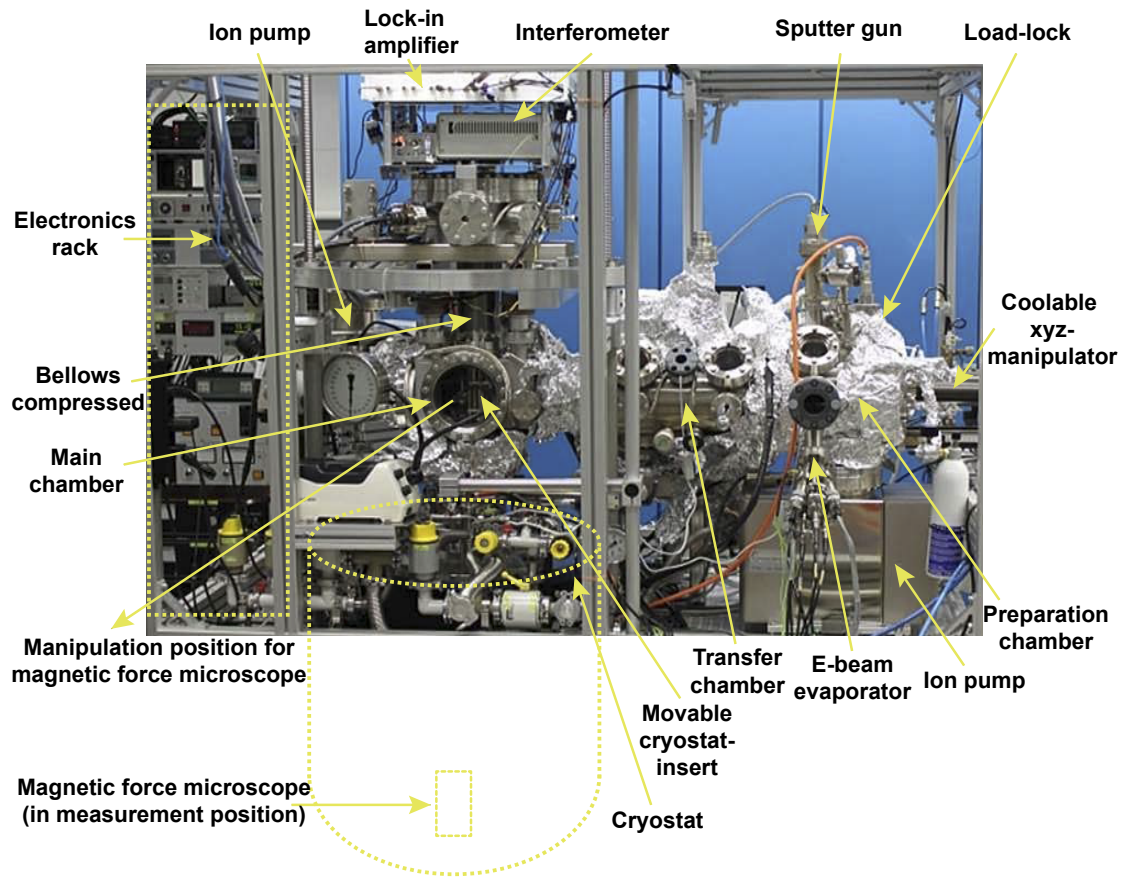
Figure 2.14: Image of the LT-MFM system in which the MFM scans and some tip/sample preparations were performed, with some of the main components labeled.

chanical hand manipulator was used for the transfer of a selected sample and/or cantilever holder(s) to the microscope. While the mounting of the sample holder is a comparatively easy task, that of the cantilever is challenging. The cantilever holder has to be pushed until it snaps into a mechanically defined position such that the cantilever becomes located above the cleaved end of an optical mono-mode fiber. While the relative position of the cantilever holder and fiber is defined by a kinematic mount, the position of the cantilever on the cantilever holder must be pre-adjusted outside the instrument on a dummy-stage which replicates the relative position of the fiber and cantilever holder of the instrument. The details

of cantilever mounting are given in the following pages.

Once both the sample and tip are placed inside the microscope, the tip is approached under visual control at a suitable position above the sample (about 50 um away). This is done by the xyz-piezo positioners of the microscope. The final approach is performed remotely without optical surveillance, once the microscope has been lowered into the cryostat using the bellow system (Fig. 2.14). At that point the microscope is located in the center of a superconducting solenoid that allows the application of magnetic fields of up to 7 T. After lowering the microscope, it takes typically several hours until the target temperature (in this thesis 10.5 K) is obtained.

2.3.2 Cantilever and sample mounting

The cantilever deflection in a SFM is often measured by a position sensitive photodetector (PSD) or a fiber-based interferometer system. The schematics of both systems are depicted in Fig. 2.15. In our LT-MFM system, an interferometer optic deflection sensor is used because it obtains a high deflection sensitivity, and only the end of a cleaved fiber but no PSD or electronic components are located inside the microscope at low temperature. However, the cantilever-fiber interferometer system requires that the cantilever is positioned very close to the fiber and aligned to its core with high precision.

A good deflection sensitivity is obtained if the cantilever is parallel to the cleaved fiber end surface at a distance not exceeding 20 μm [Fig. 2.16 c)]. Because a fiber-to-cantilever piezo-motor positioning system could not be implemented in 1993 when the instrument was designed [32], the positioning of the cantilever to the fiber is performed outside the vacuum system on a dummy stage that replicates
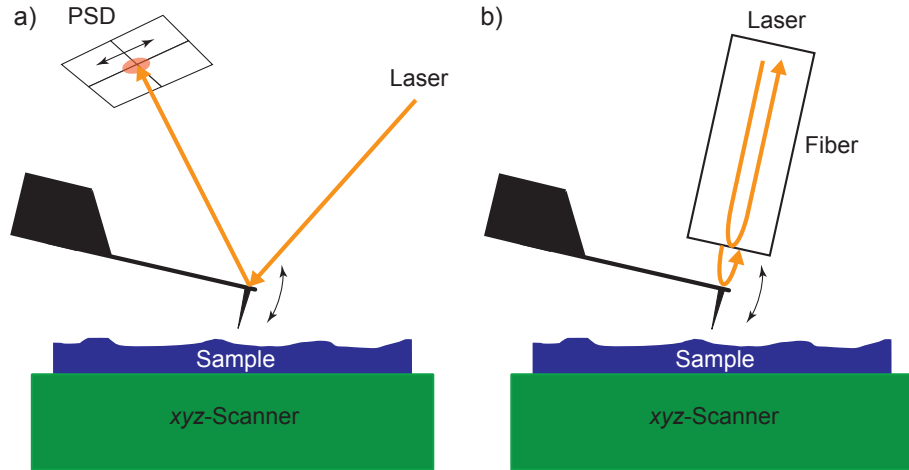
Figure 2.15: Schematics of cantilever with sharp tip in close proximity to sample surface. a) Cantilever deflection measured by PSD. b) Cantilever deflection measured by fiber-based interferometer system.

the setup of the kinematic cantilever holder mount of the SFM. The alignment procedure is:

1. The cantilever is clamped onto the cantilever holder by the spring that presses it against the body of the holder;

2. The cantilever holder is then inserted into the receiver on top of the dummy stage highlighted by the yellow circle in [Fig. 2.16 a)];

3. The fine adjustment of cantilever position with respect to the fiber is achieved by moving the cantilever chip carefully with tweezers for lateral alignment and by tuning the 3 mounting crews in the cantilever holder for vertical alignment. With some practice I was able to manually align the cantilever to the fiber core with a precision of about 5-10 µm;

4. The properly adjusted cantilever is glued with silver epoxy, cured on a heating plate for one hour at 100 °C, and then the clamping spring on the holder
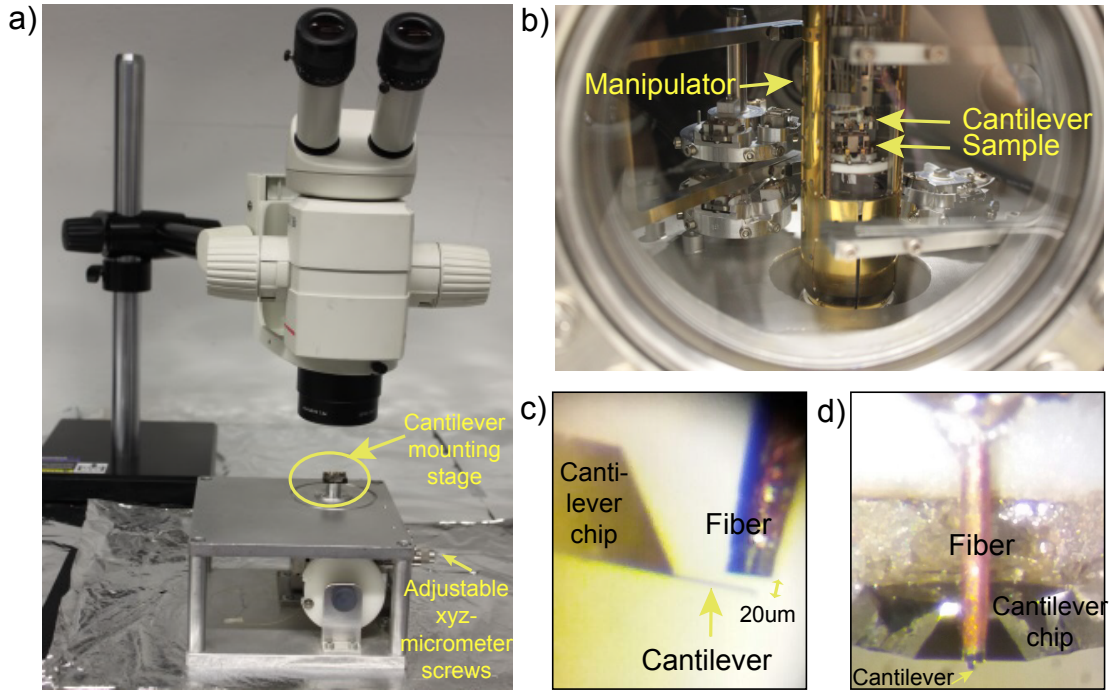
Figure 2.16: a) The dummy stage used to align the cantilever to the fiber. b) Magnetic force microscope raised from the bottom of the cryostat to the SFM chamber. The microscope which is spring-suspended can be firmly fixed between two clamps for a successive cantilever or sample holder exchange. These holders are inserted with a VG mechanical hand manipulator. c) Side view of a cantilever aligned to the end of the optical fiber. d) Front view of the aligned cantilever.

is removed.

Following this procedure, the cantilever holder is introduced into the UHV system [see Fig. 2.16 b)].

Samples are typically glued onto CuBe 14 mm×10 mm sized plates that are mounted onto the sample holder by 4 screws. UHV compatible silver epoxy is usually used to fix the sample to the CuBe plate, by applying moderate amount of silver epoxy on the sides of the sample. The electrical contact, which is needed for capacitive tip-sample distance control (see Chapter 3), is realized by bridging the sample surface and the mounting plate with silver epoxy. The sample holder

is introduced into the UHV system and mounted onto the microscope in a similar way to the cantilever holder.

2.3.3   Control system hard- and software

A block diagram of the electronic control system used for all experiments in this thesis is depicted in Fig. 2.17. The system consists of a PC running the *Scanit* and *ZI* software, a real-time National Instruments (*NI*) rack, a high-voltage amplifier (HVA), a piezo motor controller (PMC), and a Zurich Instrument (*ZI*) lock-in amplifier system. The background color is blue and red for hard- and software part of the control system, respectively. The red and blue lines are the cables for digital and analog signals, and the black lines illustrate the logic connections of processing unit and data flow.

The *NI* rack contains two field-programmable gate array (FPGA) cards with 8 digital-to-analog converters (DACs) and 8 analog-to-digital converters (ADCs) each [middle upper blue block in Fig. 2.17], a NanoScan piezo motor controller (PMC) card that was later replaced by an external PMC controller built by Michael Steinacher at the University of Basel electronic workshop[2], and a *NI* real-time PC. The real-time PC runs the real-time part of the *Scanit* software [red block in Fig. 2.17]. Further components are the high-voltage amplifier (HVA) [right blue block in Fig. 2.17] used to drive the *xyz*- and *w*-piezos of the SFM, and an interferometer system used to measure the cantilever deflection [bottom in Fig. 2.17].

The PC [left blue block in Fig. 2.17] is connected to the *NI* real-time PC and the HVA via a local Ethernet, and to the *ZI* system [middle lower blue block in

---

[2]Departement of Physics, University of Basel, Klingelbergstrasse 82, 4056 Basel, Switzerland
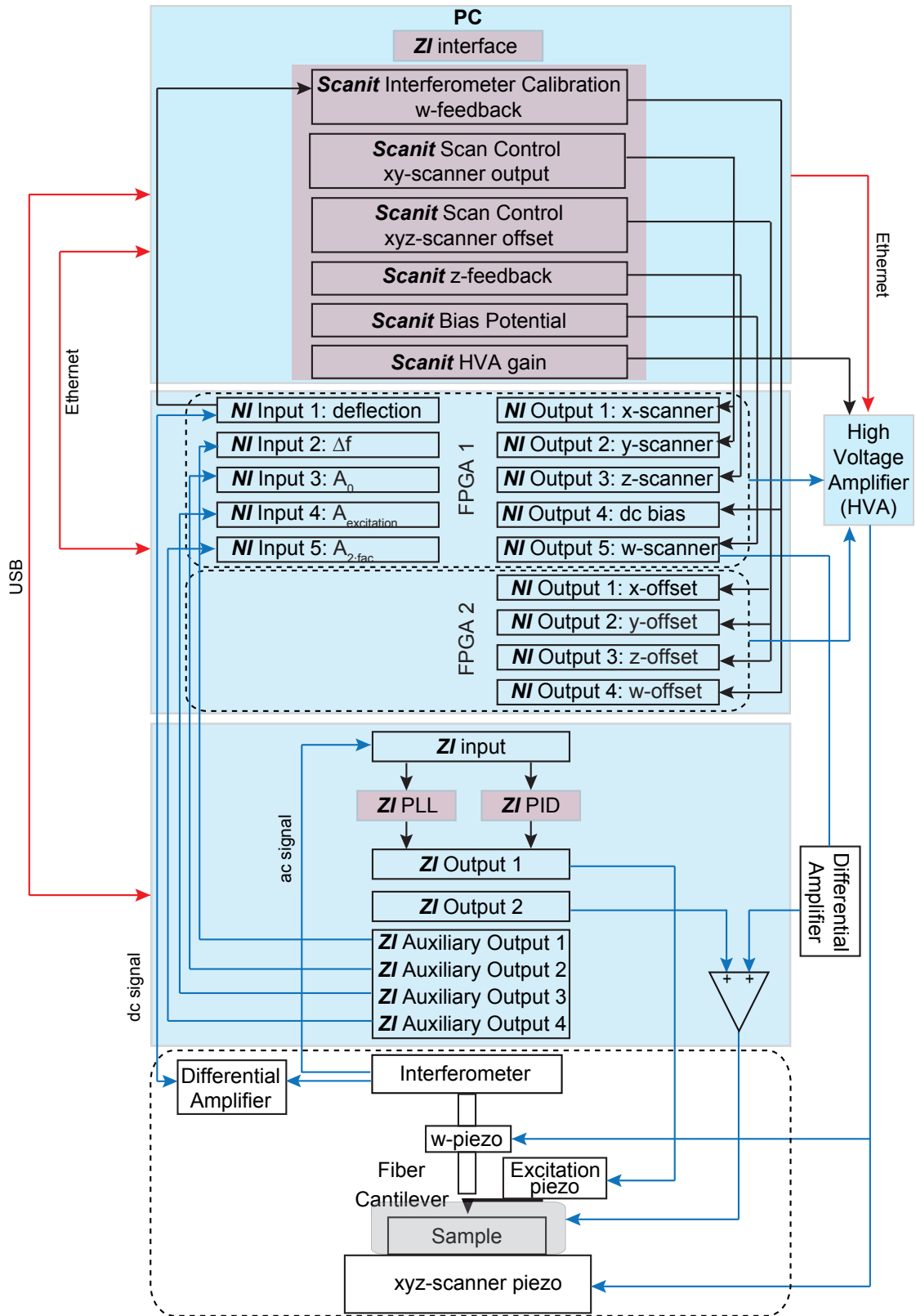
Figure 2.17: Block diagram of the electronic control system used for the MFM experiments in this thesis.

Fig. 2.17] via USB. The Ethernet and USB connections transmit control signals and measurement data. The DACs are used to send analog xyz- and w-scan and offset signals to the HVA, and apply a dc-sample-bias added to the ac-bias modulation provided by the *ZI* system. The adding is implemented with the differential output 2 of the *ZI*. The *ZI* output 1 is used to drive the excitation piezo of the cantilever. A PLL and a PI feedback of the *ZI* are used to track the cantilever's resonance frequency and to keep its oscillation amplitude constant. Changes of the first mode quality factor are thus compensated with an appropriate adjustment of the driving voltage from *ZI* output 1. For the tip-sample distance control, an oscillating tip-sample bias from *ZI* output 2 modulates the first flexural resonance while a dc-bias which zeros the tip-sample CPD is also added to *ZI* output 2. The schematics, working principle, and advantages of this operation mode suitable for high-field MFM operation under vacuum conditions is discussed in detail in Fig. 3.2 in Chapter 3.

The 6 lock-in amplifiers incorporated in *ZI* enable the simultaneous reading of digital signals of 6 different frequencies [Fig. 2.18], allowing the implementation of multi-modal measurement techniques. One such technique is the "Frequency-Modulated Capacitive Tip-Sample Distance Control" described in Chapter 3.

The *ZI* control software provides functionalities such as amplitude feedback to keep the cantilever's first mode oscillation amplitude A_0 constant [panel b)], frequency "Sweeper" for cantilever resonance frequency sweeping [panel c)], and "Auxiliary Outputs" which are connected to *NI* for real-time signal processing [panel d)].

The PC, the *NI* real-time PC, and the gain/offset control of the NanoScan HVA are controlled by the *Scanit* software. Since *Scanit* was developed during my thesis
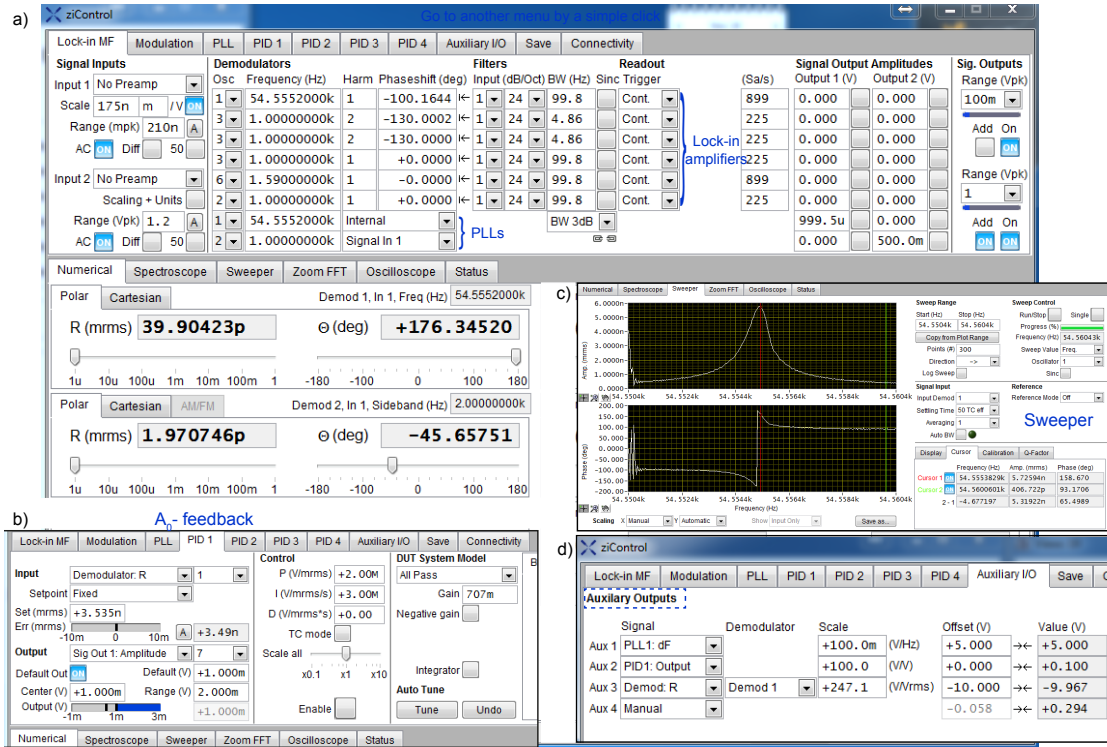
Figure 2.18: Image for Zurich Instrument Control window.

work, a major task was the implementation and debugging of the software and the control system. For this reason the main software features shall be reviewed briefly here.

The main panel of the control software *Scanit* is displayed in Fig. 2.19. The output channels of *NI* can be read from the "General Control". The tip-sample CPD can be determined and compensated by the "Bias Sweep" window (see bottom right panel). Kelvin potential force microscopy (KPFM) can be implemented via *ZI*, which adds both an ac-bias component to measure the local contact potential and a dc-potential to compensate it. The Kelvin-feedback is thus running on the *ZI*. For "z-feedback" which is performed on the real-time PC inside the *NI* rack, different analog input signals (e.g. Δf, $A_{2f_{\mathrm{ac}}}$) can be selected by the *Scanit*

46
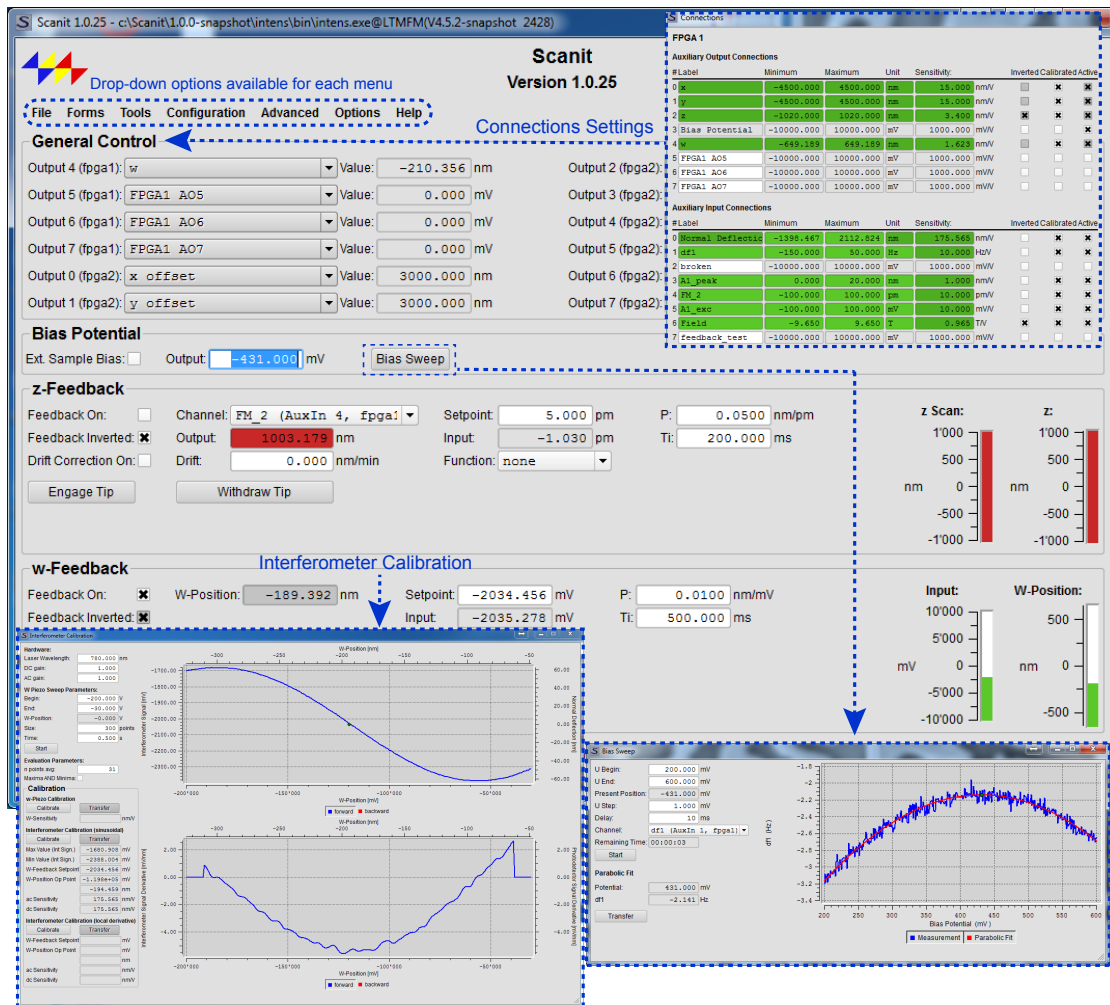
Figure 2.19: Image for the main window of *Scanit*.

software. For each input channel, a feedback parameter-set (consisting of the setpoint, the proportional gain P, and the integral gain I) can be defined and remains stored even if the input channel of the feedback is changed. The "*w*-Feedback" (also running on the real-time PC) is used to keep the fiber position exactly at the mid-position between constructive and destructive interference, i.e. at the point of maximum interferometer sensitivity. The optimal *w*-position and the interferometer sensitivity (in nm/V) are determined by a calibration procedure

via the "Interferometer Calibration" accessible from the drop-down menu of "Tools" (bottom left panel).
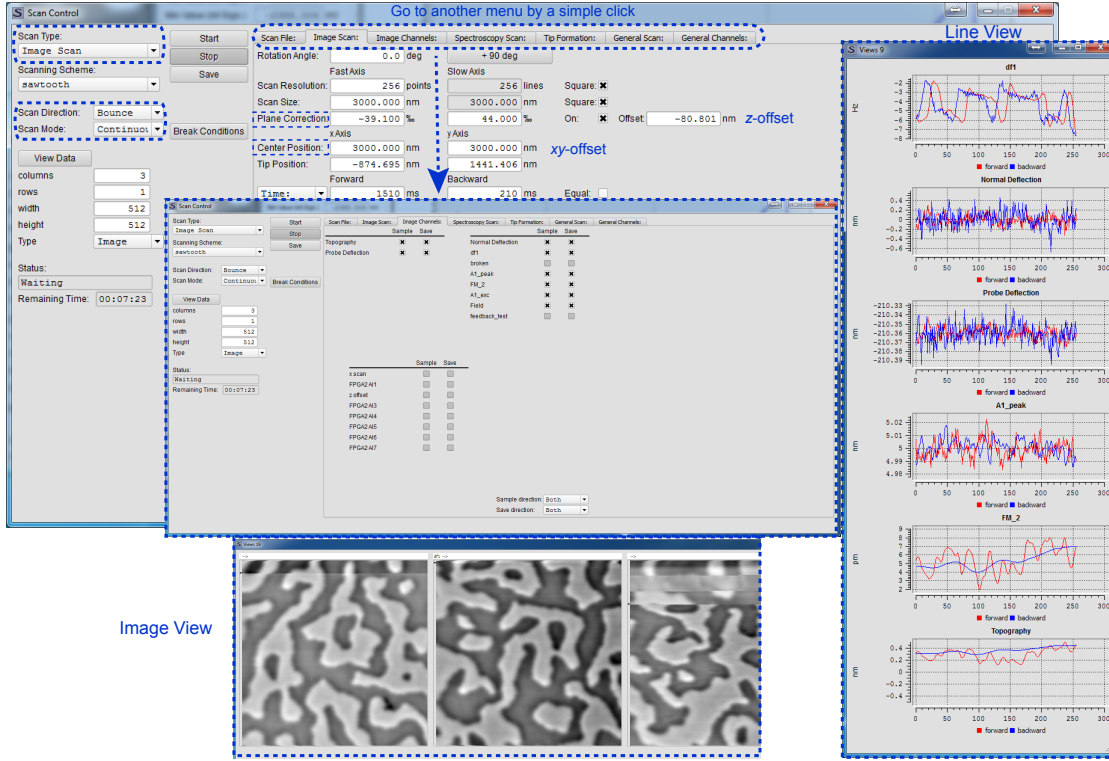
Figure 2.20: Image for the Scan Control window of *Scanit*.

The "Scan Control" allows different "Scan Type"s and the entry of scan parameters, as shown in Fig. 2.20. Both "Image View" and "Line view" are available. The displayed channels and pixel resolution can be adjusted easily (see bottom and right panels). The definition of the DAC outputs and ADC inputs and their volt to real-world physical units is performed with the "Connections" window. Once the inputs are defined, the data to be stored while scanning can be selected in the panel "Image Channels" (see inset). The four auxiliary output channels of *ZI*, i.e. Δf, A_0, A_{exc}, $A_{2f_{\text{ac}}}$, are usually recorded, together with the topography (z-scanner output in nm), the normal deflection (dc bending of cantilever), and the

probe deflection (w-position variation). Further *ZI* digital data channels are output through the USB line. A timing signal on its digital outputs is transmitted in real-time to the digital input/output (DIO) ports of the *NI* real-time PC, together with the measured digital signals through the USB to the PC. These timing signals later allow the PC to decompose the non-real-time digital data stream received through the USB into the pixels of an image recorded on the PC.

2.3.4   Handling of drift and piezo creep issues

For the separation of magnetic and topographical contributions to the MFM image contrast, and for the study of the evolution of the micromagnetic sample state with applied field, successively acquired images need to be aligned. Such a post-acquisition data alignment can in principle be used to compensate slow linear drifts, but image distortions arising from creep that depend on the scan history or drift that changes significantly over time remain difficult to correct.

To allow a post-acquisition point-by-point alignment of different images, a measurement procedure was developed that leads to a reproducible drift- and creep-induced image distortion: the images are scanned in the "Bounce" and "Continuous" mode, i.e. scanning is continuous, and the scan direction is reversed after each completed scan [see Fig. 2.20]. The time for the down scan can then be used to change the applied magnetic field. A $3\,\mu\text{m}\times3\,\mu\text{m}$ MFM-up-scan with 256×256 pixels and scanned with $1\,\text{s}$ per line, for example, takes about $10\,\text{minutes}$. The next up-scan is then acquired with the magnetic field fixed at a pre-selected value. Because the sample is scanned in the bounce mode and the data is always taken during the up-scan, creep and drift induced image distortions become reproducible. Thus a post-acquisition point-by-point linear combination or com-

parison of multiple images becomes possible. We can minimize the effects of piezo creep and successfully subtract consecutive up-scans (even if they are acquired in different fields) for data analysis.

Drifts and creep are more evident at elevated temperatures but also present at low temperatures. For our LT-MFM operated at 10 K, it's typically 0.2-0.3 nm/min in z-axis, i.e. 2-3nm between consecutive images and during the acquisition of one image, due to magnetostriction, different thermal expansion coefficients, etc. Therefore an active tip-sample distance control is needed, especially when the tip scans close to sample surface.

2.4 Cantilever preparation

The deposition of the magnetic layer on the tip side and the reflective coating on the backside of the cantilevers was performed in an UHV DC magnetron sputtering system from AJA International Inc. The typical base pressure prior to deposition is below 1×10^{-8} mbar.

In order to achieve a high force gradient sensitivity in MFM measurements, we utilized uncoated single crystalline silicon cantilevers from *Team Nanotec*. The cantilevers have a nominal stiffness of 0.7 N/m, a typical resonance frequency of about 50 kHz and an *Improved Super Cone (ISC)* tip. The length and width of the cantilever are nominally 225 μm×35 μm.

The tip is made sensitive to magnetic fields by sputter-coating a 3-10 nm thick Co layer (flat substrate equivalent) on a 2 nm Ti adhesion layer on the side of the tip which is facing towards the cantilever support chip [illustrated in Fig. 2.21 a)]. The Co layer is oxidized in air for about 10 minutes to form an anti-ferromagnetic CoO layer, which helps to stabilize the underlying Co layer due to the anti-ferromagnetic
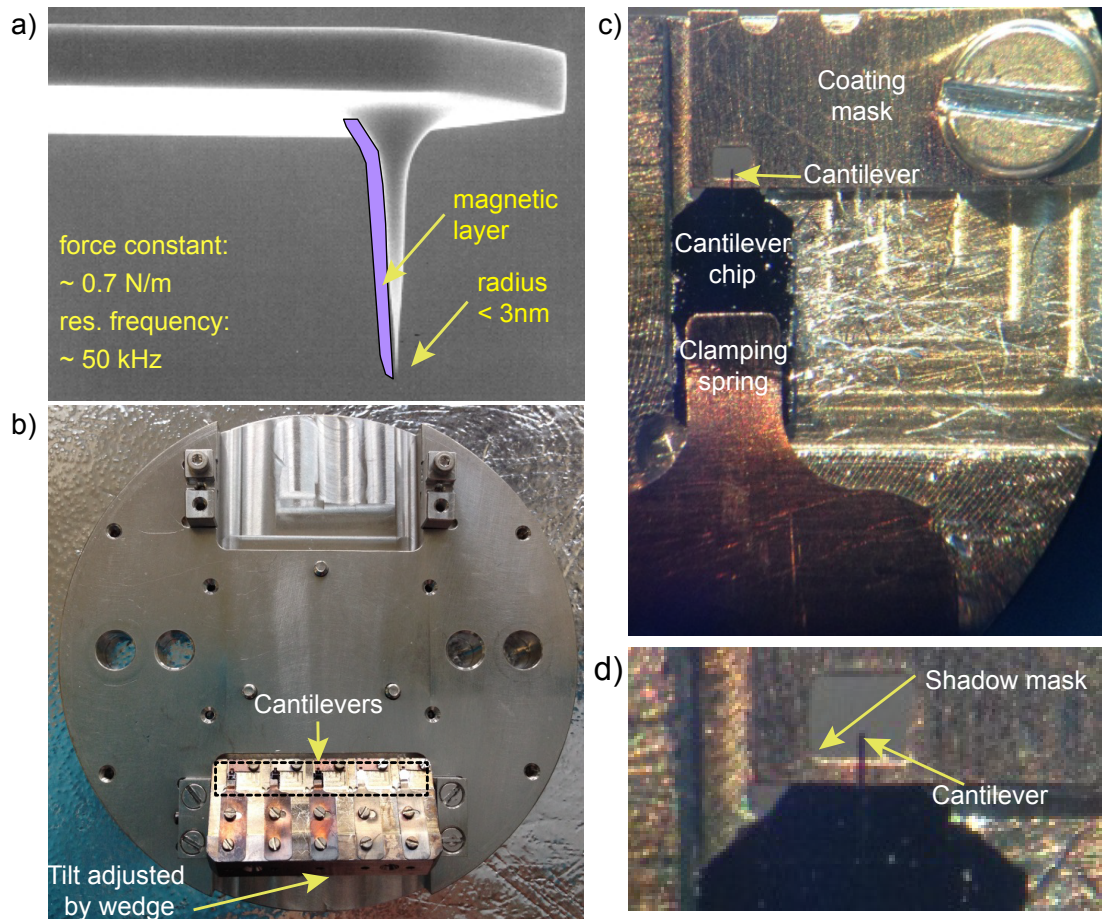
Figure 2.21: a) High-aspect ratio tip with magnetic layer deposited on the tip's backside shown schematically. b) Holding plate for sputter deposition on cantilevers. A total of 5 cantilevers can be mounted and subsequently coated. The tilt angle of cantilevers can be adjusted by inserting an appropriate wedge below the holding plate. c) Zoomed view showing a single cantilever fixed by the clamping spring, and the mask for the deposition of the mirror coating on the cantilever backside. d) Higher magnification image of c).

exchange coupling between them at low temperature. The coated tip is protected against further oxidation by 4 nm of Ti layer. For the magnetic layer deposition, the cantilever is aligned at an angle of about 30° with respect to the sputter target, in order to minimize the thickness of the magnetic layer on the cantilever while still obtaining a sufficiently thick magnetic layer on the side of the tip and on the top of the tip apex. The angle is adjusted by inserting a proper wedge beneath

the cantilever mounting plate, as shown in Fig. 2.21 b). The cantilever is heated for one hour at about 120 °C in the sputtering chamber to remove the water layer, then cooled to room temperature for the deposition of the magnetic layer.

A reflective layer deposited on the backside of the cantilever increases the signal at the interferometer and is advantageous. However, to an extent any films deposited on the back surface of the cantilever degrade the quality factor. Therefore, only the last 50-100 µm towards the free end of the cantilever backside are coated. This is achieved by a shadow mask as shown in Figs. 2.21 c) and d). We utilized Pt as a reflective layer.

2.5 Sample preparation

2.5.1 Sample growth

The samples presented in this thesis were grown by DC magnetron sputtering at room temperature in the same UHV sputtering system from AJA International Inc. used for the coating of MFM cantilevers. The samples were deposited on silicon (100) substrates with a surface oxidized under ambient conditions. The Argon gas pressure during sputtering is typically 2 µbar. The calibration of the sputter rates was obtained using X-ray reflectometry (XRR) performed on calibration samples with a nominal layer thickness between 30 and 50 nm.

Table 2.2 summarizes the deposition rates for the targets and sputter powers used for the samples and cantilevers fabricated in this thesis. For each target, the uncertainty reflects that of the calibration (determined by XRR on films of about 40 nm). For Co, Pt, Ti and Tb targets, a fixed power is often used. The TbFe film was co-sputtered from separate Tb and Fe targets. Because our samples are Fe-rich, different compositions are fabricated by operating the Fe target at different

Element	Power [W]	Rate [Å/s]
Co	15	0.087±0.001
Pt	20	0.238±0.001
Ti	15	0.079±0.001
Tb	15	0.199±0.004
Fe	20	0.076±0.002
	40	0.156±0.002
	60	0.234±0.002
	80	0.312±0.002

Table 2.2: Summary of the deposition rates for the elemental targets used for cantilever and sample preparation.

powers (rates) while keeping the Tb target at the lowest operational power allowing stable sputtering conditions.

Small Si substrates of 2.2 mm×2.2 mm were used for samples to be measured in LT-MFM and VSM, and larger substrates of 15 mm×15 mm for RBS, X-ray diffractometry (XRD), XRR, etc. The substrates were heated in vacuum for one hour at about 120 °C to clean the substrates and remove the water layers. The magnetic layers were deposited at room temperature on a Pt adhesion layer of 5-10 nm, and protected by a Pt capping layer of 3-8.5 nm.

2.5.2   Sample demagnetization

A magnetic thin film with a square hysteresis loop can be in a saturated state (one-domain state) directly after sample deposition. Apart from fields arising from local variations of the areal magnetic moment density, the saturated state does not generate a stray field, and hence no (or only little) magnetic signal is observed in the MFM. Domains were obtained after demagnetizing the sample in an oscillatory magnetic field with an amplitude decaying from 0.8 T to 0 T. The field can be applied perpendicular or parallel to the sample surface.

Note that in many thin film samples with perpendicular anisotropy the equilibrium domain state is defined by an extremely flat energy minimum. Consequently the absolute minimum is difficult to reach, and different demagnetization procedures may generate domain patterns with substantial differences in the size and shape of the domains (see also Te-ho Wu [33]). For some samples (particularly for those with a thin thickness and micron-sized domains), domains with a size convenient for the tip calibration procedure (see Section 2.2.1) can be obtained by an appropriate choice of the demagnetization procedure.

3   Magnetic force microscopy with frequency-modulated capacitive tip-sample distance control

This chapter is composed from the text and figures of the reference [34], published 2018 in *New Journal of Physics*. Authors of this paper are X. Zhao, J. Schwenk, A. O. Mandru, M. G. Penedo, M. Bacani, M. A. Marioni, and H. J. Hug.

3.1   Introduction

As alluded to in the introduction, due to the fact that the high spatial frequency components of the stray field decay rapidly with increasing distance from their source, especially for small spatial wavelengths that are essential for high spatial resolution, the MFM tip is preferably scanned at small tip-sample distances [35, 36, 37, 18]. Typically, retaining sufficient signal to noise at a spatial resolution of 10 nm will require scanning at around 10 nm distance from the surface. At such proximity to the surface the distance must be actively controlled to avoid drifting off the set-point, or collisions with isolated topographical features. Controlling this small distance is challenging because magnetic and non-magnetic forces act on the tip simultaneously [38]. Scanning while maintaining a constant frequency shift would result in a change of tip-sample distance on top of different magnetic domains, as illustrated in Fig. 3.1.

Under ambient conditions, a dual passage method is typically used [38, 39]. In a first scan the intermittent contact mode is used to map the topography of the sample. The latter is then used to scan the magnetic signal with the tip lifted off the surface of the sample. A serious drawback of this technique is being

In non-contact AFM
scanning at constant tip-sample interaction
i.e. constant frequency shift

In MFM
magnetic + topography induced interaction
i.e. tip-sample distance depends on
magnetic interaction
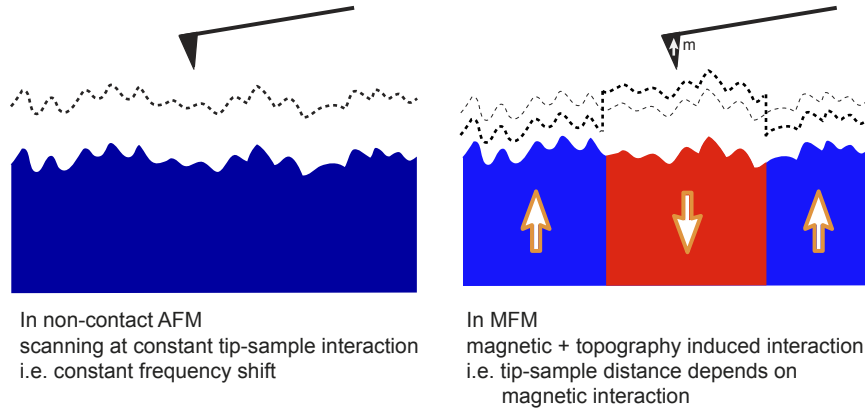
Figure 3.1: Schematics of tip-sample distance control in AFM (left) and MFM (right).

incompatible with operation under vacuum conditions.

We have recently reported two single-passage operation modes, suitable for operation under vacuum conditions. The first method [18] mechanically excites the cantilever oscillation simultaneously on its first and second resonance. Because the oscillation amplitude of the first mode is selected to be more than an order of magnitude larger than that of the second mode, the frequency shift of the first mode reflects the longer-ranged magnetic interactions, while that of the second mode is dominated by the van der Waals forces. The latter contributes mainly when the tip is closest to the sample, given its shorter decay-length. Evidently, the tip must be able to reach close proximity to the surface to map the van der Waals forces. Consequently, the tip-sample distance feedback speed must be sufficiently fast such that the tip can follow the topography on a local scale during the scan. Such a fast tip-sample distance feedback however increases the noise in the tip-sample distance and therefore the noise of the measured magnetic signal that depends on it. Moreover, an operation under constant average tip-sample distance, often used for quantitative data analysis, is not possible when using this method.

56

The second MFM operation method recently described by our group [19] overcomes these limitations. Again, the cantilever is excited mechanically on its first resonance to map the magnetic tip-sample interaction via the shift of the first mode resonance frequency. The second oscillation mode is driven electrostatically using an oscillatory sample bias at half the resonance frequency of the second mode. This generates an oscillatory electrostatic force acting on the tip on the second resonance frequency. The second mode amplitude A_2 can then be used to control the tip-sample distance, z. With sufficiently fast z-feedback parameter, the tip follows the local topography. Alternatively, the z-feedback parameters can be kept slow such that the tip follows the local sample surface slope. Data acquired in this mode facilitates a posteriori quantitative data analysis [26, 40, 41]. The variation of A_2 is a measure of the sample topography and can for example be used to align images measured in different external magnetic fields [19].

However, as already discussed in ref. [19], a tip-sample distance control based on the A_2-signal would fail if the second mode quality factor Q_2 of the cantilever changed. There are various mechanisms that can affect Q_2. We often found that it increases slightly over time, after the cantilever has been introduced to the vacuum system. We attribute this behavior to a reduction of the water layer thickness adsorbed on the cantilever. Q_2 also changes substantially with the applied magnetic field. Stipe et al. [42] showed strong dissipation for cobalt nanowires fabricated on cantilevers with force constants in the μN/m-range with a low intrinsic dissipation, designed for detecting forces on the attonewton scale. Stipe et al. demonstrated that the dissipation of such cantilevers can change by several orders of magnitude when magnetic fields up to 6 T were applied at low temperatures. Later results obtained by Rast et al. [43] looked into the dependence of the frequency shift and

energy dissipation for different hard magnetic particles attached to a cantilever. The decay of the quality factor for fields between 0 and 0.5 T was found to be inversely proportional to the anisotropy constant of the material of the particle, and proportional to its volume. Different from the work of Stipe et al. [42] and Rast et al. [43], the cantilevers used in MFM (and in most scanning force microscopy work) are not perpendicular to the surface but subtend a small angle with the latter, of about 10°. We usually find that the quality factor of such cantilevers creeps over hours after applying stronger fields ($> 500\,\mathrm{mT}$), particularly at lower temperatures. We attribute this slow and hysteretic variation of the quality factor over time to the changes of the magnetostriction of the magnetic layer on the cantilever as its magnetization rotates out of the plane of the cantilever in increasing fields. Furthermore, the magnetization of the tip, or that of the sample, may vary with the oscillating tip-sample distance at locations over the surface where the magnetic tip-sample interaction is a strong. There, additional losses of the energy stored in the cantilever oscillation can take place, which amount to a decrease of the quality factor [44].

3.2   Method

We present a method by which an accurate distance control becomes possible, independently from changes of the quality factor. A schematic of the setup is presented in Fig. 3.2. The cantilever is driven mechanically on the first flexural oscillation mode with a phase-locked loop (PLL) system that tracks changes of the cantilever resonance frequency Δf and also keeps the oscillation amplitude A_0 constant. Changes of the first mode quality factor are thus compensated with an appropriate adjustment of the driving amplitude. Further, the tip-sample bias U_{ac}

is oscillated at a frequency f_{ac} of a few hundred Hz leading to a modulation of the cantilever resonance frequency (see green box in Fig. 3.2).
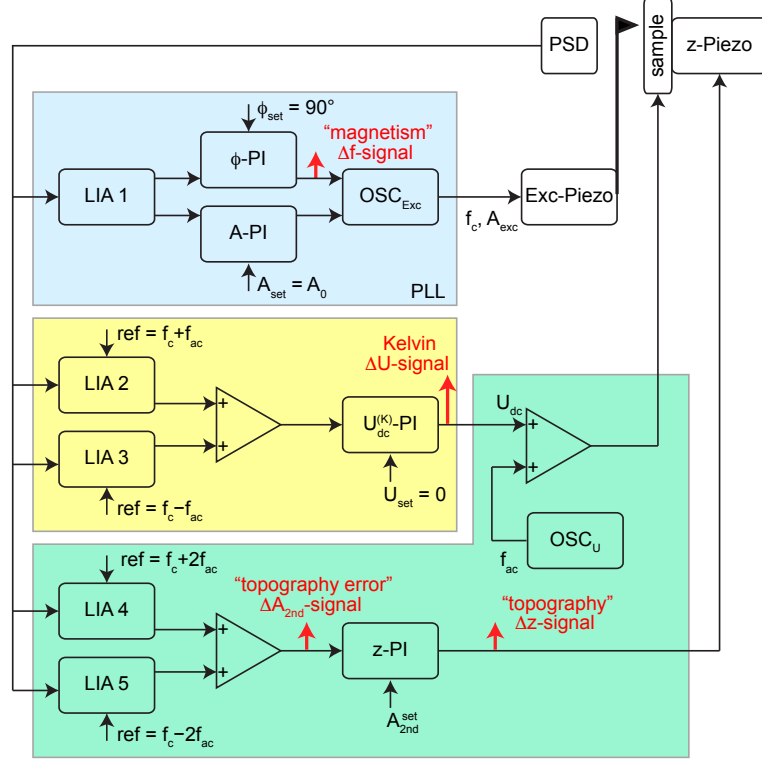
Figure 3.2: Schematics of the PLL and side bands detection systems required for frequency-modulated capacitive distance control in high resolution MFM. The first PLL (blue box) mechanically drives the cantilever on its first flexural mode, f_c, and keeps the oscillation amplitude at A_0. The shift of resonance frequency $\Delta f(x, y)$ is a measure for the magnetic stray field of the sample. The z-feedback (z-PI) adjusts the tip-sample distance to keep the amplitudes of the side-bands at $f_c + 2f_{ac}$ and $f_c - 2f_{ac}$ constant. A measure of the topography is either obtained from the variation of the side-band amplitudes or by the z-feedback output, for slow or fast z-feedback parameters, respectively. The circuitry used for the control of the tip-sample distance is highlighted by the green box. Using two additional lock-in amplifiers (LIA 2 and LIA 3), the two side band amplitudes at $f_c + f_{ac}$ and $f_c - f_{ac}$ can be measured and zeroed by a Kelvin feedback ($U_{dc}^{(K)}$-PI). The latter adjusts the applied bias voltage to compensate the contact potential (yellow box). The setup has been implemented with a Zurich Instruments lock-in amplifier PLL system HF2LI [45] .

A signal $A(t) = A_0 \cdot \cos(\omega_c t)$ which is frequency modulated by $f(t) = A_m \cdot$

$\cos(\omega_{\mathrm{m}}t)$ can be written as

$$
\begin{aligned}
A_{FM}(t) &= A_0 \cdot \mathrm{Re}\left\{e^{i\omega_{\mathrm{c}}t}e^{i\beta\sin\omega_{\mathrm{m}}t}\right\} && (3.1)\\
&= A_0 \cdot \sum_{-\infty}^{\infty} J_n(\beta)\cos(\omega_{\mathrm{c}} + n\omega_{\mathrm{m}})t, && (3.2)
\end{aligned}
$$

where ω_{c} is the carrier frequency, J_n is the n-th Bessel function [46], and β is the modulation index. The spectrum of the frequency modulated (FM) signal (equation 3.2) thus contains an infinite number of side-bands even for a single modulation frequency $\omega_{\mathrm{m}} = 2\pi f_{\mathrm{m}}$. The amplitudes of these spectral components are proportional to the Bessel functions

$$
J_n(\beta) = \sum_{k=0}^{\infty} \frac{(-1)^k (\beta/2)^{n+2k}}{k!(n+k)!}. \tag{3.3}
$$

For our high resolution MFM work, cantilevers with high-aspect ratio tips with a radius smaller than $5\,\mathrm{nm}$, and a resonance frequency f_0, of the order of $50\,\mathrm{kHz}$, are used. To minimize the non-magnetic contribution of the tip-sample force, the contact potential $U_{\mathrm{dc}}^{(\mathrm{K})}$ is compensated. We find that for an applied bias deviating $500\,\mathrm{mV}$ from the contact potential, i.e. for $U_{\mathrm{dc}}^{(\mathrm{a})} = U_{\mathrm{dc}}^{(\mathrm{K})} \pm 500\,\mathrm{mV}$, the electrostatic force gradient-induced frequency shift, Δf_{E}, remains smaller than $5\,\mathrm{Hz}$ at a tip-sample distance of $10\,\mathrm{nm}$ [see Fig. 3.3 a)].

For $f_{\mathrm{m}} = f_{\mathrm{ac}} = 1\,\mathrm{kHz}$ the modulation index $\beta = \Delta f_{\mathrm{E}}/f_{\mathrm{m}}$ thus remains smaller
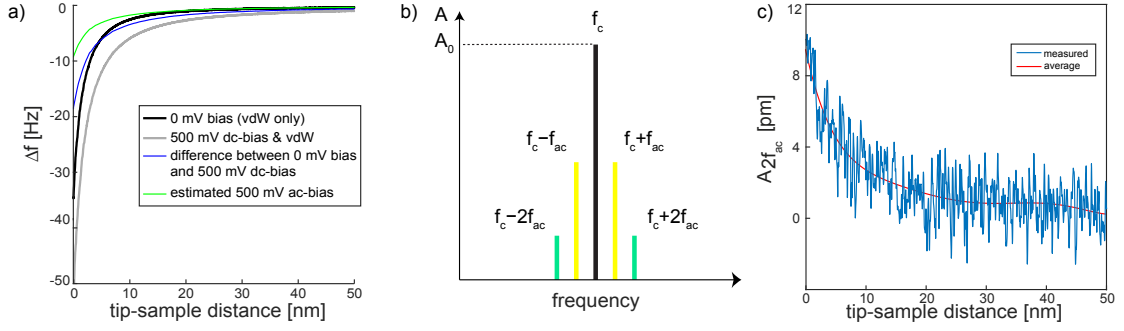
Figure 3.3: a) Frequency shift as a function of the tip-sample distance with zero bias (black line) and with an applied dc-bias of $500\,\mathrm{mV}$ (gray line). The blue curve displays the difference between these curves and thus measures the contribution of the electrostatic force arising from a $500\,\mathrm{mV}$ dc-potential to the frequency shift. The frequency shift arising from the $500\,\mathrm{mV}$ ac-potential (green line) can be approximated by taking the electrostatic force contribution (blue curve) and scaling it to the effective value for the ac-modulation bias. b) Schematics of the spectrum of a cantilever oscillation frequency modulated with a bias amplitude $U_{\mathrm{ac}} = 500\,\mathrm{mV}$. Because the electrostatic force contains components with frequency f_{ac} and $2f_{\mathrm{ac}}$, the FM-spectrum shows two groups of side bands at $f_{\mathrm{c}} \pm f_{\mathrm{ac}}$ and at $f_{\mathrm{c}} \pm 2f_{\mathrm{ac}}$. Higher order side-bands are below the noise floor and can therefore be neglected for small modulation indices (see main text). c) Measured side-band amplitude $A_{2f_{\mathrm{ac}}}$ as function of tip-sample distance.

than $5 \cdot 10^{-3}$. The Bessel functions in equation 3.2 can then be approximated by

$$
J_0(\beta) \;\; = \;\; 1 - \frac{\beta^2}{4} + \frac{\beta^4}{32} - ... \approx 1 - \frac{\beta^2}{4} \tag{3.4}
$$

$$
J_1(\beta) \;\; < \;\; \beta, \; \text{with} \; \lim_{\beta \to 0} J_1(\beta) = \frac{\beta}{2} \tag{3.5}
$$

$$
J_n(\beta) \;\; < \;\; \left(\frac{\beta}{2}\right)^n \quad \text{for } n > 1, \tag{3.6}
$$

$$
J_{-n}(\beta) \;\; = \;\; J_n(\beta) \cdot (-1)^n \quad \text{for } n > 0. \tag{3.7}
$$

For $\beta < 10^{-2}$, the spectrum of the frequency modulated signal [Fig. 3.3 b)] thus contains the carrier frequency and two side bands at $f_c \pm f_m$. The amplitude of these side bands, $A_0 \cdot J_1(\beta)$, is more than β times smaller than that of the carrier signal A_0 (typically $5\,\mathrm{nm}$). Higher order side-bands have correspondingly smaller amplitudes (see Eq. 3.6) such that, in practice, they are below the noise floor of

the deflection detector and can be neglected. Note that the side band at $f_c - f_m$ has a phase shift of $-\pi$ compared to the one at $f_c + f_m$ (see Eq. 3.7).

The electrostatic force acting on the tip is given by

$$
\begin{aligned}
F_{\mathrm{E}}(z,t) &= \frac{1}{2}\frac{\partial C(z)}{\partial z} \cdot [U_{\mathrm{dc}} + U_{\mathrm{ac}}\cos(2\pi f_{\mathrm{ac}}t)]^2 \\
&= \frac{1}{2}\frac{\partial C(z)}{\partial z} \cdot [\, U_{\mathrm{dc}}^2 + 2U_{\mathrm{dc}}U_{\mathrm{ac}}\cos(2\pi f_{\mathrm{ac}}t) \\
&\quad + \; U_{\mathrm{ac}}^2\cos^2(2\pi f_{\mathrm{ac}}t)\,]\,,
\end{aligned}
\tag{3.8}
$$

where $U_{\mathrm{dc}} = U_{\mathrm{dc}}^{(\mathrm{K})} + U_{\mathrm{dc}}^{(\mathrm{a})}$ is the sum of the contact potential and applied potential, U_{ac} is the amplitude of the potential modulation, and $C(z)$ is the distance dependent tip-sample capacitance that in principle can be calculated if the tip geometry is known [47]. Equation (3.8) shows that F_{E} has a dc-component proportional to U_{dc}^2, and components at frequency f_{ac} and $2f_{\mathrm{ac}}$. The carrier frequency can be expressed as $f_{\mathrm{c}} = f_0 + \Delta f_{\mathrm{vdw}} + \Delta f_{\mathrm{E}} + \Delta f_{\mathrm{mag}}$, where f_0 is the free resonance frequency of the cantilever, Δf_{vdw} and Δf_E are the frequency shifts arising from van der Waals and dc-part of the electrostatic force, respectively, and Δf_{mag} depends on the magnetic tip-sample interaction. The two ac-components of the electrostatic force generate two groups of first-order side bands at $f_{\mathrm{c}} \pm f_{\mathrm{ac}}$ and $f_{\mathrm{c}} \pm 2f_{\mathrm{ac}}$ [Fig.Fig. 3.3 b)]. Note that the side bands at $f_{\mathrm{c}} \pm 2f_{\mathrm{ac}}$ are the first order side bands of a modulation at the frequency $2f_{\mathrm{ac}}$, and *not* the second order side bands of a modulation at the frequency f_{ac}, because $J_n = 0$ for $n > 1$ (see Eq. 3.6).

The amplitudes of the side bands at $f_{\mathrm{c}} \pm 2f_{\mathrm{ac}}$ are given by

$$
A_{2f_{\mathrm{ac}}} \propto A_0 \cdot J_1(\beta) \approx A_0 \cdot \frac{\beta}{2},
\tag{3.9}
$$

where the approximation is valid for small β. Similar to our previous work [18],

we use the amplitudes of the second side bands at $2f_{\mathrm{ac}}$ for the distance control, because their amplitudes are independent of U_{dc}, and therefore of the contact potential difference. Provided that the tip-sample capacitance and its dependence on tip-sample distance are known, β can be calculated as

$$\beta = \frac{U_{\mathrm{ac}}^2}{4\pi k_{\mathrm{c}}} \cdot \underbrace{\int_{-A_0}^{A_0} \frac{d^2C(z+A_0-q)}{dz^2} \cdot \frac{\sqrt{A_0^2-q^2}}{2A_0^2}\,dq,}_{:= \left\langle \frac{d^2C(z+A_0)}{dz^2} \right\rangle_{-A_0}^{+A_0}} \qquad (3.10)$$

where k_{c} is the first mode force constant of the cantilever. Thus the amplitude $A_{2f\mathrm{ac}}$ is a proxy for the tip-sample distance, and can be used for tip-sample distance control (see the area highlighted by the blue color in Fig. 3.2). Note that as long as the carrier signal amplitude, i.e. the fundamental mode oscillation of the cantilever A_0, is kept constant by the amplitude feedback, the side-band amplitudes are independent of changes of the quality factor Q.

The side-band amplitude $A_{2f_{\mathrm{ac}}}$ as function of the tip-sample distance is plotted in Fig. 3.3 c). There are two modes of tip-sample distance control, i.e. constant average distance mode and constant local distance mode. For both modes the slope of the sample surface is corrected using "Plane Correction" implemented in *Scanit* software [Fig. 2.20]. For the constant average distance mode, a slow z-feedback is used to correct the drift of tip-sample distance due to piezo drift and uncompensated sample plane slope. The slow feedback speed has the advantage that minimal noise is added to the MFM Δf signal. For the constant local distance mode, a fast z-feedback is used to rapidly adjust z-output to follow the local topography of the sample surface. The limited signal-to-noise ratio (SNR) of $A_{2f_{\mathrm{ac}}}$ signal makes it not an ideal feedback parameter in this case.

3.3 Results

In order to test the performance of frequency-modulated capacitive distance control method discussed in section 3.2, we used a low temperature magnetic force microscope operated in UHV [48]. The system contains a superconducting solenoid magnet that can provide magnetic fields up to 7 T. As already mentioned in Section 2.4], we utilized uncoated silicon cantilevers from Team Nanotech GmbH with resonance frequency of about 50 kHz and nominal stiffness of 0.7 N/m. The cantilever backside was coated with Pt to increase the optical reflectivity and signal-to-noise ratio of our fiber-optical interferometer system. The sharp high-aspect ratio tip was made sensitive to magnetic stray fields with a coating of 2 nm Ti and 6.5 nm Co (nominal thickness) coated on the back side of the tip at an angle of about 30° with respect to the cantilever surface. The sputter deposition for cantilevers and samples (described in the following two subsections) was performed in a UHV DC magnetron sputtering system from AJA International Inc. The typical base pressure prior to deposition is 1×10^{-8} mbar or better.

3.3.1 Magnetic force microscopy in the case of strong tip-sample interaction

The frequency shift contrast in magnetic force microscopy arises from the interaction of the tip magnetization with the stray field of the sample or, conversely, from that of the tip stray field with the magnetization of the sample [49]. It is convenient to use low enough magnetic moment tips with high magnetic coercivity such that to a good approximation, neither tip nor sample magnetization is significantly affected by their proximity. The MFM contrast can then be calculated as a convolution of the tip magnetization with the gradient of the sample stray field

and methods for a quantitative analysis of the measured frequency shift data can be applied [22, 26].
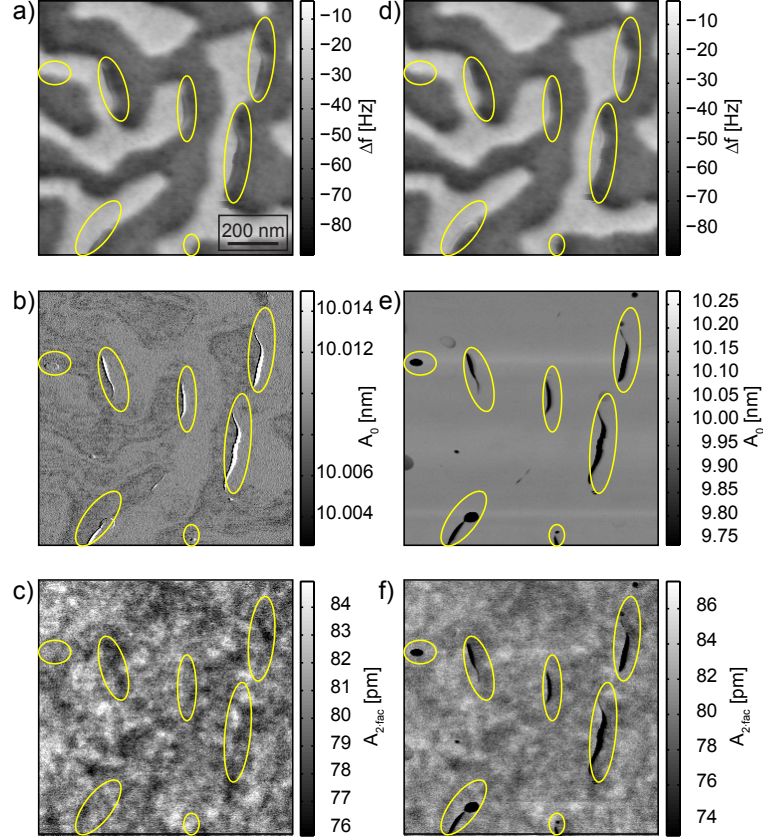
Figure 3.4: a) and d) MFM images recorded with a fast and slow feedback of the fundamental oscillation mode amplitude A_0, respectively. The strong tip-sample interaction near the domain walls (e.g. at the yellow ellipses) leads to changes of tip/sample magnetization that lower the quality factor of the cantilever. b) For a sufficiently fast amplitude feedback, A_0 remains constant within ± 5 pm around the setpoint of 10 nm. c) The sum of the side band amplitudes then reflects local variations of the tip-sample distance arising from the topography of the sample. e) For a slow amplitude feedback, the amplitude A_0 is significantly smaller at the locations with lower Q. f) The side band amplitudes are also affected by the variations of A_0.

Here we designed an experiment where the tip scans over a sample whose domains generate a stray field that is strong enough to affect the micromagnetic state of the tip near some of the domain walls. Energy dissipation of the oscillat-

ing cantilever can therefore occur, leading to an increase of the amplitude of the cantilever excitation A_{exc} if the micromagnetic state switches periodically between two states over an oscillation period of the cantilever; in this case Q_2 will have changed. We used a magnetic multilayer sample that exhibits perpendicular magnetic anisotropy, specifically $(\text{Si}_{\text{ox}}/\text{Pt}(5\text{nm})[\text{Co}(0.4\text{nm})/\text{Pt}(0.7\text{nm})]_{15}/\text{Pt}(2\text{nm}))$ [50]. The sample was DC magnetron sputtered at room temperature in a $2\,\mu\text{bar}$ Ar atmosphere onto a naturally oxidized Si substrate. The deposition rates of Co and Pt were $0.09\,\text{\AA}/\text{s}$ and $0.24\,\text{\AA}/\text{s}$, respectively.

Figs. 3.4 a) and d) depict MFM frequency shift data obtained with a fast and slow speed of the amplitude feedback (A-PI in the blue box of Fig. 3.2). The yellow ellipses highlight some of the areas of the domain walls where instabilities of the micromagnetic state of the tip occur. Figures 3.4 b), e) and Figs. 3.4 c), f) compare the fundamental mode oscillation amplitude A_0 of the cantilever (nominally 10 nm) and the sum of the amplitudes of the (second) side bands at $f_{\text{c}} \pm 2f_{\text{ac}}$, respectively; the actual f_{c} is the fundamental mode resonance frequency of the cantilever [note that $\Delta f = f_0 - f_c$ is plotted in panels a) and d)]. For a sufficiently fast amplitude feedback, the fundamental mode oscillation amplitude A_0 [Fig. 3.4 b)] deviates less than $\pm 5\,\text{pm}$ from the setpoint value of 10 nm. Then the sum of the amplitudes of the side bands at $f_c \pm 2f_{\text{ac}}$ solely reflects topography-induced changes of the tip-sample distance [granular contrast visible in Fig. 3.4 c)]. This is no longer true for lower speeds of the amplitude feedback. In that case, A_0 deviates significantly from its setpoint at the locations over the domain walls where energy dissipative processes occur [yellow ellipses in Fig. 3.4 e)], leading to a decrease of $A_{2f_{\text{ac}}}$ (see Eq. 3.9). For a slow z-feedback, the distance (defined as the lowest point in an oscillation cycle of the cantilever) becomes larger at locations of

decreased oscillation amplitude A_0, resulting in a further reduction of $A_{2f_{ac}}$ amplitude (Eq. 3.9). These effects explain the strong relative contrast highlighted by the yellow ellipses in Fig. 3.4 f). Clearly, our frequency-modulated capacitive distance control method is valid even in the presence of energy dissipative processes, as long as the fundamental mode oscillation amplitude A_0 is kept constant.

3.3.2 Magnetic force microscopy in magnetic fields

Domains have been imaged in magnetic fields up to a few hundred mT by MFM already in 1995 by Manalis et al. [51], and by Proksch et al. [52]. Both groups performed MFM under ambient conditions using lift-mode operation [38, 39] to control the tip-sample distance.

As alluded to previously, for magnetic force microscopes operated under vacuum conditions, the high quality factor increases the sensitivity but precludes the use of the intermittent contact mode for tip-sample distance control. Instead, many early MFM experiments performed in vacuum used the measured frequency shift for the distance feedback. Then contours of constant frequency shift were recorded. Alternatively, slow z-feedback parameters or an additional servo-force generated by an applied tip-sample bias [13] can be used, such that the tip-sample distance can be kept small and the tip scans roughly parallel to the average sample slope. The latter can also be achieved when the z-feedback is stopped and the average sample slope is compensated [32, 53, 54].

The application of higher magnetic fields ($> 500\,\mathrm{mT}$) deflects the cantilever, and changes its resonance frequency substantially [even for the thin magnetic coatings used here, as can be seen in Fig. 3.7 c)]. Moreover, we have often observed the resonance frequency to creep over tens of minutes after a change of the applied

field from zero to more than one Tesla. In fact, in order to prevent a crash of the tip into the surface, the tip is typically retracted from the surface before the field is changed. The tip must then be re-approached to the surface, and the feedback setpoint must be re-set (if a feedback is used) before further MFM data can be acquired [55, 56]. This makes reproducible MFM measurements in strong fields challenging, and presumably explains why only a few studies on MFM operated in fields of several Tesla have been reported to date [57, 58]. Yet such strong fields are required, e.g., for the study of samples exhibiting exchange bias effects [59], or for the analysis of the magnetization behavior of $L1_0$-FePt phase recording materials [60], exchange coupled media, and ferro/ferrimagnetic bilayers exhibiting giant exchange bias effects [61].

Figure 3.5 shows the dependence of the frequency shift with the tip kept 5 nm (blue solid line) and several hundred nanometers (red dashed line) from the sample surface. For both curves Δf decreases between 0 and 500 mT, and increases between 500 mT and 1 T, then decreases rapidly from 1 to 2 T, then increases slowly until 7 T. The two curves appear almost identical apart from a vertical shift of about 3 Hz, proving that the observed frequency shift arises from the interaction of the cantilever with the applied field, and that the tip-sample interaction can be neglected.

It is therefore important to quantify the effects from applied fields and assess the ability of the present method to compensate for changes of the resonance frequency and quality factor of the cantilever. We select a high coercivity material system with perpendicular anisotropy to discuss the MFM performance in applied fields up to 7 T. Specifically, we work at 10 K on a $\mathrm{Si_{ox}}$/Pt(10nm)/TbFe(20nm)/Pt(3nm) film, where the Tb content is 25 % (atomic ratio). The TbFe film was DC mag-
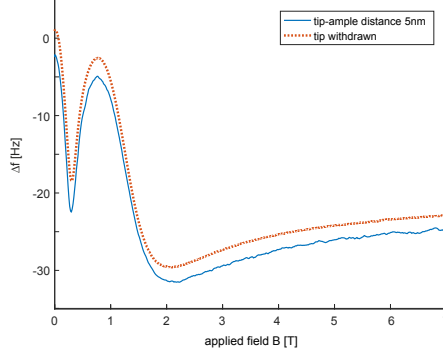
Figure 3.5: Measured frequency shift Δf as function of applied external field, for tip kept 5 nm (blue line) and withdrawn (red dashed line) from the sample surface.

netron deposited by co-sputtering from separate Tb and Fe targets, with deposition rates of 0.20 Å/s and 0.22 Å/s, respectively. Vibrating sample magnetometry (VSM) measurements (not shown) that we performed on this sample exhibit a strong perpendicular magnetic anisotropy and a high coercive field of about 5.4 T at 10.5 K. The high coercivity allows the study of the domain pattern in fields of several Tesla and the comparison of MFM data acquired in different fields.

Figs. 3.6 a) and b) depict MFM data acquired with a side band amplitude setpoint of 4.5 pm corresponding to a tip-sample distance of $z = 5$ nm in zero field with up and down tip magnetization, respectively.

The tip magnetization was set by the application of a field of ± 50 mT. The MFM data acquisition was performed with a slow z-feedback that keeps the average second side-band amplitude thus the average tip-sample distance constant. The feedback then compensates for distance changes for example arising from the deflection of the cantilever in an applied magnetic field or thermal drift, but not for local variations of the tip-sample distance arising from the topography. The contrast arising from a magnetic interaction between the tip and the domains inverts with the direction of the tip magnetization, but the contrast from topography-
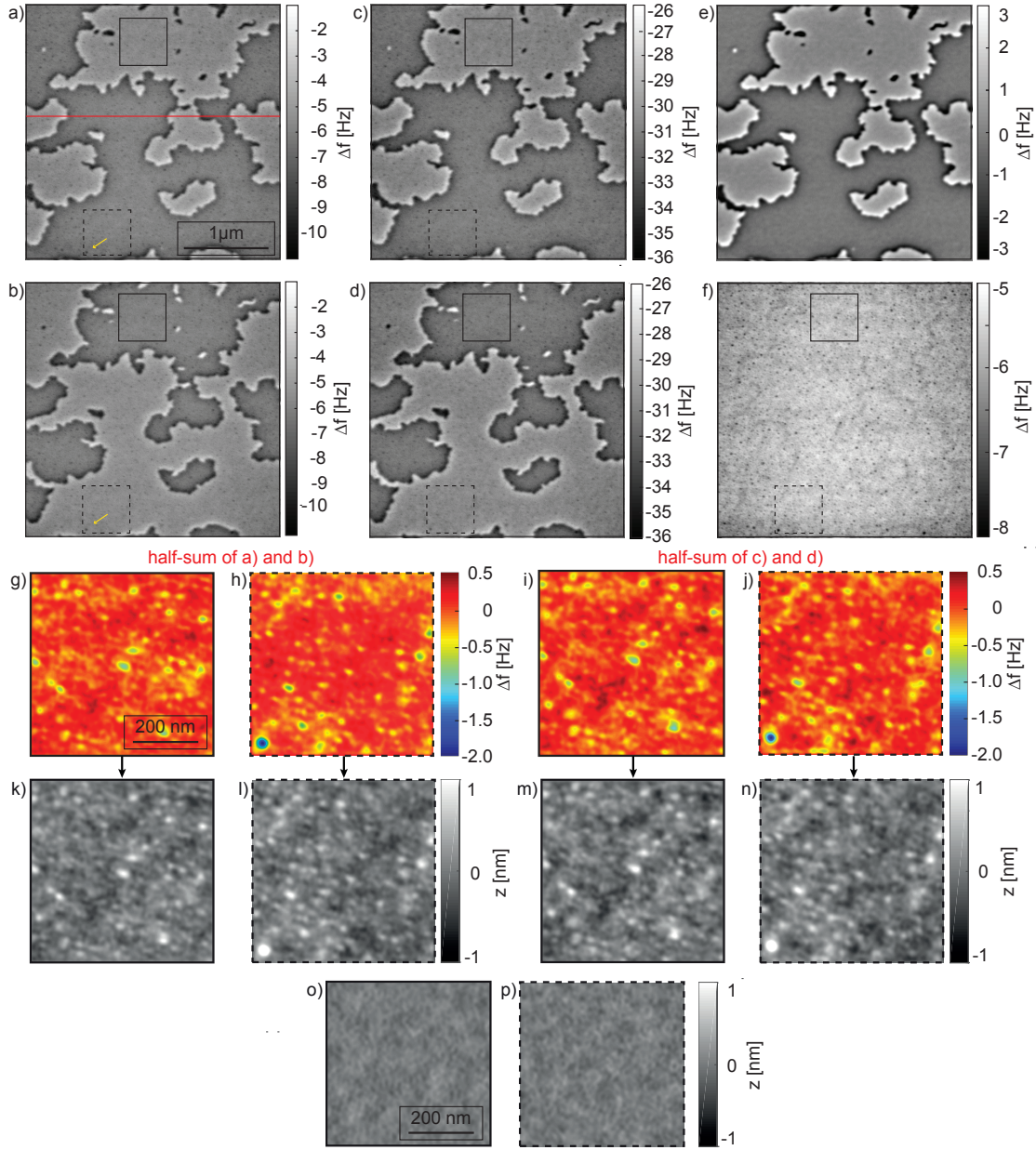
Figure 3.6: a) and b) MFM images acquired at 0 T with up and down tip magnetization, respectively. The contrast is dominated by the stray field of the micron-sized domains, while faint dark spots are also visible. The latter arises from increased attractive van der Waals and electrostatic forces caused by a locally reduced tip-sample distance at protrusions on the surface (see for example the dark spot highlighted by the yellow arrows). c) and d) MFM images acquired at 4 T with opposite tip magnetization. e) and f) Half-difference and half-sum of the data shown in a) and b). g), h) and i), j) Half-sums of the data in the areas highlighted by the solid and dashed squares, from a), b), and c), d), respectively. k) to n) topography data obtained from the frequency shift data g) to j) convoluted with the frequency shift versus distance data [see green line in Figure 3.3 a)]. o) and p) Differences of the data displayed in k), m), and l), n), respectively.

induced variations of the van der Waals and electrostatic forces appears as small and faint dark spots independent of the magnetization direction of the tip [e.g. the dark spot in the dashed black square highlighted by the yellow arrows in Figs. 3.6 a) and b)]. The electrostatic forces are minimized by the compensation of the contact potential, but the modulation of $\pm 500\,$mV around the compensation potential generates an average electrostatic force that depends on the local tip-sample distance. The frequency shift generated by the $500\,$mV ac-potential [green line in Fig. 3.3 a)] is about half of that arising from a $500\,$mV dc-potential [blue line in Fig. 3.3 a)], because the time-averaged electrostatic force is proportional to the square of the effective value of the $500\,$mV ac-potential. The frequency shift arising from the capacitive force is roughly equal to that of the van der Waals force.

The magnetic and topographic contributions to the measured contrast can be disentangled by taking the half-difference [Fig. 3.6 e)] and half-sum [Fig. 3.6 f)] of data shown in panels a) and b), respectively. A pattern of extremely faint lines reminiscent of the domain walls is visible in Fig. 3.6 f). It arises either from a non-perfect alignment of the data before the summing, or from an extremely weak change of the magnetization of the tip or sample caused by their magnetic interactions. Apart from this, the well-visible dark dots arise from the (small) sample roughness. These topographical contributions to the measured contrast become better visible when the data is displayed in color [Fig. 3.6 g) and h)], and at a smaller scale [see areas highlighted by the solid and dashed squares in panels a), b) and f)].

The topography data obtained from the half sum of $4\,$T data [from the areas highlighted by the solid and dashed squares in panels c) and d)] is displayed in Figs. 3.6 i) and j), where the frequency shift offset has been removed. They

look identical to those obtained from the zero field data in Figs. 3.6 g) and h). Figs. 3.6 k) through n) display the topography (approximately ± 1 nm obtained from the convolution of the frequency shift versus distance data [from the van der Waals and electrostatic forces displayed in Fig. 3.3 a)] and the topography-induced frequency shift data [displayed in Figs. 3.6 g) through j)]. To estimate the deviation of the tip-sample distance between data taken at 0 T [Figs. 3.6 a) and b)] and 4 T [Figs. 3.6 c) and d)], the differences between the data in the panels k) and m), and l) and n), respectively, are calculated. The results are displayed in panels o) and p), where the edges are cut-off due to alignment of images measured in different fields. The maximum deviation is about ± 0.4 nm over the displayed image size of $493 \times 493\,nm^2$. The RMS deviation is 0.12 nm. Note that the feedback typically adjusts the sample z-position by about 2-3 nm during the acquisition of one image (10 minutes) to compensate for the z-drift of the instrument. For the acquisition of the images taken in a field of 4 T the feedback changes the sample z-position by 14 nm to keep the tip-sample distance constant despite the drift of the instrument (over 126 minutes), and the bending of the cantilever in the applied field. This demonstrates the robustness of the distance control in applied fields.

The hysteresis loop of high coercive materials with perpendicular magnetic anisotropy like amorphous TbFe-alloys can be several Tesla wide whereas the switching occurs within a few tens of milli-Tesla [62]. Besides allowing the separation of topographical and magnetic signals, measurements in different applied fields can be used to analyze a reversal process with a high level of local detail. Typically, in order to observe domain nucleation and the successive wall motion, a large number of MFM images must be acquired at small increasing field intervals, such that the different steps in the reversal process can be captured. The switching

field would be more conveniently assessed by ramping the magnetic field while the same line is repeatedly scanned. We have already discussed, however, that the application of magnetic field would lead to additional energy dissipation, deflection of the cantilever and shift of its resonance frequency [42], rendering the method impractical if the field exceeds few hundred mT and the tip-sample distance is to be maintained nearly constant.

Figure 3.7 a) depicts repeated scans of the red line indicated in Fig. 3.6 a) in a magnetic field that increases from 0 to 7 T with 194 mT/minute, at a tip-sample distance of 14.3 nm. As found before [compare Figs. 3.6 a) and c)], the applied field leads to a strong variation of the background frequency shift [Fig. 3.7 c)] of approximately 30 Hz that dominates the 5 Hz contrast arising from the magnetic forces. Frequency shift of scanlines taken in different fields are displayed in Fig. 3.7 b). Note that the dependence of the background frequency shift on the field is not monotonic [Fig. 3.7 c)] indicating that the magnetization processes of the different parts of the the magnetic layer on the cantilever and on the tip contribute to the background frequency shift. The blue curve in Fig. 3.7 d) shows the excitation amplitude A_{exc} as a function of the applied field B. Interestingly, the highest dissipation does not occur in the highest field but at the relatively moderate field of 299 mT, where a first local minimum of the frequency shift is observed [see Fig. 3.7 c)]. The amplitude feedback (A-PI in the blue box shown in Fig. 3.2) operates sufficiently fast to keep the deviation of the amplitude from its setpoint of 5003 pm within less than 1 [red curve in Fig. 3.7 d)]. When the field is increased from 0 to 299 mT the z-piezo retracts the sample by about 57 nm [blue curve in Fig. 3.7 e)] predominantly to compensate the deflection of the cantilever [blue curve in Fig. 3.7 f)]. The speed of the z-feedback is slightly too slow to
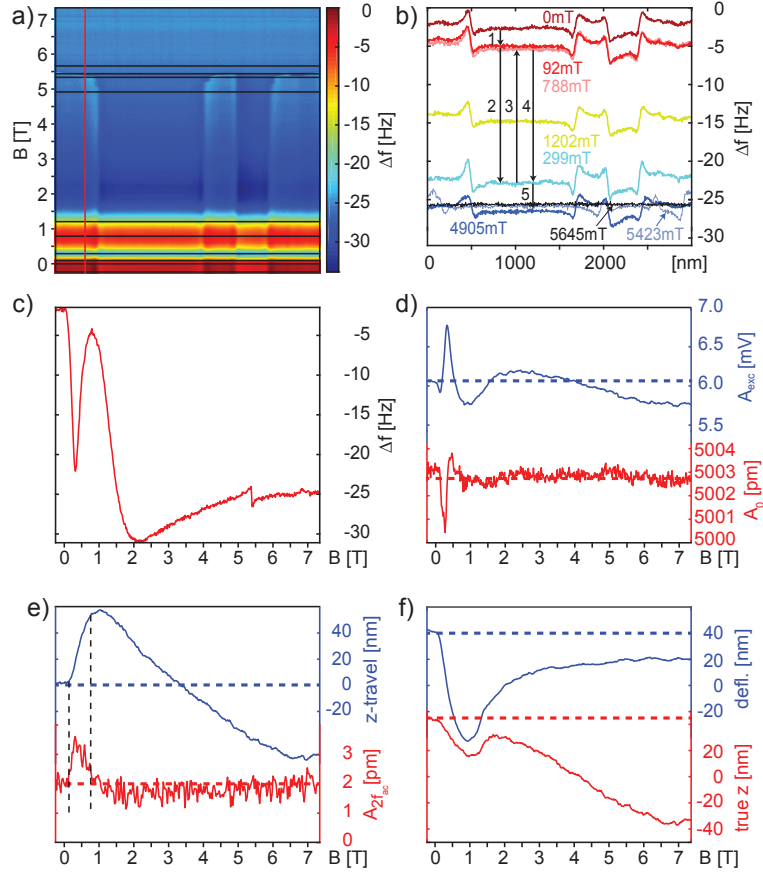
Figure 3.7: a) MFM data acquired at the location of the horizontal line crossing bright and dark domains in Fig. 3.6 a). b) Scanlines obtained in various magnetic fields corresponding to the horizontal black lines in panel a). c) Background frequency shift, i.e. the vertical red line in panel a), as a function of the applied field. d) Excitation amplitude A_{exc} (blue curve) and cantilever oscillation amplitude A_0 (red curve), measured simultaneously with frequency shift Δf during the image scan. e) Recorded travel of the z-piezo and side-band amplitude. f) Measured cantilever deflection (blue) and true z (red) which is deduced from the former and the z-travel.

keep the tip-sample distance constant, so that the measured side-band amplitude $A_{2f_{\text{ac}}}$ increases from about 2 pm to 3 pm [red line in Fig. 3.7 e)] corresponding to a decrease of the tip-sample distance from 13 nm to 8 nm. In principle, we could use a faster z-feedback, but at the cost of Δf signal-to-noise ratio. Since there is no resonance amplification of the electrostatic force at the bias oscillation frequencies

f_{ac} or $2f_{ac}$, and the amplitudes of the side bands are proportional to $J_1(\beta)$ which is approximately equal to $\beta/2$ (see Eq. 3.5). Hence, the side band amplitude and thus the signal-to-noise ratio remains small. This limits the speed of the z-feedback such that the tip cannot follow the local topography with an acceptably small error signal.

A comparison of the cantilever deflection [blue curve in Fig. 3.7 f)] with the z-piezo travel [blue curve in Fig. 3.7 e)] confirms that the z-piezo travel compensates the field-induced cantilever deflection to keep the tip-sample distance constant for fields below 2 T. In the field range from 2 to 7 T the cantilever deflection approaches a saturation at about $+18$ nm, while the z-piezo travel becomes proportional to the applied field up to about 6 T before a saturation at about -58 nm occurs. Thus the z-piezo travel is larger than the cantilever deflection for fields above 3 T, suggesting that the field also affects the tip-sample distance directly through a deformation of parts of the microscope. These contributions are disaggregated in Fig. 3.7 f). We can see that the proposed distance control method is able to provide insight into the various mechanisms contributing to the energy dissipation, and could conceivably be used for local characterization of the dissipation processes in thin magnetic films.

3.4   Conclusions

Our results demonstrate that average tip-sample distances in the range between a few nm and several tens of nm can be kept essentially constant, even during applied field ramps, at least when the height of topographical features does not exceed a few nm. Provided that the feedback is set to keep the fundamental oscillation mode amplitude constant, we show that the method is effective also when the

quality factor of the cantilever unexpectedly changes, so that the distance control is unaffected by dissipative processes. This capability is crucial for the study of TbFe ferrimagnets and exchange-coupled double layers based on TbFe, as we describe in the following chapters. More specifically, this is the basis for a pixel-by-pixel quantitative comparison of measurements carried out in different applied fields. Thus local characteristics of the reversal process become accessible.

4 Amorphous rare earth-transition metal (RE-TM) ferrimagnetic thin film TbFe

4.1 Introduction

The rare earth (RE)-transition metal (TM) alloy films are generally ferrimagnetic due to the antiferromagnetic exchange-coupling between the TM and heavy-RE atoms [63]. The magnitude of the component RE and TM magnetic moments of these ferrimagnets depend differently on temperature. At the compensation temperature T_{comp}, the total magnitudes of the RE and TM magnetic moments are equal, and the material effectively resembles an ordinary antiferromagnet (AF). At all other temperatures below the Curie temperature, the opposing moments have different magnitudes and the material has a net magnetization. So by changing the composition of RE-based amorphous materials, the compensation temperature and the Curie temperature can be adjusted, and the magnetic properties may be tailored to device specifications [64]. A further interesting characteristic of many types of RE-TM alloys in thin film form is that they have perpendicular magnetic anisotropy (PMA) for various substrates on which they have been grown. This and a low magnetization result in comparatively large coercivities that make them interesting systems e.g. for magnetic recording.

The origin for PMA for this material is not established definitively. While the compressive strain in sputtered TbFe films arising from implantation of neutral Ar was found to contribute to the PMA, Takagi et al. [3] and Mizoguchi et al. [65] concluded that atomic-scale structural anisotropy (ASA) or pair-ordering may be the main source for PMA. The detection of this ASA was made possible only with the availability of advanced synchrotron-based x-ray methods. Harris et al.

determined an ASA in amorphous TbFe films via the extended x-ray absorption fine structure (EXAFS) [66]. Using thermal annealing to reduce the strong PMA obtained after growth, they showed ASA to be the dominant mechanism for the strong PMA. In 2001 Harris et al. showed that selective resputtering of surface adatoms during film growth induced pair-order anisotropy [67] and linked it to the PMA.

The industrial interest in the coupling of magnetic layers with different properties (for giant magnetoresistance (GMR), tunneling magnetoresistance (TMR) sensors, exchange-coupled and perpendicular media) has been a further driving force for research in this field. For example, after the first demonstration of 55 % TMR ratio in a GdFeCo and TbFeCo basidesed perpendicular tunnel junction (p-MTJ) in 2002 [68], there has been growing interest in RE-TM amorphous films for p-MTJ applications [69] [70].

The present chapter focuses on thin amorphous TbFe films (sample $S1$) as a particular RE-TM system, which we study as the basic component of the exchange-coupled double layers (ECDLs) (samples $S2$-$S7$, see also Section 5.2) with tunable exchange-coupling and exchange-bias fields up to 1.1 T.

4.2   Sample fabrication, composition, and chemical analysis

We fabricated an amorphous TbFe film of 20 nm thickness on silicon (100) substrates with a thermally oxidized layer (Si): $Si_{ox}/Pt_{10nm}/TbFe_{20nm}/Pt_{8.5nm}$. It was DC magnetron sputtered at room temperature in an UHV AJA Orion sputtering system with an Argon gas pressure of 2 µbar. The substrates were rotated during deposition to improve sample homogeneity.

The nominal Tb and Fe contents are 25 % and 75 % (atomic ratio), with de-

position rates of 0.20 Å/s and 0.22 Å/s, respectively, at the power level used for sputtering (15 W and 56 W respectively). The TbFe films were measured by XRD where no crystalline structures were observed, and thus confirmed to be amorphous.

The overall composition of the TbFe thin film (*S1*) was determined by RBS. The measurements were carried out by Max Doebeli at ETH Zurich[1]. For sample *S1*, the measured atomic ratio of 26.5±1.5 % Tb and 73.5±15 % Fe is close to our nominal values achieved by co-sputtering from rate-calibrated separate targets.

The TbFe film (sample *S1*) was investigated by TEM for structural and chemical analysis. The TEM measurements were carried out by the group of Rolf Erni at EMPA.
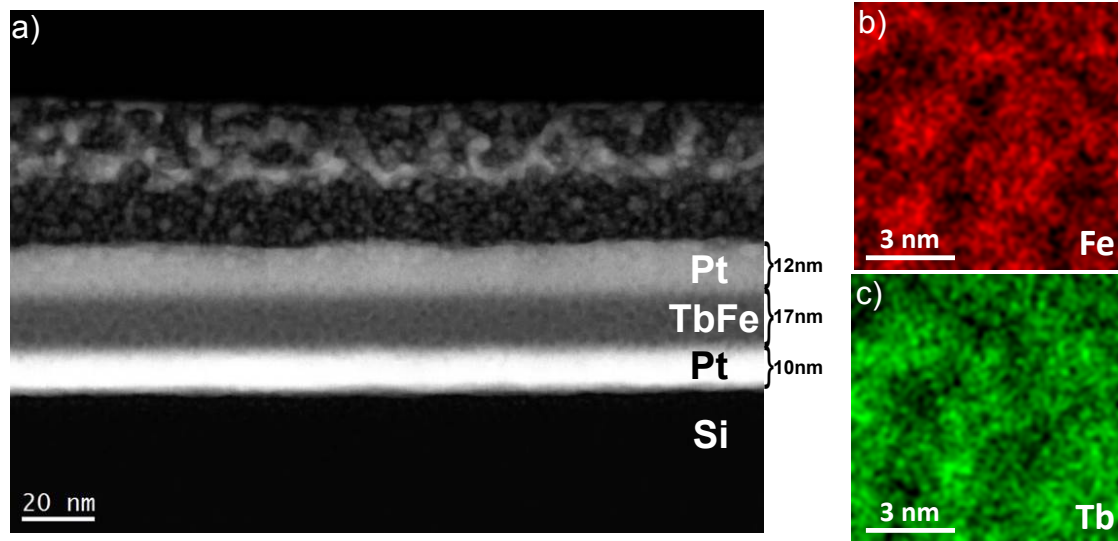
Figure 4.1: a) TEM image obtained in cross section geometry of sample *S1*. b) Local variations of Tb and Fe content measured by STEM-EDX with field of view of 9 nm×9 nm.

Figure 4.1 a) depicts the TEM image in cross section geometry of the TbFe 20 nm thin film sputtered on Si substrate with Pt adhesion layer and Pt capping

---

[1] Otto-Stern-Weg 5, 8093 Zurich, Switzerland

layer, which were labeled in the figure. The structure on top of the Pt capping is deposited by focused ion beam (FIB), as preparation for FIB cut of the TEM samples. The layer thicknesses of the Pt adhesion layer, the TbFe film and the Pt capping layer were 10 nm, 17 nm and 12 nm, respectively. The Pt adhesion layer thickness is the same as the nominal value, while the TbFe layer is thinner and the capping layer is thicker. It is apparent that the Pt cap layer is not as dense as the Pt adhesion layer, which can account for the thickness of the former. The TbFe layer thickness can not be determined accurately due to the insufficient definition of the upper and lower boundaries of the TbFe layer. This can arise from intermixing of TbFe with Pt during growth, but can also be due to the FIB preparation of the sample. Further investigations are planned to clarify the situation.

Figure 4.1 b) shows local variations of Tb and Fe content in $Tb_{25}Fe_{75}$ measured with energy dispersive X-ray analysis (EDX). The color saturation is a measure of the elemental enrichment. The maps show the complementary nature of Tb-rich and Fe-rich regions, and both elements exhibit chemically enriched areas with a characteristic length of about 3 nm. This inhomogeneous distribution of the composition of the TbFe film was not expected from an amorphous alloy. Interestingly, the inhomogeneities in TbFe film would likely contribute to domain wall pinning, leading to the high coercivity of the material, according to the extended theory of domain wall pinning by Paul [71] and the micromagnetic simulation by Suess et al. [72].

Inhomogeneities in the amorphous ferrimagnetic alloy films with RE-TM were recently also reported by other groups. Graves et al. reported in 2013 the nanoscale spin reversal in a GdFeCo system using ultrafast laser techniques [73], revealing that amorphous GdFeCo displays nanoscale chemical and magnetic inhomo-

geneities that affect the spin dynamics. Liu et al. investigated the magnetization reversal in amorphous TbFeCo thin film excited by single femto-second optical laser pulses [7]. In their sample the switched regions were randomly distributed, which was attributed to the inhomogeneous chemical nanostructure of the sample. Oezelt et al. [74] performed micromagnetic simulations of exchange coupled ferri-/ferromagnetic heterostructures, taking into account varying uniaxial anisotropic direction and anisotropic constant in the ferrimagnetic TbFe film. Hebler et al. [75] observed a thickness dependence of the TbFe magnetic properties due to growth-induced redistribution of the orientation of the Tb magnetic moments.

These findings, taken together with the preliminary STEM-EDX results, indicate that we could expect the reversal process of TbFe to be dominated by compositional inhomogeneity if the wall is of comparable width. Moreover, the coupling at the interface with a perpendicular magnetic anisotropic ferromagnet, which was lack frustration [61], might likewise be inhomogeneous, and thus strongly affect the reversal process [41, 76].

4.3 Magnetic sample characterization

4.3.1 Magnetometry data

Figure 4.2 a) shows the magnetization loop measured by VSM on the TbFe film (sample *S1*), for fields ranging from -7 T to 7 T applied perpendicular to the sample surface at 10.5 K. The sample exhibits a high coercive field of about 6 T and strong perpendicular anisotropy. This is confirmed by the domain-wall-motion leading to saturation in this field range observed by MFM (Fig. 3.7 and Fig. 4.3). In addition, a strong variation of the measured VSM signal occurs at low fields [marked in yellow in Fig. 4.2 a) and b)]. This feature was not expected for our sample which

has strong PMA and shows no domain-wall-motion even in fields up to a few Teslas. Moreover, our MFM results (Fig. 4.3) do not show any major change of the domain pattern at such low fields.
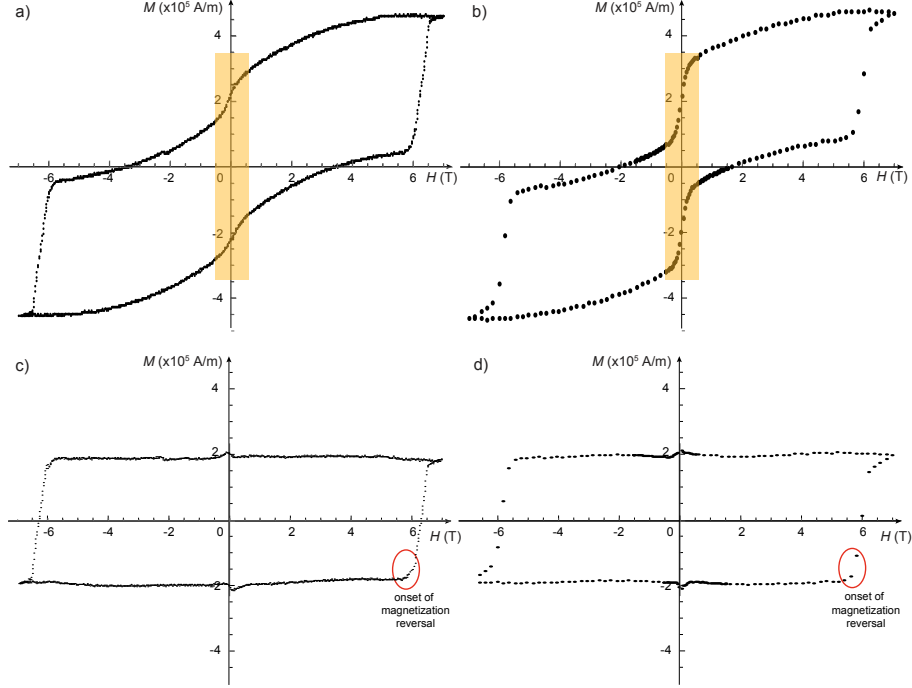
Figure 4.2: Magnetization loops of the TbFe film: measured by a) VSM and b) superconducting quantum interference device (SQUID) magnetometer, and background subtracted c) VSM loop and d) SQUID loop.

To investigate the artifacts possibly arising from a paramagnetic signal of our VSM sample holder, we had the TbFe films measured by SQUID magnetometer at the University of Augsburg. The SQUID loop depicted in Fig. 4.2 b) shows similar (even more pronounced) changes of the magnetic moment in low fields. Comparable low-field magnetic moment variations were also observed in SQUID loops performed on similar TbFe samples grown by our colleagues at the University of Augsburg, but were absent in XMCD magnetometry loops.

Furthermore, the samples were fabricated with an mask on top allowing only the

center of the substrate to be coated, which avoids the materials being sputtered on the sidewalls of the substrates. However, the masks lead to a thinner film at the boundary of the coated area due to shadowing effect. Since the magnetic properties of TbFe films depend strongly on the thickness [75], the thinner film at the boundary can contribute to the low field feature in the magnetization loops.

From this we conclude that the low field feature is an artifact, thus justifies a background subtraction using a phenomenological correction function $a \times \arctan(bH) + c$, where H is the applied magnetic field. The parameters a, b, and c are chosen to obtain a flat magnetization behavior in low and in intermediate fields. Figures 4.2 c) and d) display the background subtracted VSM and SQUID magnetometry data, respectively.

A lower bound for the magnetic anisotropy of the TbFe film 2.4×10^6 J/m^3 at 10.5 K is found from the coercive field H_c=6 T and the remanent magnetization M_R=2$\times 10^5$ A/m by $K_u^{\text{est.}}$=$2M_R H_c$. This value is consistent with the estimated lower bound for magnetic anisotropy for a ferrimagnetic $(\text{Tb}_{23}\text{Fe}_{77})_{40nm}$ film from Romer et al. [61].

In literature [1, 77], the exchange stiffness of the TbFe alloy films is set to 4×10^{-12} J/m (at room temperature). Using the Bloch wall width equation $\delta = \pi\sqrt{A^{\text{est.}}/K_u^{\text{est.}}}$ [78] and $K_u^{\text{est.}}$=2.4×10^6 J/m^3, the estimated domain wall width of the TbFe thin film is about 4 nm. It is important to note that this estimated domain wall width is comparable to the characteristic length of 3 nm of the inhomogeneities in TbFe film, as shown in the TEM data [Fig. 4.1]. If these inhomogeneities have magnetic properties sufficiently distinct from the rest of the film, strong domain wall pinning would occur, which would explain the high coercivity of the TbFe films.

4.3.2 MFM data

As the magnetometry results indicate, the TbFe thin film has a remarkably high coercivity. We are interested now in characterizing the micromagnetic state of the film, to obtain a reference for the study of the exchange-coupled double layers (ECDLs) and to improve our understanding of the mechanisms that can lead to the high coercivity.

We performed MFM measurements on the TbFe film at $10.5\,\mathrm{K}$, well below the compensation temperature T_{comp} of $385\,\mathrm{T}$ (measured by VSM). Then the Tb moment dominates that of the Fe. The low surface roughness of the samples, of about $\pm0.3\,\mathrm{nm}$ peak-to-peak measured with a Bruker ICON3 AFM, enables MFM measurements at constant average tip-sample distance of $7\,\mathrm{nm}$, and thus to obtain a high lateral resolution (see Section 2.1.2). The cantilever oscillation amplitude $(A_1)$was kept at $5\,\mathrm{nm}$ during the scan. $3\,\mathrm{\mu m}\times3\,\mathrm{\mu m}$ sized images with 256×256 pixels were acquired. We utilized silicon cantilevers with a resonance frequency of $59.676\,\mathrm{kHz}$ and nominal stiffness of $0.7\,\mathrm{N/m}$. The tip was coated with $2\,\mathrm{nm}$ of Ti followed by $6.5\,\mathrm{nm}$ Co, and a $4\,\mathrm{nm}$ Ti cap (nominal thickness).

The cantilever frequency shift changes appreciably when strong fields are applied, as shown in Fig. 3.5. The (background) frequency shift arising from the applied field was determined when the tip was retracted from the sample surface, and later subtracted from MFM data acquired in field. Thus data acquired in different external fields become comparable.

Figures 4.3 a) through o) depict the measured frequency shift Δf of sample *S1* in magnetic fields from 0 to $6000\,\mathrm{mT}$. Large micron-sized domains are observed in images taken in applied fields up tp $5000\,\mathrm{mT}$. The tip magnetization and applied magnetic field H are up (indicated by the symbol $\odot$). The up and down domains [as

marked in Fig. 4.3 a) with $\odot$ and $\otimes$, respectively] with magnetization parallel/anti-parallel to the tip magnetization exert attractive/repulsive forces on the latter, which in general results in negative/positive frequency shift contrast.

Note that domain wall contrast — not domain contrast — is observed in Fig. 4.3. The reason is that for thin film samples, especially when the tip is very close to the sample surface (which is the case for our MFM measurements, with a tip-sample distance $z=7\,\text{nm}$), the magnitude of the measured frequency shift decreases toward the center of the domain [see Section 2.1.1.2]. Therefore, the contrast in the middle of the large domains is very low (close to zero).

The domain walls remained pinned in fields up to $3\,\text{T}$ [panels b) through m)]. In isolated wall locations a motion can be observed at $4\,\text{T}$ and $5\,\text{T}$, as highlighted by the dashed circles in panels n) and o), respectively. The sample is in a saturated state in $6\,\text{T}$ [panel p)]. This is compatible with the switching field observed during MFM data acquisition in ramping fields [Figs. 3.5 a) and b)]. Further, the MFM observation agrees with the coercive fields found in the magnetometry data in Section 4.3.1.

Overall, it is remarkable how little the domain pattern changes from one field to the next between $0\,\text{mT}$ and large fields of up to $5000\,\text{mT}$. This is consistent with the large perpendicular anisotropy found in the material (also in [61]). Most domains have a size of $1\,\mu\text{m}$ or larger, but several features with a much smaller size (e.g. down to $40\,\text{nm}$) which are visible in the images in Fig. 4.3 remain stable even in fields approaching $5000\,\text{mT}$. The main change between the images appears to be a slight contrast increase, especially at the locations of the domain walls [e.g. compare the areas highlighted by dashed rectangular boxes in panels a) and l)].

In addition to the domains, small dark blue spots are visible throughout the
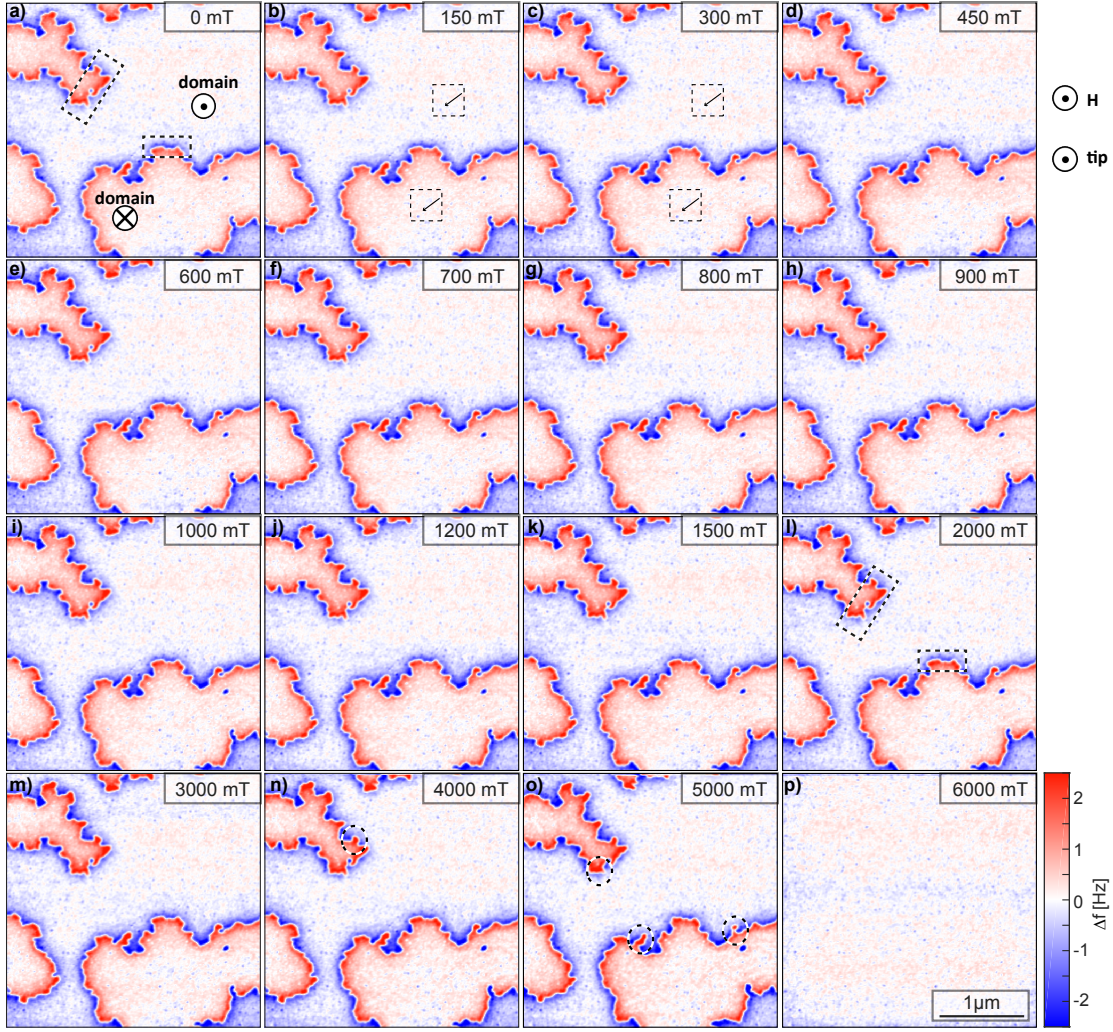
Figure 4.3: Measured frequency shift Δf of $3\,\mu\text{m}\times 3\,\mu\text{m}$ MFM-scan on the sample *S1*. The color scale of -2.5 to +2.5 Hz is the same for all the images, as given on the right edge of the figure.

image [examples are highlighted by the black arrows inside the dashed frame in Figs. 4.3 b) and c)]. They appear at the same locations for all MFM images in the series of fields, and are even visible in the saturated image. It indicates that these may not be of magnetic origin, but arise from a topography-induced spatial variation of the van der Waals force and capacitive force. Recall that the tip is scanned at a constant average height. Then small bumps will lead to a locally

smaller tip-sample distance and hence to a larger attractive van der Waals force.
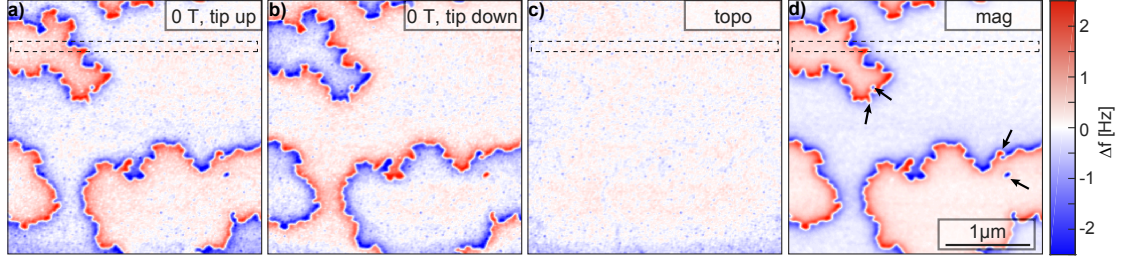
Figure 4.4: Frequency shift Δf over a $3\,\mu\text{m} \times 3\,\mu\text{m}$ area. a) and b) MFM images acquired in $0\,\text{T}$ with up and down tip magnetization, respectively. c) and d) Half-sum and half-difference of the data shown in a) and b), representing the topographic and the magnetic contribution, respectively. The images are displayed with the same color-scale of -2.5 to $+2.5\,\text{Hz}$.

As described in Chapter 3, the topographic and magnetic contributions to the measured contrast can be disentangled. This is achieved by taking the half-sum of data acquired with opposite tip polarities in zero field [Fig. 4.4 a) and b)]. The resulting data [Fig. 4.4 c)] no longer shows magnetic structures apart from a pattern of faint lines reminiscent of the domain walls. The cause for this artifact has already been discussed in Section 2.2.1 for Fig. 2.8 c). The spotty contrast visible in Fig. 4.4 c) represents the topography-induced variations of the van der Waals and capacitive contrast. To obtain the magnetic contrast, the half-difference of the data shown in Figs. 4.4 a) and b) is calculated, and displayed in Fig. 4.4 d). The small dark blue spots no longer appear, but many small features (arrows) are still visible and therefore of magnetic origin.

Apart from the topographical features, the images presented in Fig. 4.3 and Fig. 4.4 also show (very) weak contrast variations appearing from one (horizontal) scan-line to the next. See for example the lines highlighted in dashed rectangles in Fig. 4.4 a) that remain visible in Fig. 4.4 d) [and faintly also in Fig. 4.4 c)]. We found that these sudden contrast variations result from small power instabilities of

the laser used for the cantilever deflection measurement. These contrast variations can be removed from the data with a flattening procedure subtracting the average contrast of each line inside the large up domain.
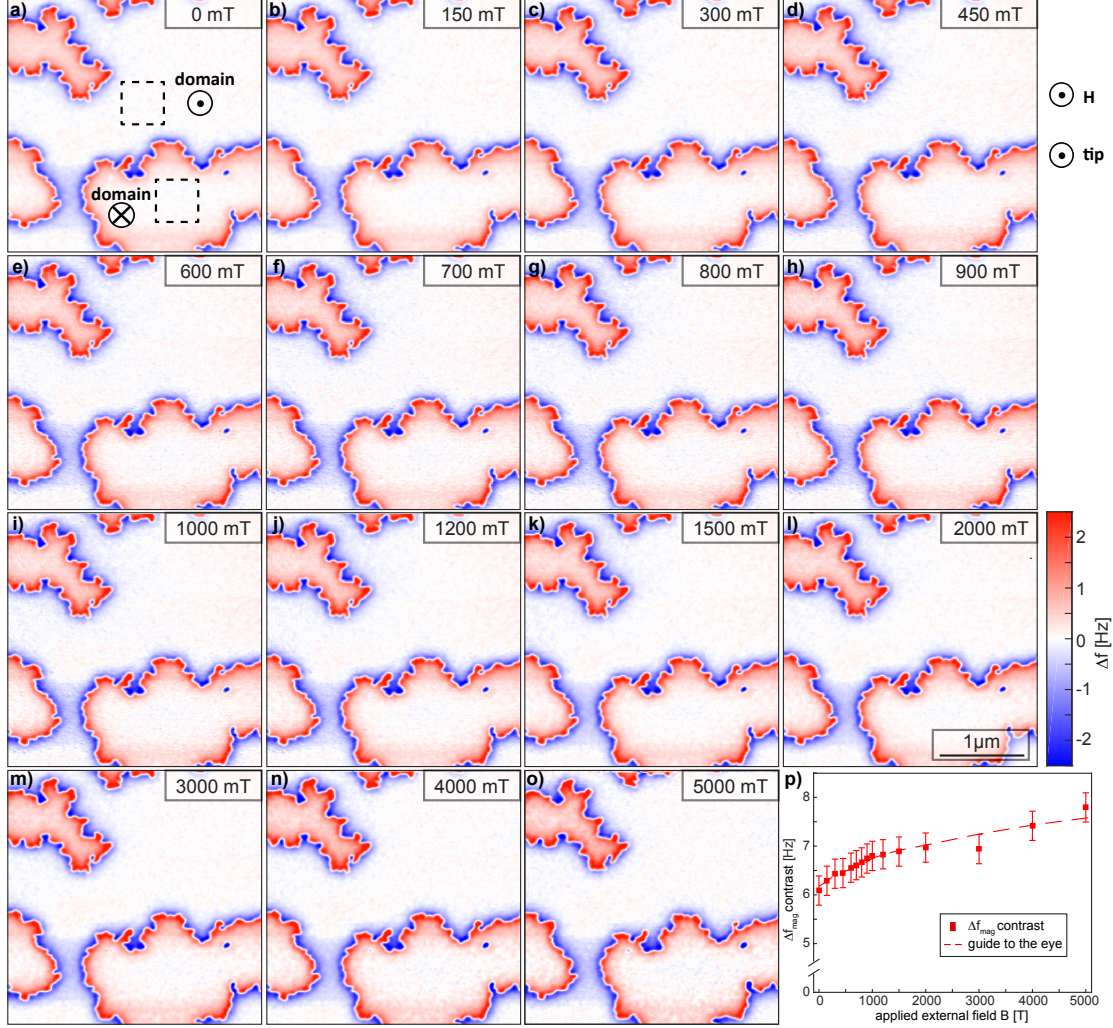
Figure 4.5: a)-o) Processed Δf_{mag} data, representing only the magnetic contrast of Fig. 4.3a)-o). p) Δf_{mag} contrast as function of applied external field for MFM-scans on sample *S1*. The squares are the calculated Δf_{mag} contrast with the error bars for the uncertainty of contrast determination, and the dashed line is a guide to the eye.

The field-dependent MFM data after the removal of the topography-induced contrast and the laser-power-instability-induced artifacts is displayed in Fig. 4.5.

Instead of the image taken in saturation in $6000\,\text{mT}$, panel p) displays the measured MFM contrast as function of the applied field, determined by the difference of the maximum and the minimum of the MFM data in Fig. 4.5 a)-o). The error bars account for the electronic control system including the bandwidth-dependent frequency-control accuracy (of about $\pm 0.1\,\text{Hz}$) of the PLL [Fig. 2.17], and the frequency shift (of about $\pm 0.2\,\text{Hz}$) due to possible small uncorrected changes of tip-sample distance during the image scans [Fig. 3.6]. The Δf_{mag} contrast increases gradually from $0\,\text{T}$ up to $5\,\text{T}$ before the applied field reaches the coercive field of the TbFe thin film.

4.3.3 Quantitative analysis of domain-level magnetic structures

There is a clear increase in the MFM contrast with applied field, displayed by Fig. 4.5 p). We propose three possible mechanisms that lead to an increase of the MFM contrast with the applied field, as illustrated in Fig. 4.6:
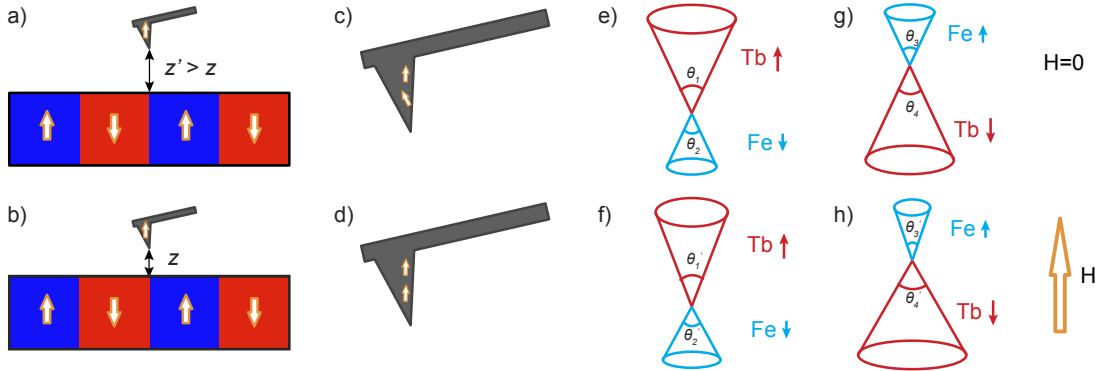
Figure 4.6: Possible mechanisms for the increase of the MFM contrast in fields, with top panels in zero field and bottom ones in applied field up. a) and b) Increase of the contrast by a decreased tip-sample distance. c) and d) The improved alignment of local magnetic moments of the tip with the field. e) and f) The closing/opening of the Tb/Fe cones in field, corresponding to the situation in the dark domains. g) and h) The opening/closing of the Tb/Fe cones in field, corresponding to the situation in the bright domains.

1. A decrease of the tip-sample distance z in applied fields would lead to a smaller *distance loss* factor e^{-kz}, resulting in a higher magnetic stray field according to Eq. 2.6 [see panels a) and b)].

   This mechanism can however be excluded, because the tip-sample distance control method described in Chapter 3 keeps the tip-sample distance constant within about ± 0.4 nm even when a field is applied (see Fig. 3.6).

2. The applied field leads to an improved alignment of the magnetic moments of the tip along the z-axis, which would lead to an increased tip-sample interaction and thus to an increased image contrast according to Eq. 2.5 [see panels c) and d)].

   This requires a separate assessment of the contrast within bright and dark domains, respectively. We discuss these results at length below (in Section 4.3.4), but refer at this point to Fig. 4.13, wherein we show that the contrast increase of the dark domains is not exactly the same as the bright domains. This means that the contrast increase (at least partially) arises from changes of the local magnetization structures of the sample and not from that of the tip, but the possibility of increased magnetic moments of the tip cannot be excluded.

3. The magnetization difference between the up and down domains of the TbFe film increases in field. The local distribution of the Tb and Fe magnetic moments, also known as sperimagnetism [79], arises from the competition between the local magnetic anisotropies and exchange interactions, and temperature fluctuations. The angular distributions (fanning cone) of the Tb and Fe moments change with applied field, and the opening and closing of the cones are direction- and element dependent [compare panels e) and f),

90

g) and h)] [75].

In this work, therefore, we attribute the Δf_{mag} contrast increase in applied field to the increase of the magnitude of the magnetization of the TbFe film.

4.3.3.1 Simulation of the domain magnetization

To quantify the magnetization dependence on the applied field, we need to associate a magnetization $M(x, y)$ with a measurement $\Delta f_{\text{mag}}(x, y)$. Looking at Eq. 2.13, it is clear that knowledge of $TF(\mathbf{k})$ allows the comparison either in terms of $M(x, y)$ or of $\Delta f_{\text{mag}}(x, y)$.

We begin with *the first approach*, and recover the magnetization pattern of the TbFe thin film magnetization $M(x, y)$ by deconvolving $TF(\mathbf{k})$ from the Δf_{mag} images.

The transfer function $TF(\mathbf{k})$ is obtained from the tip calibration procedures [Section 2.2.1]. Figure 4.7 displays a radial section through a circular averaged version of $TF(\mathbf{k})$ depicted in Fig. 2.11 c).
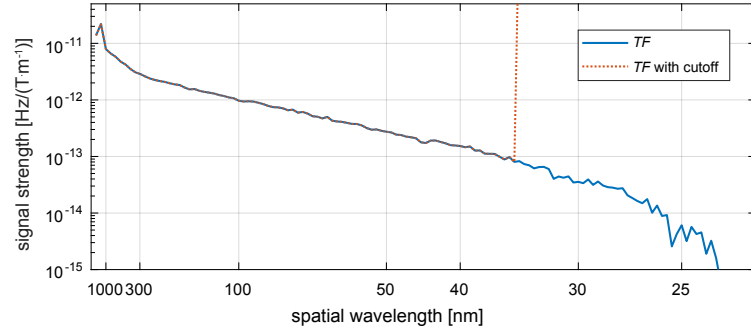
Figure 4.7: The dependence of the transfer function on spatial wavelength for Tikhonov parameter δ=16. The solid line is the original TF, and the dashed line is the TF with cutoff frequency k_{limit}, where $1/k_{\text{limit}} = 33\,nm$.

The magnetization pattern obtained from the deconvolution of the Δf-pattern is displayed in Fig. 4.8 b). This pattern can be compared with a pattern of through-

thickness domains (and domain wall width of 4 nm) in Fig. 4.8 a), which is obtained by multiplying the domain pattern of Fig. 4.5 a) with the sample remanent magnetization of 2×10^5 A/m [from Fig. 4.2].
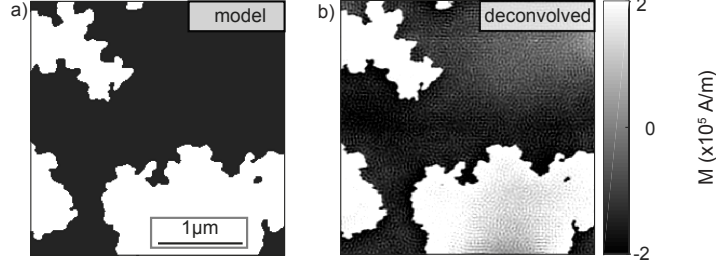
Figure 4.8: Magnetization pattern M for TbFe film in zero field, displayed with the scale of -2×10^5 to 2×10^5 A/m. a) Model magnetization pattern. b) Deconvolved M in zero field.

Some structures can be seen inside the domains of the deconvolved M [Fig. 4.8 b)]. This can be attributed to the low signal strength of $\Delta f_{1,\mathrm{mag}}$ in the middle of big domains of the TbFe film, and the fact that the deconvolution contains inverse distance loss factors from the propagation from the sample surface to the scan plane. These are exponential amplifications for the short wavelengths in the magnetic structure [Eq. 2.13]. For the same reason, the transfer function with a cutoff wavelength of λ_{limit} =33 nm [dotted line in Fig. 4.7] is used in the deconvolution to avoid amplifying the high frequency noise of $TF(\mathbf{k})$ which would give rise to artifacts in the deconvolved M. However, the deconvolved M [Fig. 4.8 b)] still contains some artifacts. We conclude that this approach is not precise enough to distinguish the putative magnetization amplitude variations with applied field.

The second approach utilizes a magnetization pattern [Fig. 4.8 a)] obtained from the MFM data with a magnetization tuned to match the simulated Δf-contrast to the measured one. Note that in this case the propagation from sample surface to scan plane is an exponential loss factor, that attenuates the noise of

$TF(\mathbf{k})$ at small spatial wavelengths.

For the TbFe thin film (sample *S1*), the simulated frequency shift image in zero field using the model magnetization pattern [Fig. 4.8 a)] is depicted in Fig. 4.9, as an example. A detailed procedure of the simulation using the transfer function is discussed in Section 2.2.2.
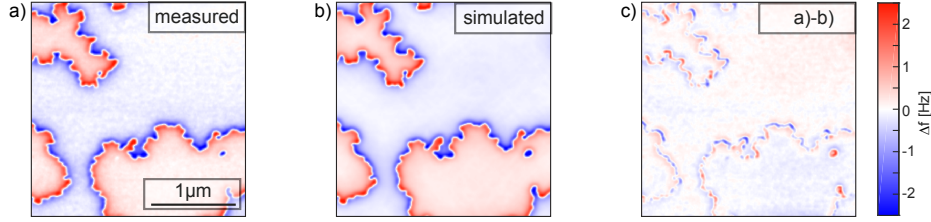
Figure 4.9: a) Measured magnetic contrast [same as Fig. 4.5 a)]. b) Simulated frequency shift. c) Difference of a) and b).

The contrast of the simulated MFM-image [Fig. 4.9 b)] matches that of the measured image [Fig. 4.9 a)] well. Small (positive and negative) deviations at the walls can be attributed to Bloch lines in the walls, a slightly wrong position of the domain wall in the estimated magnetization pattern, or a local variation of the domain wall thickness that is not included in the model magnetization pattern. The same is true for the granular magnetic contrast visible in the measured image, which may arise from local variations of the saturation magnetization or its alignment along the z-axis, which is again not included in our model magnetization pattern.

Simulations of the stray field of a given magnetization *pattern* will need to account for a field-dependent magnetization *amplitude* to be able to give rise to the anticipated contrast change. We therefore want to find an expression for the field dependent effective magnetization amplitude. For a more robust measurement of the evolution of the magnetization amplitude, we compute the amplification

factor which best reproduces the observed contrast amplitude. The dependence of the amplification factor on the applied field (equivalent to the dependence of the normalized magnetization amplitude) is plotted in Fig. 4.10. As a comparison, the normalized MFM contrast (the difference of the maximal and minimal frequency shift over all the pixels of the image) as function of field [Fig. 4.5 p)] is also plotted in this figure. Both the magnetization amplitude [red circles in Fig. 4.10] and the Δf_{mag} contrast [black squares in Fig. 4.10] increase with applied field. The increase of the magnetization amplitude is smoother than the MFM contrast, suggesting that the simulation of the MFM data gives a better estimate of the magnetization. The small but existing mismatch of the determined domain patterns with the MFM images [compare Fig. 4.8 a) and b)] can lead to a slightly attenuated magnetization amplitudes.
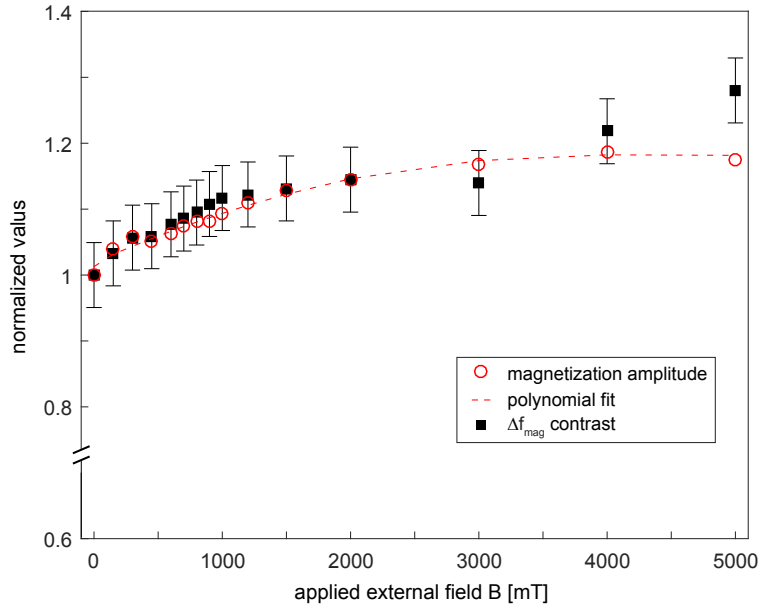
Figure 4.10: Normalized magnetization amplitude (red circles) which best reproduces the observed contrast amplitude and the normalized Δf_{mag} contrast (black squares) as function of the applied field. The magnetization amplitude and Δf_{mag} contrast are normalized with respect to the one in zero field.

The increase of the Δf_{mag} contrast and of the magnetization amplitude in applied fields has been addressed in this section. The observed increasing contrast with applied fields in the MFM images [Fig. 4.5] is considered to arise from the increase of the TbFe film magnetization. On the other hand, an increase of tip magnetization can also give rise to the increasing contrast in the MFM images.

The above example shows that with the transfer function obtained by calibrating the tip [Section 2.2.1], it is possible to reliably calculate the TbFe layer that gives rise to the observed frequency shift. This is significant because we can count on this ability to infer the existence of ferrimagnetic domain patterns also in situations where the ferrimagnet is part of an exchange couple double-layer structure. The 4th order polynomial fit is used for the simulations in Section 5.4.2.2.

4.3.4   Analysis of the MFM contrast within the domains

Note that the 'rough contrast' visible in the (high field) images inside the magnetic domains [Fig. 4.5] is of magnetic origin. It could arise from a thickness variation of the magnetic layer [discussed in Section 2.2.1], or from local variations of the magnetic moment density that may be related tp an inhomogeneous distribution of the composition and hence magnetic properties of the TbFe film [Secion 4.2]. For clarity, we will refer to these contrast structures "magnetic background."

A distinction between the evolution of the magnetization in opposite applied field directions could not be discerned looking at domain stray fields, as in the previous sections. We need to investigate the magnetic background over a small area of $500\,\mathrm{nm}{\times}500\,\mathrm{nm}$ cropped inside the large down and up domains of the topography-subtracted images, as marked by the dashed squares in Fig. 4.5 a). The square size was chosen so as to be unaffected by the domain wall contrast at

that location, as can be seen from simulations analogous to Section 4.3.3.1 (not shown). The nano-structures can be better seen when displayed in a different color scale spanning the range from -0.2 to 0.2 Hz.
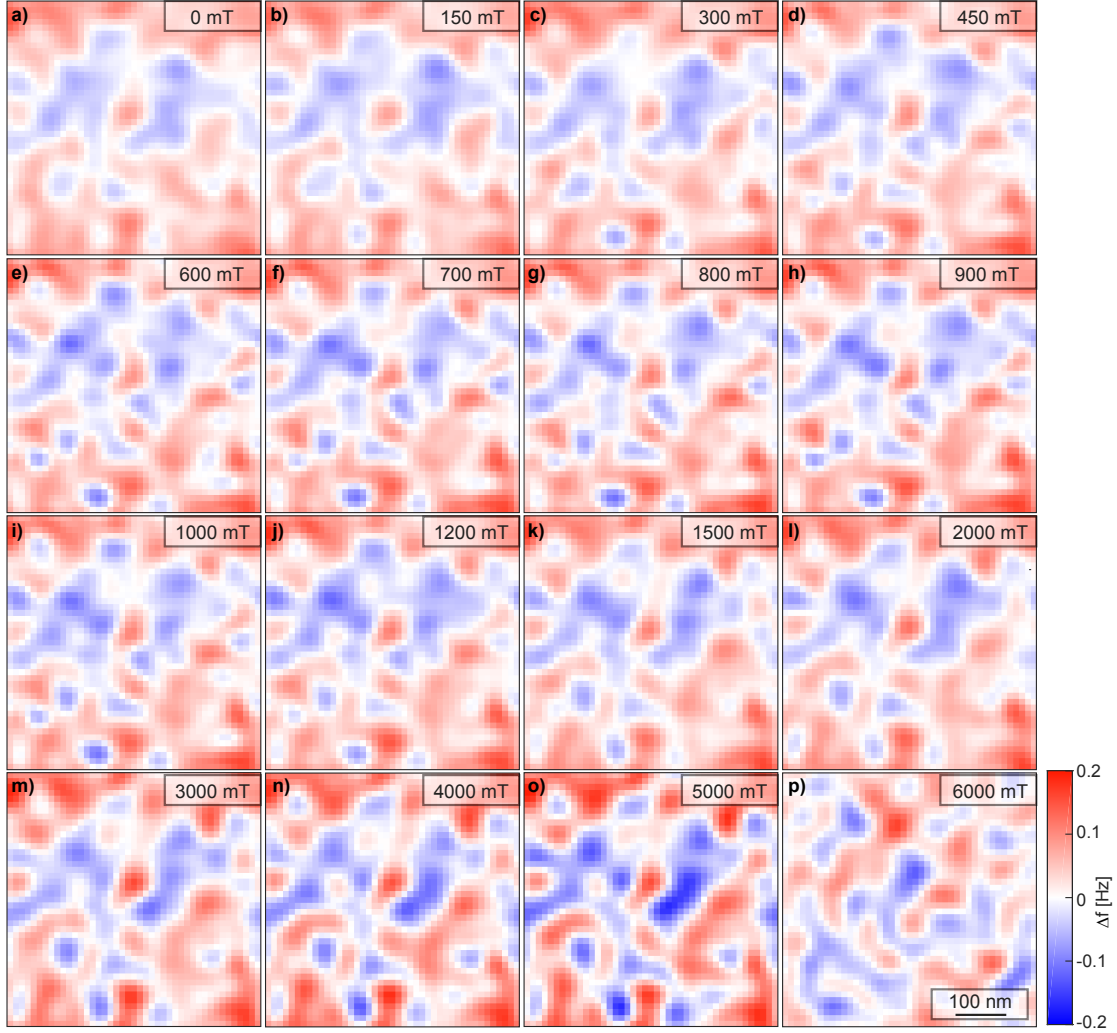
Figure 4.11: Zoomed-in images over a 500nm×500nm area inside the down domain (⊗ domain), as marked by the dashed square in Fig. 4.5 a). The applied external magnetic fields in T for each column are given in the upper right corner of each image. Note that the color scale given on the bottom right of the figure is between -0.2 and 0.2 Hz, which covers much smaller range than for the 3000nm×3000nm images in Fig. 4.5.

Figures 4.11 and 4.12 show the evolution of the magnetic contrast with the applied field inside the down and up domain, respectively. The dependence of the
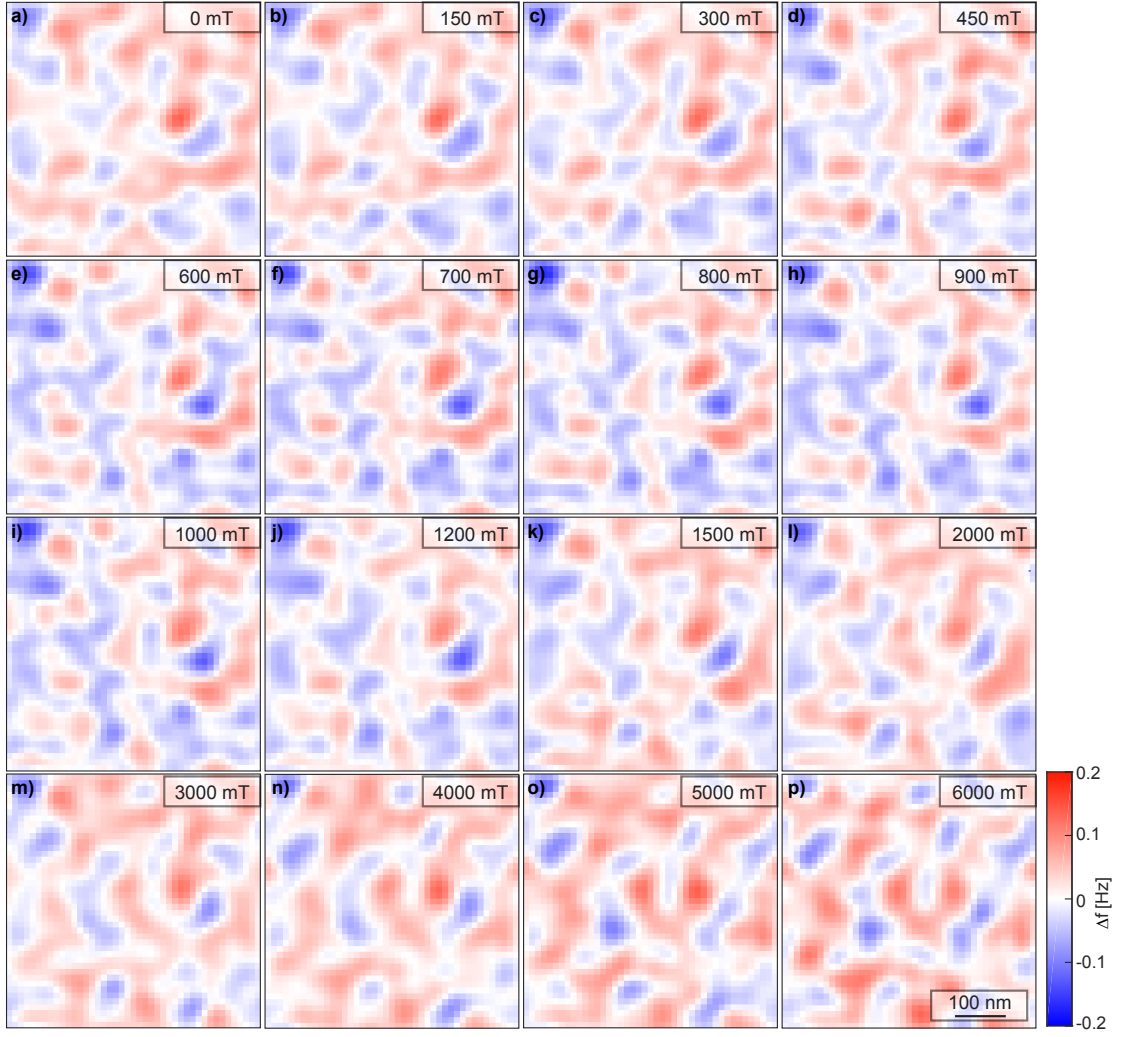
Figure 4.12: Zoomed-in images over a 500nm×500nm area inside the up domain (⊙ domain), as marked by the dashed square in Fig. 4.5 a). The applied external magnetic fields in T for each column are given in the upper right corner of each image. Note that the color scale given on the bottom right of the figure is between -0.2 and 0.2 Hz, which is much smaller than the 3000nm×3000nm images shown in Fig. 4.5.

Δf-contrast ($\Delta f_{\max} - \Delta f_{\min}$) on the field is plotted in Fig. 4.13 a) for both domains. Surprisingly, the contrast inside the down domain increases while that inside the up domain remains constant, but changes of the local structure are smaller in the down domain. The latter was assessed by cross-correlating the images obtained in applied fields with the zero field image [Fig. 4.12 a)] or 5 T image [Fig. 4.12 o)],

respectively.
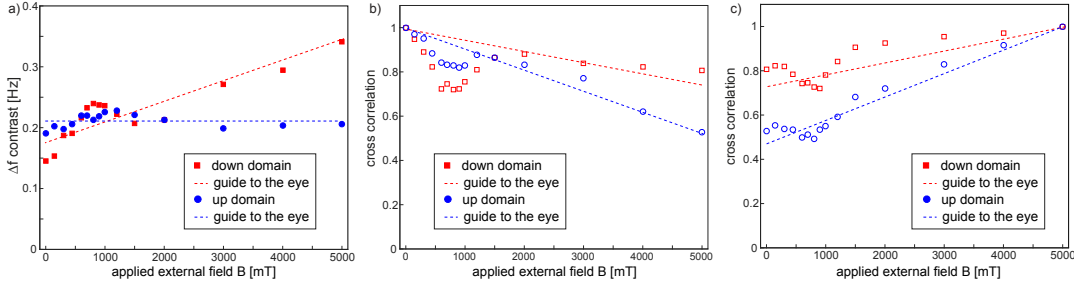
Figure 4.13: a) Δf_{mag} contrast and b) cross-correlation with respect to the 0 T image and c) cross-correlation with respect to the 5 T image as function of applied field for the cropped images over a 500nm×500nm area inside the up and down domains, from Fig. 4.11 and Fig. 4.12, respectively.

The following conclusions can be drawn from the above observations:

1. Because the contrast in the down domain increases whereas that of the up domain remains constant, the increase of the contrast of the MFM images of the down and up domains (Figs. 4.11 and 4.12, respectively) does not arise from an improved alignment of the magnetic moments of the tip along the z-axis. Hence, the increase of the contrast of the MFM images of the domain pattern (Fig. 4.5) with applied field arises from an increased difference of magnetic moments of the up and down domains. It is further evident that this increase of the magnetic moment difference cannot be caused by a field-driven alignment of the down domain moments along the negative z-axis, but must arise from an improved alignment of the moments of the up domains. The increase of the up magnetic moment arising from a closing of the ferrimagnetic cone of the Tb moments must be stronger than that arising from the opening of the cone in the down domains, such that a net increase of the magnetic moment difference between the up and down domains and hence an increase of the observed MFM contrast is obtained.

2. Such an increase of the magnetic moment of the up domain is compatible with the observation that the contrast within the up domain does *not* increase, for example when the magnetization of the up domain increases homogeneously. In the latter case one would however not expect that the cross-correlation decays with with increasing fields. This indicates that the sub-domain pattern and hence the local magnetic moment density changes with the field. Such a change of the local magnetic moment density may arise from locally softer parts of the sample that may be attributed to local compositional variations.

3. The observed changes of the local MFM contrast in increased fields however remains small, i.e. much smaller than the contrast variations observed for the exchange coupled double layer (ECDL) system discussed in Chapter 5.

5 Reversal mechanisms in a [Co/Pt]$_{\times 5}$-multilayer with strong interfacial exchange-coupling to a ferrimagnetic TbFe thin film

In the previous chapter, the structural and magnetic properties of amorphous Tb$_{25}$Fe$_{75}$ layers were discussed. In this chapter we build on those results and investigate the reversal of exchange-coupled double layers (ECDLs), in which the RE-TM ferrimagnetic TbFe film and a TM/noble metal (NM) [Co/Pt]$_{\times 5}$-multilayer are coupled with varying strengths.

5.1 General introduction

Exchange-coupling in double layers based on RE-TM/TM/NM shares some of the characteristics of the coupling in AF/ferromagnet (F) systems, the prototypical exchange-bias systems. In this introduction we discuss some aspects of exchange-bias systems and ferrimagnet (Fi)/F systems that are relevant to the understanding of our TbFe-based ECDLs. Also, we address the concept of interfacial domain walls (iDW) [80], which plays an important role in the reversal of strongly coupled ECDLs like the present one, as we will show. Finally we discuss the existing research on the use of spacing layers between coupled layers to modify the coupling.

5.1.1 Exchange-bias effect and exchange-coupled systems

The exchange-bias effect typically arises in a ferromagnetic layer adjacent to an antiferromagnetic layer. It is a consequence of anchoring the magnetic moments of the former in the latter. The AF constitutes a good anchor point a priori, on account of its vanishing macroscopic magnetization and typically large magne-

tocrystalline anisotropy. However, the net coupling between the AF and the F is much weaker than what inter-atomic coupling might lead to think. Several models have been applied to different systems to help understand why this is the case, and a review of exchange-bias and these effects was presented by Nogues et al. in 1998 [81].

Using quantitative MFM, Schmid et al. [76] have shown that the coupling between AF and F in their system is proportional to the density of pinned uncompensated spins (pUCS) that are aligned antiparallel to the F magnetic moments, and imaged the spatial distribution of these pUCS. In a following work, Benassi et al. [82] used a 2D phase field model that incorporated the measured pUCS pattern of Schmid et al. [76], and reproduced the macroscopic loops as well as the domain patterns at all measured field levels, in a process shown to be of lateral wall motion. Their work confirmed that the exchange-bias field is proportional to the spatially averaged density of pUCS, and that the increased coercivity is an important extented result of the amplitude of the local pUCS areal density variation. This means that the inhomogeneity of the stray field of the AF and the interfacial coupling are related. We will discuss this concept further along this chapter. Note that previous explanations attributed the increased coercivity to the density of the uncompensated spins of the AF rotating with those of the F.

Unlike the AF in conventional exchange-bias systems using a AF/F bilayer, the moments of the Fi in our ECDLs are made of different elements. The coupling between RE and TM atoms is antiferromagnetic, but among TM atoms such as Co and Fe it is ferromagnetic. Therefore, the Fi/F coupling is overall antiferromagnetic if the RE moments dominate over the TM moments, and is conversely ferromagnetic if the TM moments dominate.

Concerning ECDLs based on TbFe, Aeschlimann et al., in their pioneering work in 1988 [83], used spin-polarized photoemission to study the exchange-coupling of Fe grown on amorphous TbFe ferrimagnets (a-TbFe), showing that interesting magnetic properties (perpendicular anisotropy, coercivity) of a-TbFe may be imposed onto Fe which lacks these properties.

First studies on exchange-coupled RE-Fi films were devoted to a GdFe/TbFe/GdFe trilayer fabricated by thermal evaporation by Mangin et al. in 1998 [84], where the GdFe layers were the soft Fis with in-plane anisotropy and the TbFe layer was the hard Fi with PMA. Further, a weak exchange-bias effect was reported for this trilayer system [85], as well as for in-plane anisotropy bilayers of the form FeSn/FeGd and FeGd/TbFe [86]. The first bilayer couples antiferromagnetically leading to a positive exchange-bias field (H_{ex}), while the latter couples ferromagnetically, generating a negative H_{ex}.

The previous work in our group has studied the temperature dependence of the large exchange-bias in TbFe-Co/Pt system [61], presenting hysteresis loops of the TbFe film and TbFe-Co/Pt coupled system (obtained with VSM).

5.1.2 Interfacial domain walls (iDWs) and magnetization reversal

Domain walls in thin films typically separate through-thickness domains, i.e. the domain wall is crossed along a line in the plane of the film. Its lateral motion in the plane of the film causes the relative domain fraction to change, resulting in net macroscopic magnetization change. This is the process by which (weakly coupled) exchange-bias systems revert in the aforementioned work [76], [82]. In contrast, an interfacial domain wall (iDW) separates two domains on either side

of the film, extending parallel to it, so that crossing it requires traversing a line running perpendicular to the film. This configuration tends to carry a larger energy per unit area than a through-thickness domain wall on account of the magnetic chargees it creates inside the film.

Early work on the magnetization and iDW of exchange-coupled bilayers dates back to 1987 and is due to Mauri et al. [87] and Malozemoff et al. [88]. The nucleation, propagation and compression of iDW were discussed in 1998 by Mangin et al. [84]. Mangin et al. [89] studied in 2004 the magnetization reversal process of the in-plane magnetized GdFe/TbFe ferrimagnetic bilayer by XMCD, which allowed the separation of the magnetic contribution of Gd, Tb, and Fe at the system interface, and gave evidence of the creation of the iDW and its compression and pinning. The mechanism of reversal in these bilayers was identified in 2008 [90] as occurring through iDW nucleation and lateral domain wall propagation.

There have also been indications that iDWs are found in Tb-Fe based Fis. C.-C. Lin et al. [91] reported bilayers of TbFeCo exhibiting PMA with different compositions in 2003. A giant exchange-coupling energy of $5\,\mathrm{mJ/m^2}$ and a large exchange-bias of $3\,\mathrm{kOe}$ were found at room temperature. In their later work, XMCD spectroscopy was used to study the transition from perpendicular to in-plane magnetization in Co films grown on TbFeCo, by increasing Co film thickness [92]. For a Co film thickness of $1.5\,\mathrm{nm}$, the Co moment was oriented perpendicular to the surface, because of the strong coupling to the TbFe layer. At larger thicknesses, i.e. $5\,\mathrm{nm}$, the Co moments were found to be in-plane. The TbFe moments located at the interface follow the Co moments (in-plane) and become perpendicular further away from the interface. It was hence concluded that a partial in-plane domain wall had formed inside the TbFe layer.

A more complete analysis of the iDW formation in exchange-spring films exhibiting PMA was performed by Watson et al. [80]. They grew a TbFeCo(24.5 nm)/ [Co(0.35 nm)/Pd(t_Pd)]$_{\times 15}$/Pd(2nm) multilayer with t_Pd = 0.5 and 0.7 nm on Si-wafers by DC-magnetron sputtering at room temperature. These samples were analyzed as a function of the applied field by polarized neutron reflectometry measurements. A depth-dependent in-plane magnetic moment was fitted to the measured data and compared to a 1D-spin chain model. The results revealed that iDW mainly located inside the [Co/Pd] multilayer with a domain width of 4.5 nm for t_Pd = 0.5 nm and 1.5 nm for t_Pd = 0.7 nm. The latter iDW is said to be thinner because of the smaller exchange-coupling across the Pd layers. With increasing fields a decrease of the maximum in-plane magnetic moment and a compression of the iDW to the interface was found. Considerably larger in-plane moments but smaller wall width were found in 1d-spin chain model calculations. Watson et al. attributed this discrepancy to a spatially inhomogeneous iDW that may have a width that varies with the position in the plane. But these studies were unable to resolve any lateral variation in the wall characteristics. As we report in the following sections, the results from our high resolution MFM studies call for modifying our understanding of the reversal process in these types of materials.

5.1.3 Influence of spacing layer on exchange-coupling

Driven by the implications for applications in high density magnetic recording [93] [94], the use of non-magnetic spacers to separate two thin magnetic layers with PMA has been investigated to an extent. Garcia et al. studied the role of a Pt spacer in the F/AF exchange-coupled system $(\mathrm{Pt/Co})_n$ /FeMn. They observed an enhancement of the exchange-bias field H_ex for a Pt interlayer of a few angstroms

and decrease of H_{ex} for thicker Pt layer [95]. Schuermann et al. [96] studied the influence of Pt interlayer thickness on the exchange-coupling between a CoPtO hard layer and a CoCrPt soft layer, observing that the layers switch as a single unit with thin Pt interlayers ($<$1.6 nm) and reverse separately with a thicker Pt interlayer. Berger et al. [97] demonstrated that an optimized nonmagnetic coupling layer thickness improves the media writeability and recording performance due to improved media noise properties. Radu et al. reported an adjustable perpendicular exchange-bias in ferrimagnetic spin valves by means of thickness variation of the interlayer spacer Ta between $DyCo_5$ and $/Fe_{76}Gd_{24}$ [98]. Tang et al. [99] studied the magnetization reversal in $[Co/Ni]_n/TbCo(2nm)$, and achieved high H_{ex} by tuning the Co interlayer thickness.

It can be seen from the previous studies that the exchange-coupling can be tuned by adjusting the interlayer thickness. Here we study $TbFe/[Co/Pt]_{\times 5}$ ECDLs, and in particular their reversal mechanism. We further investigate the influence of Pt spacing layers on the coupling strength and the evolution of the micromagnetic structure on a scale down to 20 nm.

5.2   Sample fabrication and composition

A series of $Si_{\mathrm{ox}}/Pt_{10nm}/TbFe_{20nm}/Pt_{d_{\mathrm{int}}}/[Co_{0.4nm}/Pt_{0.7nm}]_{\times 5}/Pt_{3nm}$ samples with Pt interlayer thickness $d_{\mathrm{int}} = 0$, 0.4 nm, 0.7 nm, 1.2 nm, 2.0 nm, and 2.5 nm were fabricated by DC magnetron sputtering in an UHV AJA Orion sputtering system (see Table 5.1). For the amorphous TbFe ferrimagnetic bottom layer, the same sputter conditions as those described in Section 4.2 were used. The deposition rates of Co and Pt were 0.09 Å/s and 0.24 Å/s, respectively, for the $[Co/Pt]_{\times 5}$-multilayer and the Pt layers.

S1	$\mathrm{Si_{ox}/Pt_{10nm}/TbFe_{20nm}/Pt_{8.5nm}}$
S2	$\mathrm{Si_{ox}/Pt_{10nm}/TbFe_{20nm}/[Co_{0.4nm}/Pt_{0.7nm}]_{\times 5}/Pt_{3nm}}$
S3	$\mathrm{Si_{ox}/Pt_{10nm}/TbFe_{20nm}/Pt_{0.4nm}/[Co_{0.4nm}/Pt_{0.7nm}]_{\times 5}/Pt_{3nm}}$
S4	$\mathrm{Si_{ox}/Pt_{10nm}/TbFe_{20nm}/Pt_{0.7nm}/[Co_{0.4nm}/Pt_{0.7nm}]_{\times 5}/Pt_{3nm}}$
S5	$\mathrm{Si_{ox}/Pt_{10nm}/TbFe_{20nm}/Pt_{1.2nm}/[Co_{0.4nm}/Pt_{0.7nm}]_{\times 5}/Pt_{3nm}}$
S6	$\mathrm{Si_{ox}/Pt_{10nm}/TbFe_{20nm}/Pt_{2.0nm}/[Co_{0.4nm}/Pt_{0.7nm}]_{\times 5}/Pt_{3nm}}$
S7	$\mathrm{Si_{ox}/Pt_{10nm}/TbFe_{20nm}/Pt_{2.5nm}/[Co_{0.4nm}/Pt_{0.7nm}]_{\times 5}/Pt_{3nm}}$

Table 5.1: Summary of ECDLs structures analyzed in this work.

The layer structures are illustrated in Fig. 5.1, e.g. for the sample *S1*, $\mathrm{TbFe/[Co/Pt]_{\times 5}}$ (*S2*), and $\mathrm{TbFe/Pt_{0.7nm}/[Co/Pt]_{\times 5}}$ (*S4*). The overall composition of the TbFe bottom layer of sample S2 was determined by RBS[1]. The measured atomic ratio of 26.5±1.5 % Tb and 73.5±1.5 % Fe, i.e. the same as the TbFe film of sample *S1*. In both cases the nominal and actual compositions are very similar.
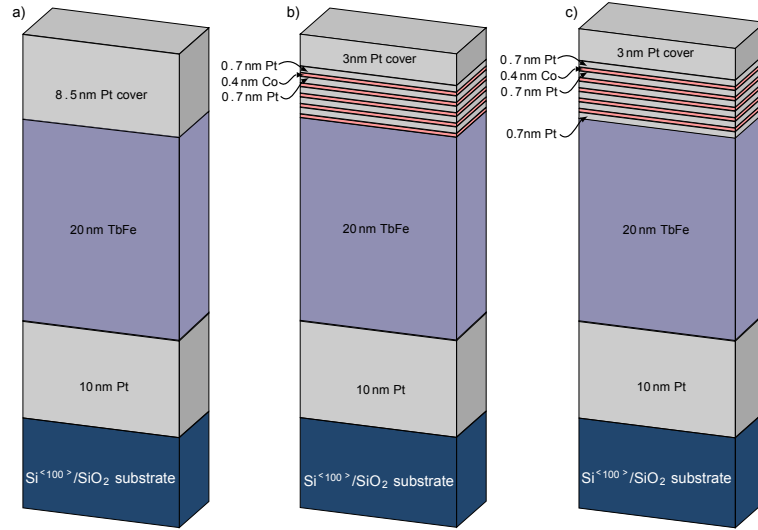
Figure 5.1: a), b) and c) The layer structure of the samples *S1*, *S2*, and *S4*, respectively.

Note that the samples *S1* and *S2* (Fig. 5.1) were designed such that the distance between the top surface of the sample and TbFe layer is the same for both samples, by adjusting the Pt capping layer thicknesses.

---

[1] Max Doebeli, ETH Zurich, Otto-Stern-Weg 5, 8093 Zurich, Switzerland

5.3 Macroscopic magnetic sample characterization

5.3.1 Magnetometry data

Figure 5.2 shows the areal density of the magnetic moment measured by VSM magnetometry on samples $S2$, $S4$, and $S7$, i.e. $TbFe_{20nm}/Pt_{d_{int}}/[Co_{0.4nm}/Pt_{0.7nm}]_{\times 5}$ with $d_{int} = 0$, 0.7, and 2.5 nm, for applied perpendicular fields sweeping from 7 T to -7 T then back to 7 T at 10.5 K. Background due to the measurement was removed from the loop in a similar way as used in Section 4.3.1.
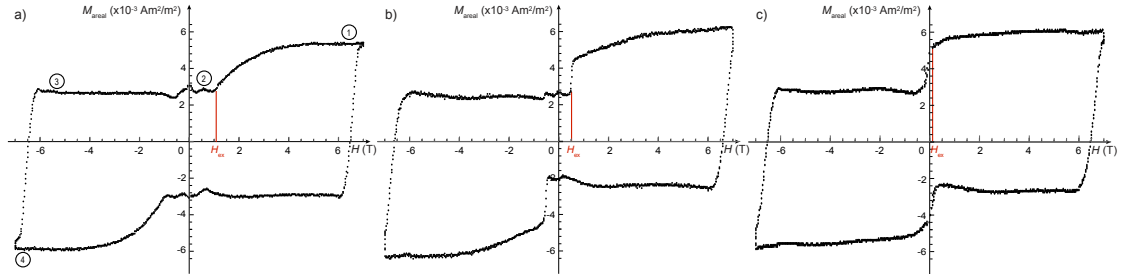
Figure 5.2: Areal density of the magnetic moment for samples a) $S2$, b) $S4$, and c) $TbFe/Pt_{2.5nm}/[Co/Pt]_{\times 5}$ ($S7$) measured by VSM. The observed exchange-bias field (marked by the vertical red line) is about 1.1 T, 0.7 T and 0 T, respectively.

For sample $S2$ [Fig. 5.2 a)], it is saturated in +7 T. A magnetization switching process occurs around -6 T upon decreasing the applied field from +7 T to 0 T and increasing the field in the opposite direction. This process consists of domain wall nucleation and lateral motion in the TbFe film, as can be seen in Figure 3.7 a) - b), and also in Section 4.3.2]. In addition, a gradual decrease of the magnetization occurs between about 5 T and 1.1 T, which is significantly smaller than the coercive field of TbFe. This is the magnetization reversal from the [Co/Pt]-multilayer. The vertical red line in Fig. 5.2 a) marks the exchange-bias field H_{ex}, determined as the onset of the magnetization reversal of the [Co/Pt]-multilayer. The measured magnetic moment areal density stays the same as the applied field decreases to

0 T, and switches its direction then increases. The reversal of the TbFe film occurs between -6 T (state 3) and -7 T (state 3). The difference of the magnetic moment areal density between these two states is about $8.8 \times 10^{-3} \, \mathrm{Am^2/m^2}$, resulting in a magnetization (magnetic moment volume density) of $4 \times 10^5 \, \mathrm{A/m}$ for a 20 nm thick TbFe film. This magnetization is twice the remanent magnetization of the TbFe film of sample *S1* [Fig. 4.2], as expected. The difference of the magnetic moment areal density between states 1 and 2, i.e. the reversal of the [Co/Pt]-multilayer, is about $3 \times 10^{-3} \, \mathrm{Am^2/m^2}$, lower than $8.8 \times 10^{-3} \, \mathrm{Am^2/m^2}$ of the TbFe film. Therefore the magnetic moment of the TbFe film is dominating that of the [Co/Pt]-multilayer.

For sample *S4* [Fig. 5.2 b)], which comprises a 0.7 nm thick Pt interlayer, similar magnetization switching processes of the TbFe film and the [Co/Pt]-multilayer are observed, with a reduced exchange-bias field at about 0.5 T. Also in sample *S7* (comprising a 2.5 nm thick Pt interlayer) [Fig. 5.2 c)], the TbFe film switches at around 6 T, but the [Co/Pt]-multilayer switches in very low fields, below 0.1 T.

5.3.2 Significance of the magnetometry data

Figure 5.3 is a simplified model to illustrate the general orientation of the moments of the double layers of sample *S2* in various fields. The states 1 to 2, and 3 to 4, illustrate the magnetization reversal of the [Co/Pt]-multilayer and the TbFe film, respectively. In low fields (state 2 in Fig. 5.3) the [Co/Pt]-multilayer is exchange-coupled antiparallel to the TbFe film (the Fe-Co coupling is ferromagnetic and the Tb-Co coupling is antiferromagnetic; further, at 10.5 K the Tb moment dominates the others), while in (sufficiently) high fields (above 6 T) (states 1 and 4 in Fig. 5.3) both layers are aligned parallel to the field. In high fields the exchange-coupling

is broken, and we expect an iDW to form [89, 91, 80] (marked by the green areas in states 1 and 4 in Fig. 5.3) at the interface of the TbFe film and the [Co/Pt]-multilayer.
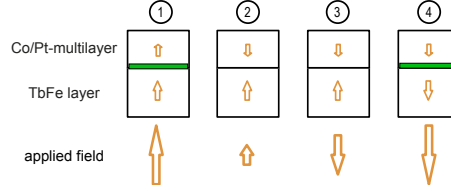
Figure 5.3: Cartoons illustrate the [Co/Pt]-multilayer and the TbFe moments in various fields for sample *S2*, where the states 1-4 are marked in Fig. 5.2 a).

According to Mangin et al. [89] and Watson et al. [80], the iDW is compressed with increasing field. Besides this view, the observed slight increase of magnetic moment from about 4 T towards 7 T in Fig. 5.2 a) could be attributed to the compression of the iDW.

From the magnetometry data of samples *S2* to *S7*, the exchange-bias field H_{ex} decreases from 1.1 T to lower than 0.1 T as Pt interlayer thickness increases from 0 to 2.5 nm. As expected, the exchange-coupling between the TbFe film and the [Co/Pt]-multilayer is weakened by the Pt interlayer, but the decoupling is not immediate once the Pt-interlayer thickness exceeds one atomic monolayer, about 0.196 nm.

The decrease of exchange-bias field with increasing Pt interlayer thickness is plotted in Fig. 5.4. The error bars of ±50mT in Figure 5.4 represent the uncertainty in determining the exchange-bias field [e.g. Fig. 5.2 a)].

The temperature dependent exchange-coupling between a $[Co/Pt]_{\times 5}$ ferromagnetic layer and an armorphous TbFe layer with strong PMA and a high coercivity was studied by VSM magnetometry [61]. It had been found that the strength of the exchange-coupling increased very rapidly and saturated as the tempera-
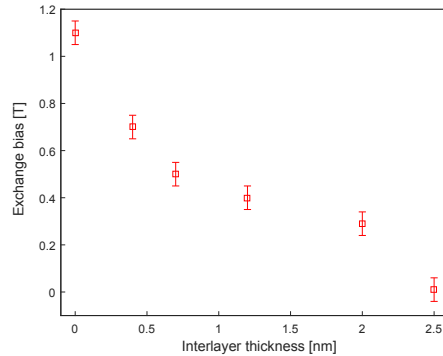
Figure 5.4: Exchange-bias field [T] as a function of Pt interlayer thickness [nm].

ture decreased below the compensation point, unlike the exchange in conventional exchange-bias systems. This was evidence of the absence of frustration in the RE-TM-based Fi/F interface.

Note that the microscopic details of the TbFe reversal in these ECDLs could be influenced by the strong coupling to the [Co/Pt]-multilayer, whereas the macroscopic characteristics of the reversal is reminiscent of the reversal of typical PMA thin films (via lateral domain-wall-motion). Moreover, the magnetization reversal of the [Co/Pt]-multilayer apparent in the hysteresis loops [Fig. 5.2] bears little resemblance to that of stand-alone films. It is necessary to characterize these reversal processes microscopically, in particular in the fields around the exchange-bias field.

5.4   Microscopic magnetic sample characterization

To characterize the reversal process microscopically, MFM was used to measure the local stray field of the ECDLs with high spatial resolution and in applied magnetic fields. We performed MFM measurements on samples *S2* to *S7* under the same conditions as the TbFe film (sample *S1*) at $10.5\,\mathrm{K}$, below the compensation temperature T_{comp} of $380\,\mathrm{K}$ (measured by VSM). Thus Tb moments are dominat-

ing over the Fe moments. The tip-sample distance z is kept at 7 nm using the frequency-modulated capacitive control described in Chapter 3.

5.4.1 MFM data on strongly exchange-coupled double layers (sample S2)

Similar to the data processing presented in Fig T. 4.4, the topography-induced frequency shift is obtained from the half-sum of the MFM images with up and down tip magnetizations. The magnetic frequency shift Δf_{mag}, as a result of subtracting the topographical contributions from the raw MFM data, is depicted in Fig. 5.5 for the strongly coupled sample $\mathrm{TbFe_{20nm}/[Co_{0.4nm}/Pt_{0.7nm}]_{\times 5}}$ (sample *S2*).

Figure 5.5 a) shows the as-grown domain state of sample *S2*. Similar to the MFM data acquired on the TbFe layer presented in Chapter 4, micron-sized domains are visible, but the frequency shift contrast is very low compared to sample *S1*. Recall that the distance between the top surface of the sample and TbFe layer is the same for samples *S1* and *S2*. In addition, the tip-sample distance was kept at 7 nm during all measurements of the two samples using the tip-sample distance control modes described in Chapter 3. Consequently, the comparatively small contrast is a direct result of the system comprising the additional $\mathrm{[Co/Pt]_{\times 5}}$-multilayer.

The small domains [e.g. the one at the bottom center in Fig. 5.5 a)] shrink in applied fields of 6 T [Fig. 5.5 o)] and vanish in 7 T [Fig. 5.5 p)]. The areas within the small domains appear smooth.

Based on the magnetometry and MFM data of sample *S1* (Section 4.3), the contraction of these small domains around 6 T indicates the domain-wall-motion thus the onset of the magnetization reversal process of the TbFe film. Therefore
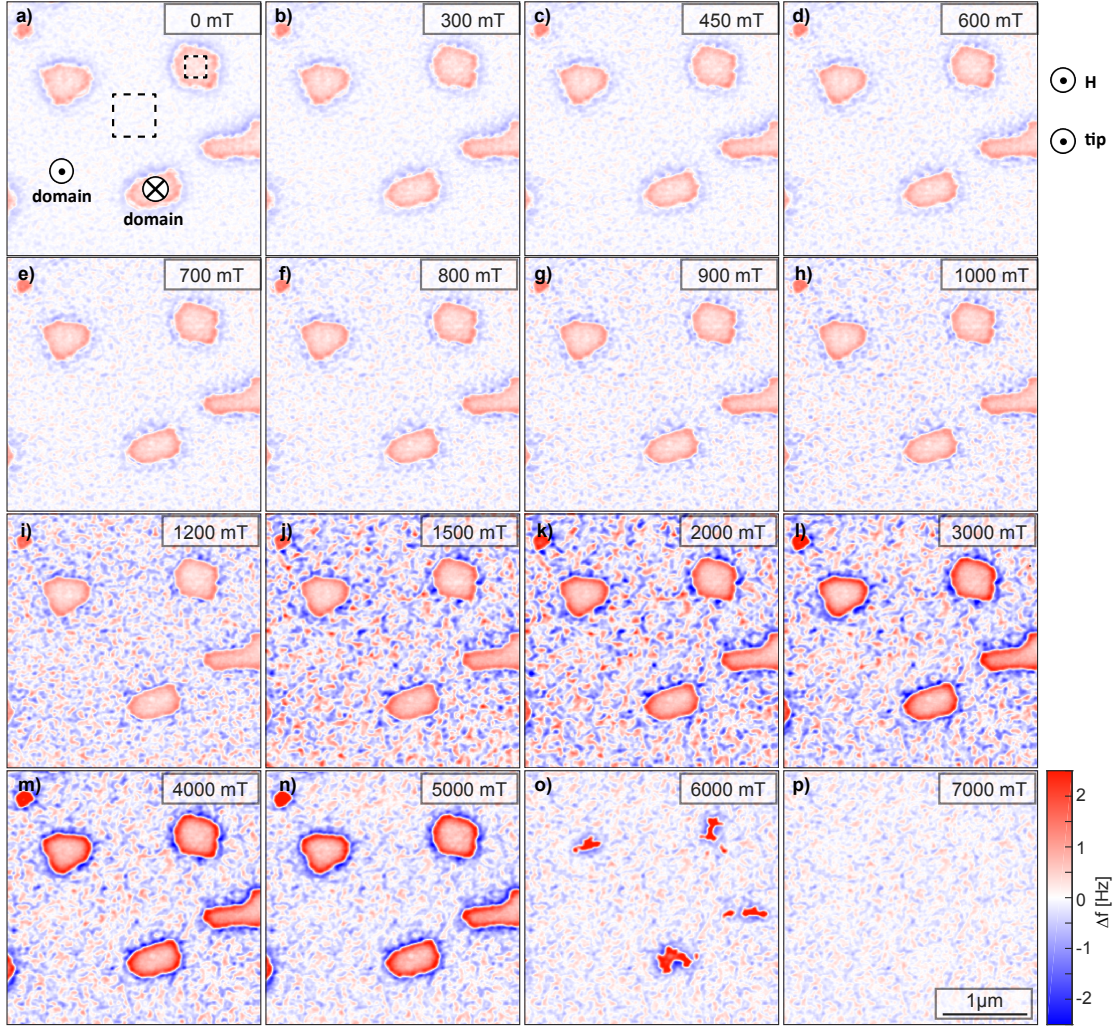
Figure 5.5: Measured frequency shift Δf_{mag} of $3\,\mu m \times 3\,\mu m$ MFM-scan on the sample $S2$, for which the topography-induced contrast is subtracted from the raw images. The color scale of -2.5 to $2.5\,\mathrm{Hz}$ is the same for all the images, as given on the right edge of the figure. The symbol $\odot$ on the top right of the figure indicate the up direction of the applied field and the tip. The symbols $\odot$ and $\otimes$ in panel a) indicate the directions of the net magnetization of the large and small domains.

the magnetization of the Tb-dominated ferrimagnetic film in these domains is down (antiparallel to the field) in Fig. 5.5 a). Because of the antiferromagnetic exchange-coupling, the magnetization of the $[\mathrm{Co/Pt}]_{\times 5}$-multilayer is up at those locations. The positive frequency shift contrast of these small domains proves

that its net magnetization is down, i.e. antiparallel to that of the tip (which is up). Hence the Tb magnetization dominates both the magnetic moment of the Fe contained in the RE film and that of the $[Co/Pt]_{\times 5}$-multilayer. The notation of up and down domains as per dominant Tb magnetization is employed henceforth.

In the large domain [marked by the symbol $\odot$ in Fig. 5.5 a)], the direction of the net magnetization in zero field is opposite to that of the small domains, i.e. the magnetization of the TbFe film is up and the magnetization of the $[Co/Pt]_{\times 5}$-multilayer is down [Fig. 5.5 a)]. A granularity appears in the large domain with a drastically increasing contrast in the field range of $1\,T$ to $2\,T$ [panels h) through k)], and a decreasing contrast in higher fields [panels m) through p)].

Note that the domain walls appear like "double domain walls" with low contrast in zero field. They evolve in applied fields up to $1\,T$ and resemble in higher fields the typical domain walls [e.g. Fig. 4.5 a) for sample *S1*]. For the small domains, in low applied fields ($<1\,T$) the frequency shift is slightly higher at the locations of the domain walls than in the center of the domains, whereas in high fields ($>2\,T$) the frequency shift at the locations of the domain walls is notably higher than that in the center of the domains [see also Fig. 2.1 for domain wall contrast].

5.4.2 Quantitative analysis of domain-level magnetic structures

To evaluate the above discussed MFM contrast in applied fields, the frequency shift contrast determined by the maximum and minimum of the MFM data shown in Fig. 5.5 is plotted in Fig. 5.6. For comparison, the contrast of MFM images on the sample *S1* is also displayed. The error bars of $\pm 0.3\,Hz$ account for the uncertainty of frequency shift from the electronic control system and the possible

113

changes of tip-sample distance during the image scans.
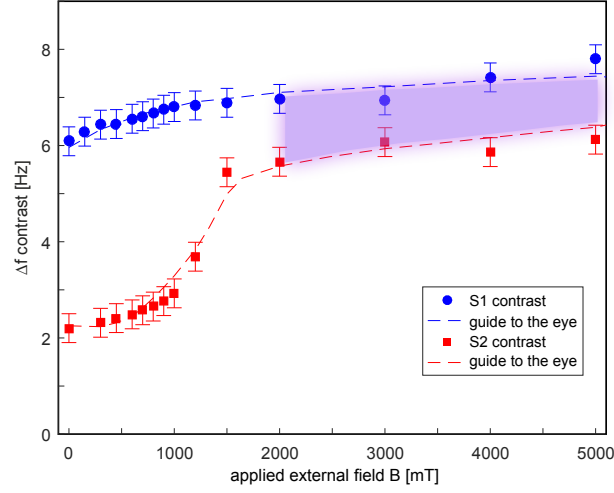
Figure 5.6: Comparison of Δf_{mag} contrast as function of applied field for samples *S1* (blue circles) and *S2* (red squares). The blue and red lines are a guide to the eye.

The contrast of sample *S2* between $0\,\mathrm{T}$ and $1\,\mathrm{T}$ is very low (around $2\,\mathrm{Hz}$), then increases drastically from $2.7\,\mathrm{Hz}$ to $5.6\,\mathrm{Hz}$ in the field range of $1\,\mathrm{T}$ to $2\,\mathrm{T}$, then increases more gradually until $5\,\mathrm{T}$. The contrast of sample *S1* is the same as shown in Fig. 4.5 p).

The low contrast of sample *S2* between $0\,\mathrm{T}$ and $1\,\mathrm{T}$, compared to sample *S1*, is due to the antiferromagnetic alignment of the Co moment of the $[\mathrm{Co/Pt}]_{\times 5}$ top layer relative to the net moment of the Tb-moment-dominated ferrimagnetic TbFe bottom layer. The magnetization reversal of $[\mathrm{Co/Pt}]_{\times 5}$ between $1\,\mathrm{T}$ and $2\,\mathrm{T}$ leads to the rapid contrast increase. For high fields from $2\,\mathrm{T}$ to $5\,\mathrm{T}$, the contrast of *S2* is approaching the *S1*, and the shaded area indicates the gap between the contrast of these two samples.

5.4.2.1   Simulation of the domain magnetization

Recall that sample *S2* consists of an underlying TbFe film and a $[Co/Pt]_{\times 5}$-multilayer. To understand the measured low contrast and the untypical domain wall of sample *S2* in zero field, the frequency shift of the TbFe film and the $[Co/Pt]_{\times 5}$ should be simulated separately from their model magnetization patterns, and summed taking into account their antiferromangetic exchange-coupling. This sum of frequency shift can be compared to the measured one.
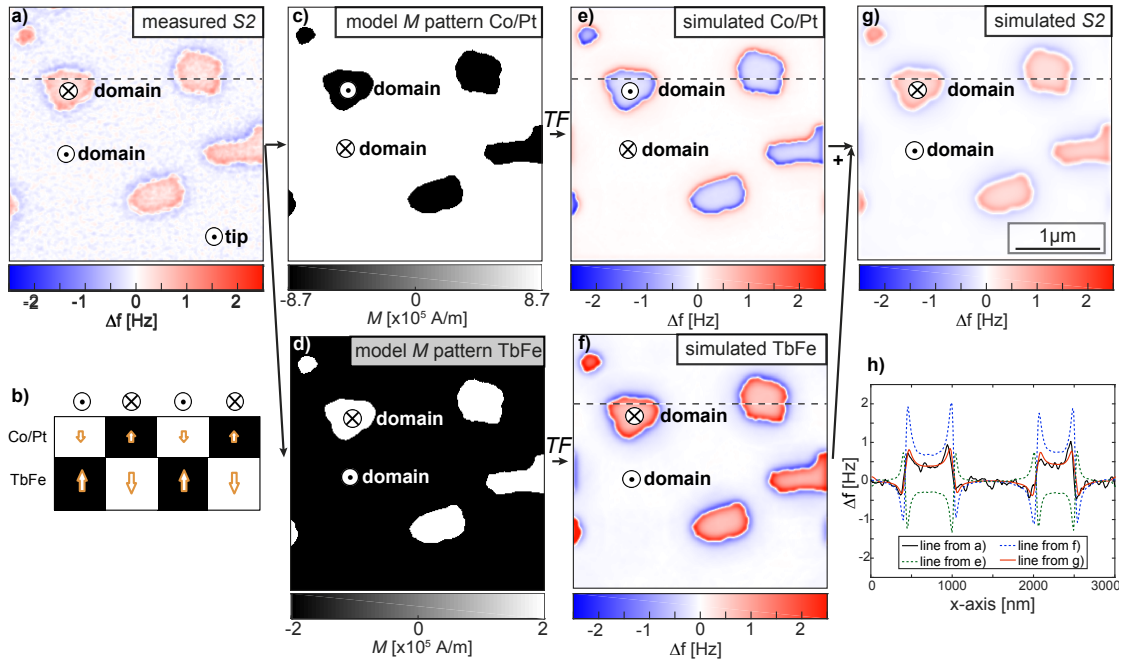
Figure 5.7: Simulation of Δf_{mag} for sample *S2* in zero field. a) Measured magnetic frequency shift. b) Schematic of the antiferromagnetically exchange-coupled $[Co/Pt]_{\times 5}$-multilayer and TbFe film. c) and d) Model magnetization pattern for the $[Co/Pt]_{\times 5}$-multilayer and the TbFe film, respectively. e) and f) Simulated frequency shift for the $[Co/Pt]_{\times 5}$-multilayer and the TbFe film, respectively. g) Simulated frequency shift for sample *S2*, as sum of e) and f). h) Δf_{mag} for horizontal dashed lines from panels a), e), f), and g).

For the simulation of the frequency shift Δf_{mag} for sample *S2*, we utilized the transfer function TF obtained in Section 2.2.1. The measured and simulated Δf_{mag}

115

are depicted in Fig. 5.7. The measured magnetic contrast in Fig. 5.7 a) is the same as Fig. 5.5 a).

The antiparallel coupling of the $[Co/Pt]_{\times 5}$-multilayer and the TbFe film sketched in Fig. 5.7 b) leads to the low frequency shift contrast in Fig. 5.7 a). The model magnetization patterns of the two layers [panels c) and d)] are acquired by multiplying their domain patterns with their magnetizations measured by magnetometry. Then the Δf_{mag} image can be simulated for each layer [panels e) and f)], using the transfer function TF [Eq. 2.10]. The simulated Δf_{mag} for sample $S2$ is obtained as the sum of simulated Δf_{mag} for the $[Co/Pt]_{\times 5}$-multilayer [e)] and the TbFe film [f)]. The horizontal dashed lines from panels a), e), f), and g) are plotted in panel h). It can be seen that the simulated Δf_{mag} [g)] matches the measurement [panel a)] quite well. The domain wall contrast is reproduced. The untypical domain wall observed in panel a) can be attributed to the double-layer structure of sample $S2$, i.e. the domain wall width is not the same for the $[Co/Pt]_{\times 5}$-multilayer and the TbFe film. In addition, the distance loss factor and thickness loss factor [see Section 2.1.1.2] of the two layers are different.

5.4.2.2   Domain-level analysis of the magnetization reversal

Based on the macroscopic magnetometry data [Fig. 5.2] and the domain-level MFM data [Fig. 5.6] of the ECDLs, the magnetization reversal of the soft layer ($[Co/Pt]_{\times 5}$) could be explained by the in-plane domain wall model by Watson et al [80]. They proposed that the magnetization reversal takes place through the formation of an in-plane domain wall inside the soft layer. The in-plane domain wall is initially formed at the top of the soft layer, then expands vertically down to the interface of the soft (In our case the $[Co/Pt]_{\times 5}$-multilayer) and hard layers

(here TbFe).

To asses the above mentioned in-plane domain wall model for sample $S2$, the frequency shift image is simulated for each field and the simulations are then compared to the measured MFM images [Fig. 5.5]. If we assumed that the in-plane domain wall does not contribute to frequency shifts in the MFM images and the magnetization is homogeneous through thickness for the $[\text{Co/Pt}]_{\times 5}$-multilayer, the $[\text{Co/Pt}]_{\times 5}$-multilayer coupled to the TbFe film [yellow area in Fig. 5.9] should give rise to the measured MFM images in applied fields. We calculated the thickness ratio between the coupled $[\text{Co/Pt}]_{\times 5}$ and the total $[\text{Co/Pt}]_{\times 5}$ in each field which reproduces the measured MFM images (in a least square root sense). This field-dependent thickness ratio is plotted in Fig. 5.8.
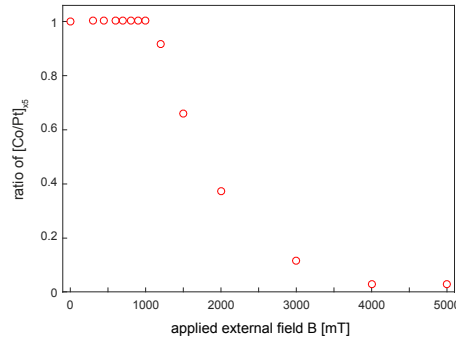
Figure 5.8: Thickness ratio between the $[\text{Co/Pt}]_{\times 5}$-multilayer which is coupled to the TbFe film and the total $[\text{Co/Pt}]_{\times 5}$-multilayer, as function of field.

The thickness ratio between the coupled $[\text{Co/Pt}]_{\times 5}$ and the total $[\text{Co/Pt}]_{\times 5}$ is 1 for fields below $1\,\text{T}$, indicating that all the $[\text{Co/Pt}]_{\times 5}$ moments are coupled antiparallel to the underlying TbFe film [see Fig.5.9 a)]. This ratio decreases from 1 to 0 in the applied field range of $1\,\text{T}$ to $5\,\text{T}$, which signifies the formation and expansion of the in-plane domain wall toward the interface [see Figs.5.9 b)-e)].

The formation and expansion of the in-plane domain wall is illustrated in Fig. 5.9.
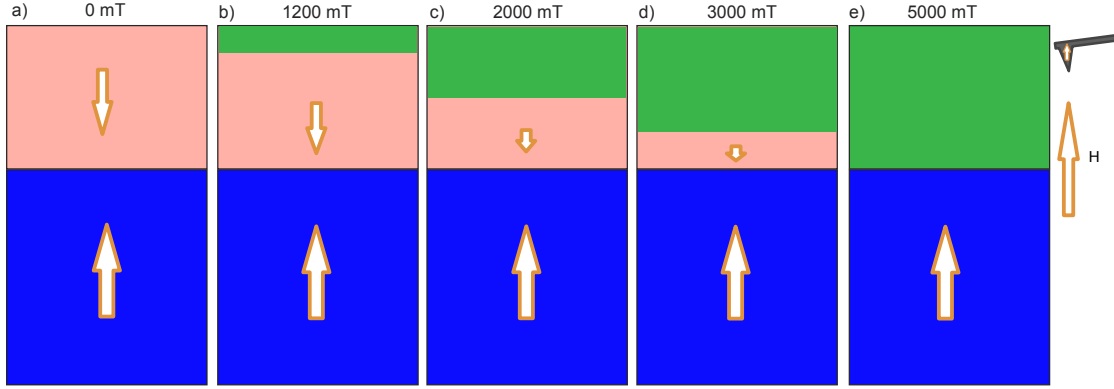
Figure 5.9: Schematics of the in-plane domain wall model in a ECDLs system. a) The soft layer is coupled antiparallel to the underlying hard layer in zero field. b) An in-plane domain wall (green area) is formed at the top of the soft layer in applied field of for example 1 T. c)-e) With increasing field, the in-plane domain wall expands toward the interface.

It is important to note that this in-plane domain wall model could account for the increase of MFM contrast as function of applied field and seem to be confirmed by the domain-level simulation of the MFM data, but it does not match the microscopic observations of the reversal process of the $[Co/Pt]_{\times 5}$-multilayer.

5.4.3 Quantitative analysis of magnetic structures within domains

We now consider the fine structures inside the domains which evolve in the applied fields, shown as "roughness" in Fig. 5.5. Note that the topography has already been removed, so the images shown are of magnetic origin.

For the quantitative analysis of these fine structures, a small area of $250\,nm \times 250\,nm$ was cropped inside the down domain and $500\,nm \times 500\,nm$ inside the up domain, as marked in Fig. 5.5a).

For the zoomed-in images inside the down domain in Fig. 5.5, the contrast remains very low. A small color scale of -0.2 to 0.2 Hz was employed for Fig. 5.10
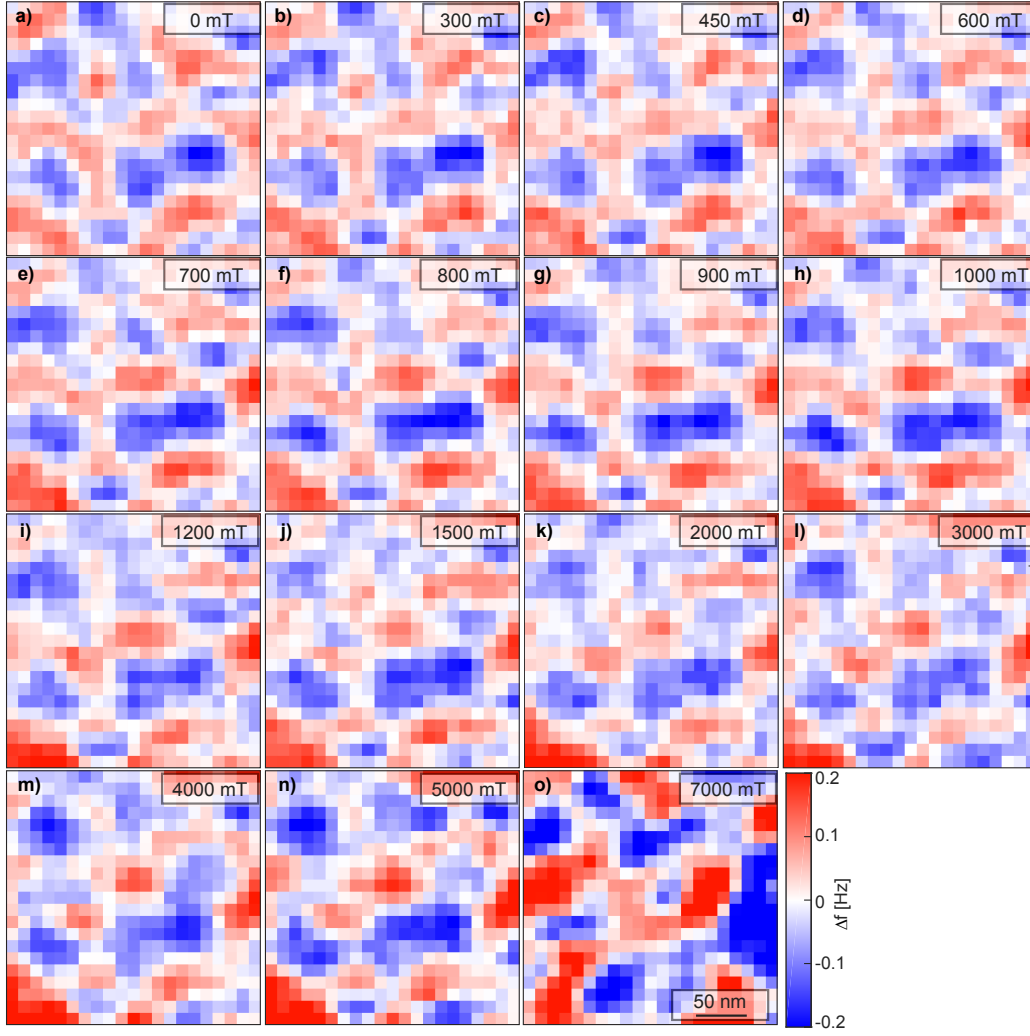
Figure 5.10: Zoomed-in images of 250nm×250nm scale inside the down domain (TbFe down, [Co/Pt]$_{\times 5}$ up), within the area marked by the dashed square in Fig. 5.5 a). Note that the color scale is between -0.2 and 0.2 Hz for the images. The image in 6000 mT is not shown due to domain-wall-motion that occurs.

to display the nano-scale magnetic structures better. A slight increase of contrast amplitude with roughly the same pattern was observed in Fig. 5.10. The image in an applied field of 7000 mT shows an inverted pattern due to the magnetization reversal of the TbFe film.

For the zoomed-in images [Fig. 5.11] for the up domain in Fig. 5.5, the color
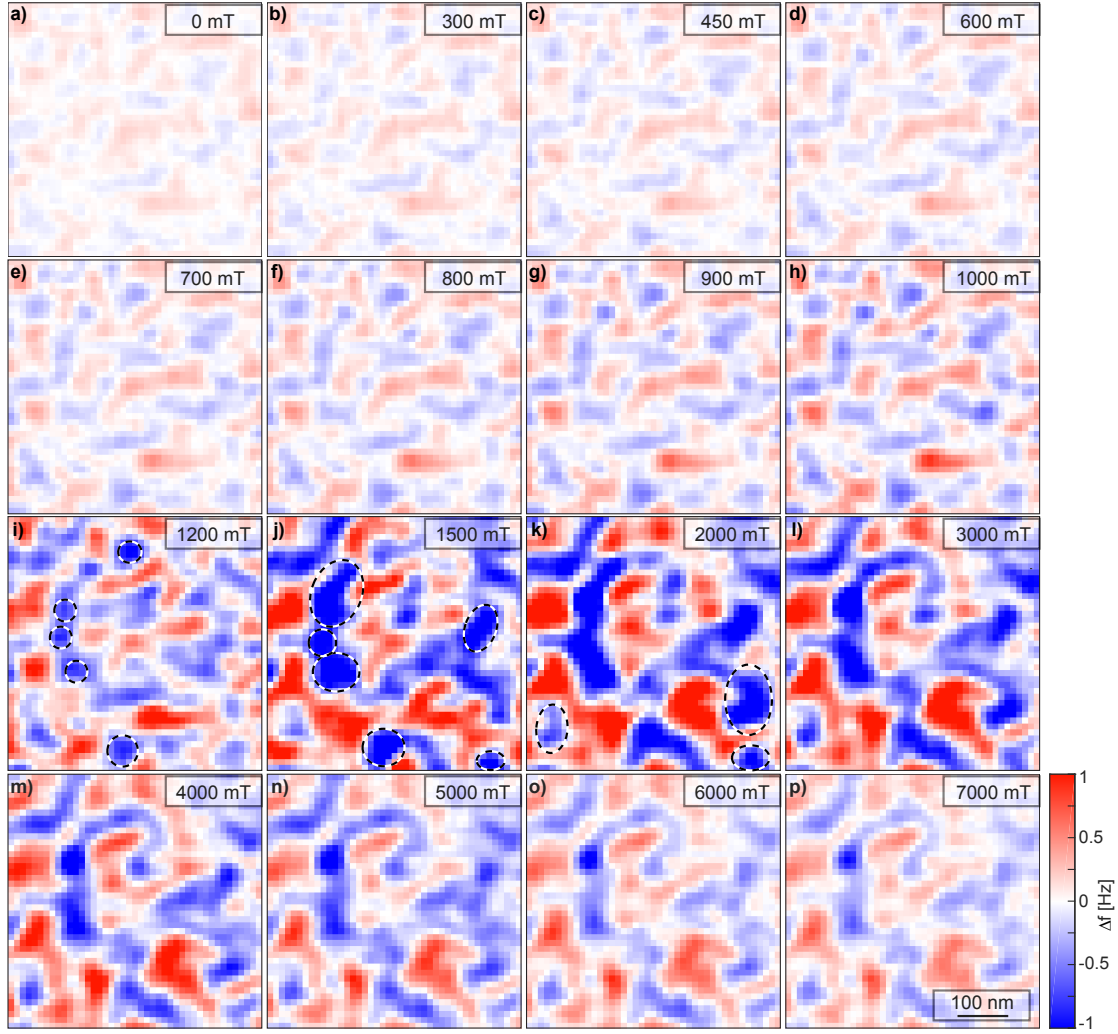
Figure 5.11: Zoomed-in images of 500nm×500nm scale inside the up domain (TbFe up, [Co/Pt]$_{\times 5}$ down), within the area marked by the dashed square in Fig. 5.5 a). Note that the color scale is between -1 and 1 Hz for the images.

scale of -1 to 1 Hz was used. The contrast increases slightly from 0 T to 1 T, and then considerably from 1 T to 2 T, and subsequently decreases gradually in applied fields from 2 T to 7 T. In addition, an evolution of the magnetic pattern in applied fields was observed, especially in the range of 1 T to 2 T [e.g. the areas highlighted by the ellipses in Fig. 5.11 i) through k)].

The magnetic contrast as function of field for the zoomed-in images of sample

S2 in Figs. 5.10 and 5.11 is plotted in Fig. 5.12 a). For the cropped area inside the down domain, the contrast increases from about 0.4 to 0.8 Hz when the applied field increases from 0 to 5 T. For the up domain, the contrast increases more evidently, from 0.7 to 4.7 Hz in the fields from 0 to 2 T, then decreases gradually toward 2.5 Hz in 5 T.
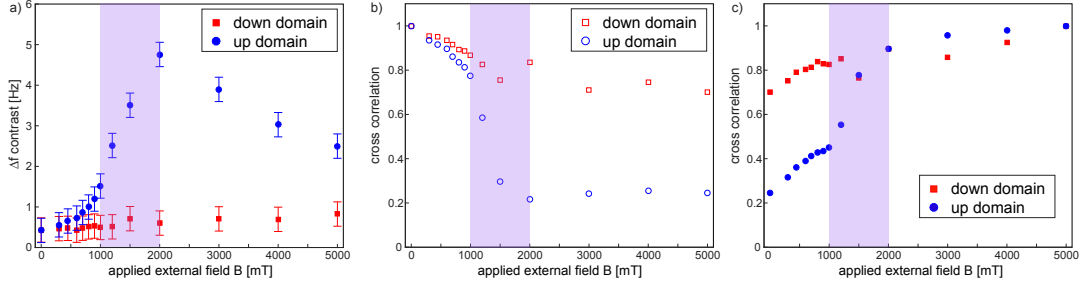
Figure 5.12: a) Δf_{mag} contrast, b) cross-correlation with respect to the 0 T image and c) cross-correlation with respect to the 5 T image as function of applied field for the cropped images inside the down and up domains, for sample *S2*.

The evolution of magnetic patterns is quantified by the cross-correlation of the MFM data in each field with respect to the 0 T image, as depicted in Fig. 5.12 b). The cross-correlation decreases by 30 % from 1 to 0.7, in fields from 0 to 5 T for the down domain. For the up domain, the cross-correlation decreases by 80 % from 1 to 0.2, in the field range of 0 to 2 T, then remains roughly the same from 2 T to 5 T. This discrepancy is also observed in Fig. 5.12 c) for the cross-correlation in each field with respect to the 5 T image. The cross-correlation expresses the magnetic pattern change, notably in the field range from 1 T to 2 T within the up domains but not the down domains, confirming the observations in Figs. 5.10 and 5.11.

Based on the observations in the cropped images within the up and down domains [Figs. 5.10 and 5.11], and the quantitative analysis of magnetic contrast and the cross-correlation of these images as function of field [[Fig. 5.12]], there are

three characteristic field regions for the up domain of sample *S2*: the low field region between 0 T and 1 T where the magnetic contrast increase slightly with roughly the same pattern; the intermediate field region from 1 T to 2 T, where the contrast increases drastically and the pattern changes; and the high field region up to 5 T where the contrast decreases while the pattern is largely maintained. These qualitative changes in the Δf_{mag} data of the ECDLs for the field ranges accordingly defines three stages in the reversal, which we analyze further in the following sections.

The main discrepancy between evolution of the magnetic contrast data in the down and up domains of sample *S2*, respectively, occurs in the field range of 1 T to 2 T [highlighted area in Fig. 5.12]. From the magnetization loop of sample *S2* discussed in Section 5.3.1, the magnetization of the $[\mathrm{Co/Pt}]_{\times 5}$-multilayer reverts in a field of about 1200 mT. This is consistent with the MFM data, indicating that the discrepancy is related to the reversal of $[\mathrm{Co/Pt}]_{\times 5}$ which takes place in applied fields between 1 T and 2 T.

5.4.3.1   Analysis of stage 2 magnetization reversal for Co/Pt

We begin with the analysis of stage 2 of the magnetization reversal, rather than stage 1, because the interpretation of it clearly singles out one specific mechanism of reversal, as we now show.

The second stage of the magnetization reversal of the $[\mathrm{Co/Pt}]_{\times 5}$-multilayer extends over applied fields from 1 T to 2 T. That is, it ranges from the approximate field level at which stage 1 is completed and pattern changes become prominent in the correlation drop [Fig. 5.12 b)], to the point where the correlation between successive images is largely maintained, as indicated by the correlation to the 5 T

image [Fig. 5.12 c)].

An increase of the magnetic contrast (as large as 4 Hz) and a drop in magnetic pattern correlation from slightly below 0.8 to 0.2 over a field range from 1 T to 2 T is observed for the magnetic structures within the up domain in stage 2. These comprise the appearance of grainy pattern of contrast with differing sign inside the up domain, which we call 'sub-domains'. These sub-domains connect magnetization states with opposite domain magnetization of $[Co/Pt]_{\times 5}$. The reversal does not take place in the same field at all locations in the up domain, as observed in Fig. 5.11. The few highlighted dark spots in panel i) are the locations where $[Co/Pt]_{\times 5}$ magnetic moments have reverted in 1200 mT. A greater number of $[Co/Pt]_{\times 5}$ moments [highlighted by the ellipses in panel j)] revert its magnetization in 1500 mT, and form sub-domains. In the field of 2000 mT, almost all the $[Co/Pt]_{\times 5}$ moments have reverted [newly reverted ones are highlighted in panel k)].

An important observation concerns the sign of the contrast change in stage 2. Notice that the contrast in the up domains is dominated by the TbFe film, which is aligned with the applied field and the magnetic tip. Consequently, it will be essentially negative, as expected for attractive interactions. An applied field will provide driving force for a reversal into alignment with the field, and accordingly only affects $[Co/Pt]_{\times 5}$ over the up domain. However consistent with this we would expect the resulting contrast change to be negative, whereas the observation is of a contrast increase.

The nature of the sub-domains can be revealed by considering the contrast produced by appropriate through-thickness isolated reversal domains in the $[Co/Pt]_{\times 5}$-multilayer. To understand this, recall that over the up domain the uniform thin films of the double layer give rise to little contrast (this is related to the thickness

loss, as previously discussed). Therefore the reversal of a column in the Co/Pt amounts to an interruption in the otherwise uniform film, which is tantamount to adding the stray field of a column of reversed magnetization. This column provides the characteristic stray field swings observed at the domain walls (this is what it ultimately is) and in particular also a positive Δf_{mag} change. Because our MFM transfer function is calibrated, we can simulate the resulting contrast quantitatively.

We carry out a simulation of such sub-domains structures using the frequency shift Δf_{mag} in 1500 mT. To that end, we apply a threshold to the measured magnetic frequency shift [Fig. 5.13 a)], which results in a bi-level magnetization pattern that we ascribe to the [Co/Pt]$_5$-multilayer, and depict in Fig. 5.13 c). The domain pattern of the TbFe film is unaltered, but we adjust the saturation magnetization to the observed field-dependent value obtained from the MFM contrast analysis of sample S2 [Section 4.3.3.1]. An iDW at the interface with TbFe reduces the thickness of the reversed sub-domain column in accordance with the observed measured contrast. Its thickness in effect constitutes a fitting parameter, adjusted to 1.1 nm in this case. The antiparallel coupling of the [Co/Pt]$_5$-multilayer (with sub-domains) and the TbFe film (same as in 0 T) is sketched in Fig. Fig. 5.13 b). The Δf_{mag} image is simulated for each layer [panels e) and f)] using the transfer function [Eq. 2.10]. Their sum is displayed in panel g).

The simulated Δf_{mag} [panel g)] reproduces the measurement [panel a)] with the correct contrast amplitude and comparable granularity of the pattern. This is the basis for asserting that stage 2 of the reversal process in the down domains consists of isolated sub-domains reverting in the Co/Pt part. Note that from their size the sub-domains are consistent with the observed composition inhomogeneity found in

124
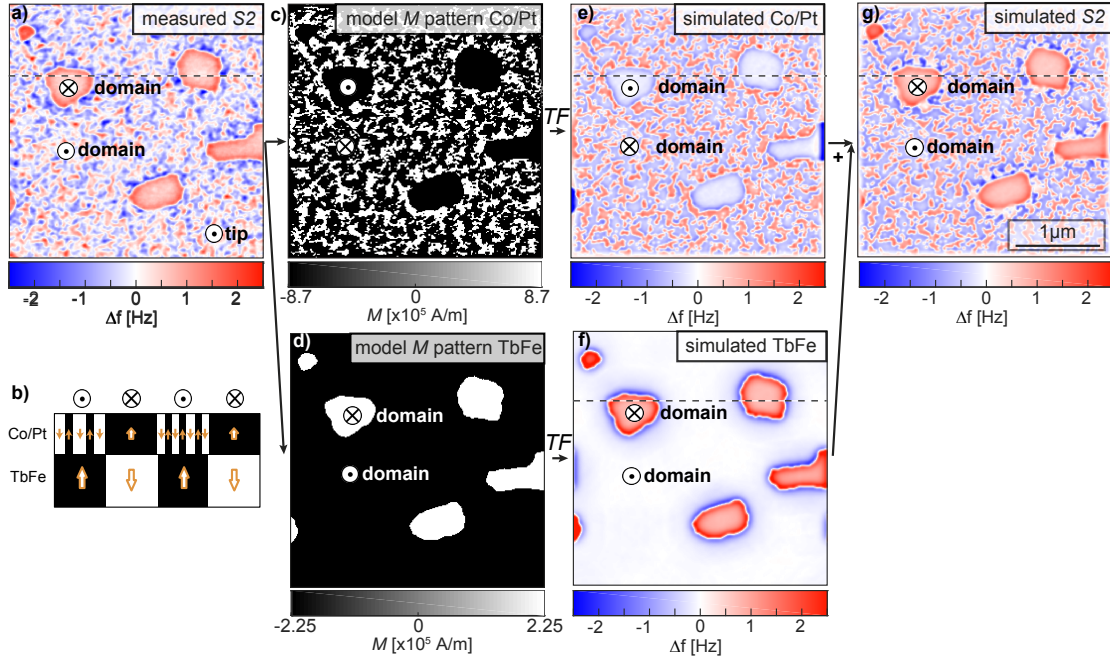
Figure 5.13: Simulation of Δf_{mag} for sample *S2* in an applied field of 1500 mT. a) Measured magnetic frequency shift in 1500 mT. b) Schematic of the antiparallel exchange-coupled $[\mathrm{Co/Pt}]_{\times 5}$-multilayer and TbFe film. c) and d) Model magnetization pattern for the $[\mathrm{Co/Pt}]_{\times 5}$-multilayer and the TbFe film, respectively. e) and f) Simulated frequency shift for the $[\mathrm{Co/Pt}]_{\times 5}$-multilayer and the TbFe film, respectively. g) Simulated frequency shift for sample *S2*, as sum of e) and f).

TbFe [see Sections 4.2 and 4.3.2]. It is conceivable that the coupling between the two layers in the ECDL varies locally in a manner related to this TbFe composition in homogeneity.

5.4.3.2 Analysis of stage 1 magnetization reversal for Co/Pt

As per Fig. 5.12 a), the contrast in $H < 1\,\mathrm{T}$ increases within the up domains by a factor of 3 without a clear change in the pattern of the magnetic structures (correlation $> 70\,\%$ in Fig. 5.12 b). By comparison, in the down domains the contrast is essentially unaltered, with an even larger correlation between images (in excess of $80\,\%$). By sheer size $(0.5 - 1.5\,\mathrm{Hz})$ the contrast changes are incompatible

with the previously assessed contrast changes in the TbFe [Fig. 4.13 a)]. Moreover, being largely restricted to the up domains, they must involve a reversal change of the Co/Pt magnetization into the direction of the field.

In view of the mechanism established in stage 2 in the previous section, we must consider the possibility that the contrast increases in stage 1 by a similar mechanism, with much sparser and smaller reversed areas through the thickness of the $[Co/Pt]_{\times 5}$. Simulations carried out in a similar manner as in Section 5.4.3.1 allow for this possibility.

On the other hand, Fig. 5.9 shows an alternative mechanism wherein the reversal sets in as a thin region at the surface of the $[Co/Pt]_{\times 5}$ opposite to the TbFe, in which the magnetic moments are turned off of the perpendicular orientation down, though not to the point of leading to the through thickness reversed columns found in stage 2. As before, the effect of this modification in the $[Co/Pt]_{\times 5}$ domain is a reduced masking of the TbFe domain pattern stray field, and hence a contrast increase which would necessarily retain any inhomogeneity found in the TbFe and reflect local changes in the amount of rotation of the $[Co/Pt]_{\times 5}$ moments.

A definite distinction is not possible at this time, because of the difficulty deconvolving the transfer function and distance losses from the measured frequency shift image in the presence of measurement noise (see previous section). Nevertheless, it is reasonable to assume that at the lowest fields the rotation of the $[Co/Pt]_{\times 5}$ moments prevails, eventually leading up to the reversal of isolated, discrete through thickness reversed columns, such as dominate stage 2.

126

5.4.3.3 Analysis of stage 3 magnetization reversal for Co/Pt

Above $2\,T$ Fig. 5.12 c) indicates that the contrast in the down domain diminishes from its peak value attained in stage 2, but exceeding $2\,Hz$ it is still larger than in stage 1. Concurrently, the correlation between the magnetic structures with those found for the maximum field is high, suggesting that no new reverted columns in the $[Co/Pt]_{\times 5}$-multilayer appear. Consistent with this picture, the $[Co/Pt]_{\times 5}$-multilayer is saturated. Nevertheless, the parallel alignment between $[Co/Pt]_{\times 5}$ and TbFe implied by this configuration necessitates breaking the coupling at the interface, i.e. the formation of the aforementioned iDW. The nature of the reversal in stage 2, comprising isolated through-thickness (except for the iDW) reverted columns suggests that the coupling strength is not uniform. An inhomogeneous iDW would be the natural consequence. The increasing field would drive the compression of the iDW toward the interface with TbFe, possibly retaining the inhomogeneity of its thickness, at least in part. This would result in the observed reduction in overall contrast while retaining the structure of the magnetization. A quantitative simulation of this process proceeds analogous to Section 5.4.2.2, and confirms the salient features of the iDW evolution in this stage. This stage 3 mechanism captures the essence of the behavior within the down domain. Indeed, prior to domain-wall-motion in TbFe at fields of $6\,T$, $[Co/Pt]_{\times 5}$ is aligned with the applied magnetic field. There is no driving force for its reversal. Accordingly, we would expect no alteration in the contrast, and this expectation largely bears out, although a small increase is observed in Fig. 5.10. However, after domain-wall-motion ensues, the magnetization of two layers is parallel, and an iDW must form and evolve as detailed for stage 3. We summarize the findings in the following section.

5.4.3.4   Summary of the magnetization reversal process

As alluded to previously, the observed contrast inside the up domain in the intermediate field region and the high field region [Fig. 5.12] can arise from the nucleation of the sub-domains and the compression of the iDWs, respectively.

In low fields below $1\,$T, the increase of contrast inside the up domain can be attributed to the rotation of local magnetic moment of $[\mathrm{Co/Pt}]_{\times 5}$. At the interface of the $[\mathrm{Co/Pt}]_{\times 5}$-multilayer and the underlying TbFe film, the local magnetic moments of the former stay pinned antiparallel to the latter, thus antiparallel to the applied field. At an increasing distance from the interface, the local magnetic moments of $[\mathrm{Co/Pt}]_{\times 5}$ are rotated to be better aligned with the field. The magnetic moments of the top layer of the $[\mathrm{Co/Pt}]_{\times 5}$-multilayer are aligned parallel to the field, given that the applied field is above the exchange-bias field of $1.2\,$T. In the intermediate fields between 1 and $2\,$T, the reversal of $[\mathrm{Co/Pt}]_{\times 5}$ is accompanied by the forming of the iDW, presumably mostly located within the $[\mathrm{Co/Pt}]_{\times 5}$-multilayer due to the high perpendicular anisotropy of the TbFe film. More iDW are formed with increasing field. In high fields above $2\,$T, the thickness of the iDWs decreases with increasing field. The compression of the iDW with increasing field was observed in Fig. 5.11 l)-p), and quantified by Fig.5.6 where the shaded area highlights the closing gap between the contrast of the samples *S1* and *S2*.

It is important to note that the domain-level in-plane domain wall model [Fig. 5.9] is proved to be an incomplete picture of the magnetization reversal process of the $[\mathrm{Co/Pt}]_{\times 5}$-multilayer. Thanks to our high-resolution MFM images showing magnetic structures of down to $20\,$nm scale, the sub-domain model [Fig. 5.9] of $[\mathrm{Co/Pt}]_{\times 5}$ magnetization reversal matches the MFM data within the domains, and

provides a nano-scale understanding of the reversal process.

The magnetization reversal process of sample *S2* is illustrated in Fig. 5.14. The left panels depict the MFM images in various fields, and the middle ones are the corresponding schematics of the cross-section view of the double layers. The symbols $\odot$ and $\otimes$ indicate the direction of the domains for the middle panels. In 7000 mT, the dashed lines in panel i) indicate the previously existing domain walls.

Figure 5.14 a) shows the as-grown sample in 0 mT. Magnetometry and comparing MFM data with simulations (see Section 5.4.2) indicate antiferromagnetic coupling of the $[Co/Pt]_{\times 5}$-multilayer and the TbFe film [panel b)]. In 600 T, an increase of roughness in observed within the up domains [panel c)], which could be attributed to the rotation of $[Co/Pt]_{\times 5}$ moments which is distributed inhomogeneously [sketched by the green areas in panel d)]. The local magnetic moments of $[Co/Pt]_{\times 5}$ are antiferromagnetically exchange-coupled to the TbFe layer at the interface, while the moments on the top can be rotated [see zoomed image] due to the applied field. In a field of 1500 mT (up direction), a pattern of sub-domains appears within the $[Co/Pt]_{\times 5}$ domain with initially down magnetization [panel e)]. The magnetization of sub-domains [blue areas within the up domains in panel f)] in the up direction and iDWs are formed at the interface [green areas in panel f)]. As discussed in Section 5.4.3.1, the reversal of $[Co/Pt]_{\times 5}$ occurs mainly between 1000 mT and 2000 mT. In fields above 2000 mT, the MFM signal reflects TbFe domains and variations of the iDW thickness which decreases with increasing field, but remains visible even in 5000 mT [panels g) and h)]. The iDW of an inhomogeneous thickness is highlighted in panels h) and zoomed on the right. In 7000 mT, above the TbFe coercivity of about 6 T, the TbFe film is saturated [panel i)]. The roughness at the locations of initial $[Co/Pt]_{\times 5}$ up-domains [within dashed lines in
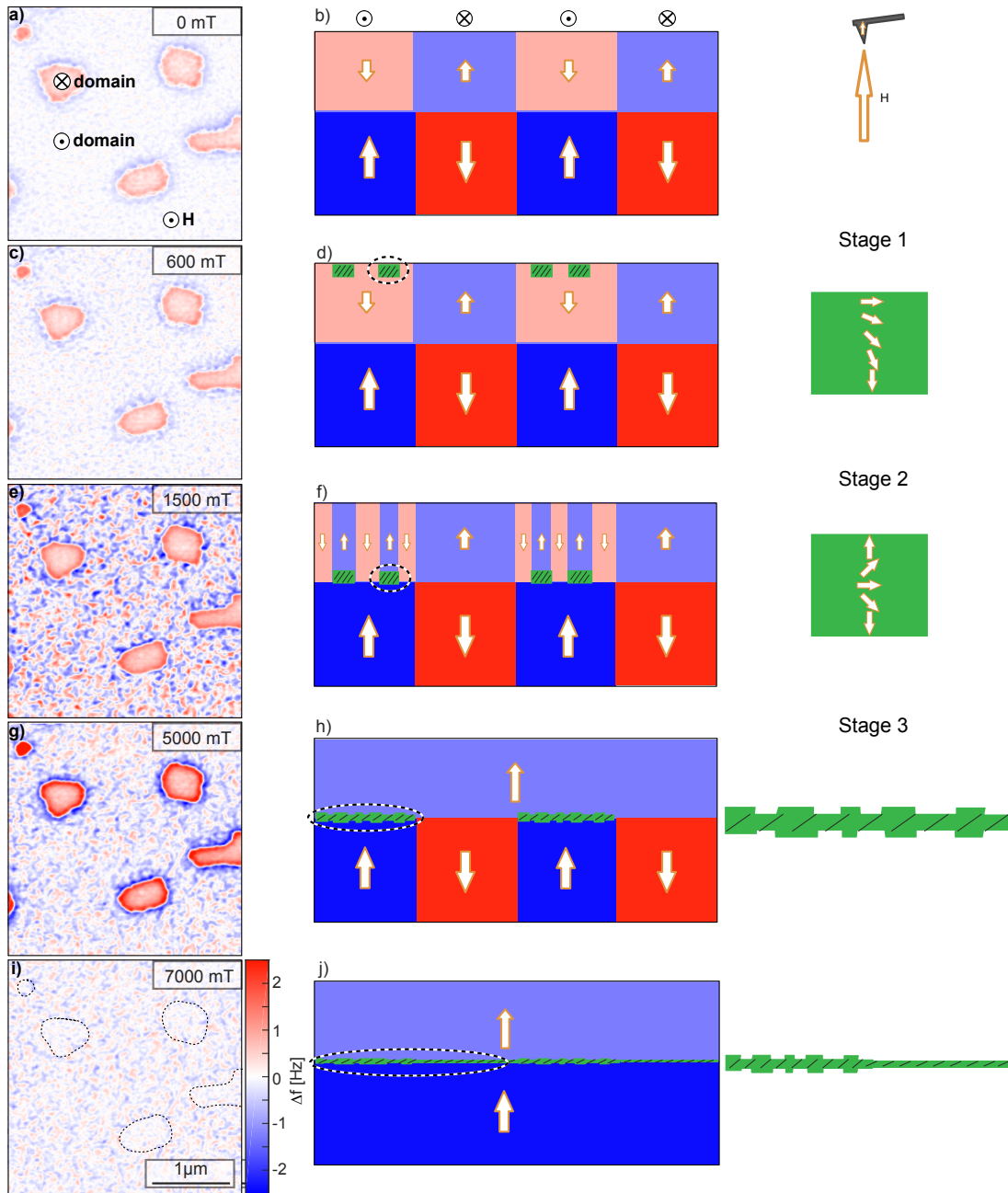
Figure 5.14: Illustration of the magnetization reversal process of sample *S2*, with MFM images in the left panels and schematics in the middle panels. The in-plane domain walls highlighted by the dashed ellipses are zoomed on the right of the corresponding schematic. Note that the aspect ratio of the in-plane domains walls are not maintained in the zoomed images.

panel g)] is lower than that outside these areas [panel j)]. This roughness can arise from the thickness variations of the both layers, the inhomogeneous distribution of the composition of the TbFe film (and the related Tb/Fe fanning cones), and the iDW with locally varying thickness which plays an important role.

5.4.4 MFM data on exchange-coupled systems with Pt interlayer

5.4.4.1 Exchange-coupled systems with thin Pt interlayer

We have performed MFM scans under the same conditions on the ECDLs of $[Co/Pt]_{\times 5}$-multilayer and TbFe film with Pt interlayer of various thicknesses. For the samples with Pt interlayer thickness up to 2.0 nm (samples *S3*, *S4*, *S5*, *S6*), the magnetization reversal is dominated by the nucleation of sub-domains appearing within the $[Co/Pt]_{\times 5}$ domain with magnetization initially opposite to the applied field. The MFM data of sample *S4* is presented as an example.

Sample *S4* comprises a Pt layer of 0.7 nm at the interface between the TbFe film and the $[Co/Pt]_{\times 5}$-multilayer, as illustrated in Fig. 5.1 c). The MFM images of sample *S4* are depicted in Fig. 5.15.

The observed stage 2 reversal of the $[Co/Pt]_{\times 5}$ multilayer starts in 600 mT (where the magnetic contrast increases notably) [Fig. 5.15 d)]. This field level is consistent with the H_{ex} of about 0.5 T obtained from the VSM measurements [Fig. 5.2]. Similar to sample *S2*, the magnetization reversal is not homogeneous for sample *S4*. The measured frequency shift contrast in panels d) through k) arise from the evolving sub-domains between 700 mT and 2000 mT. At 3000 mT the Co/Pt reversal is complete, except for the compression of the iDW, which proceed as found for stage 3 in sample *S2*. The panels l) through o) depict the Δf_{mag} contrast
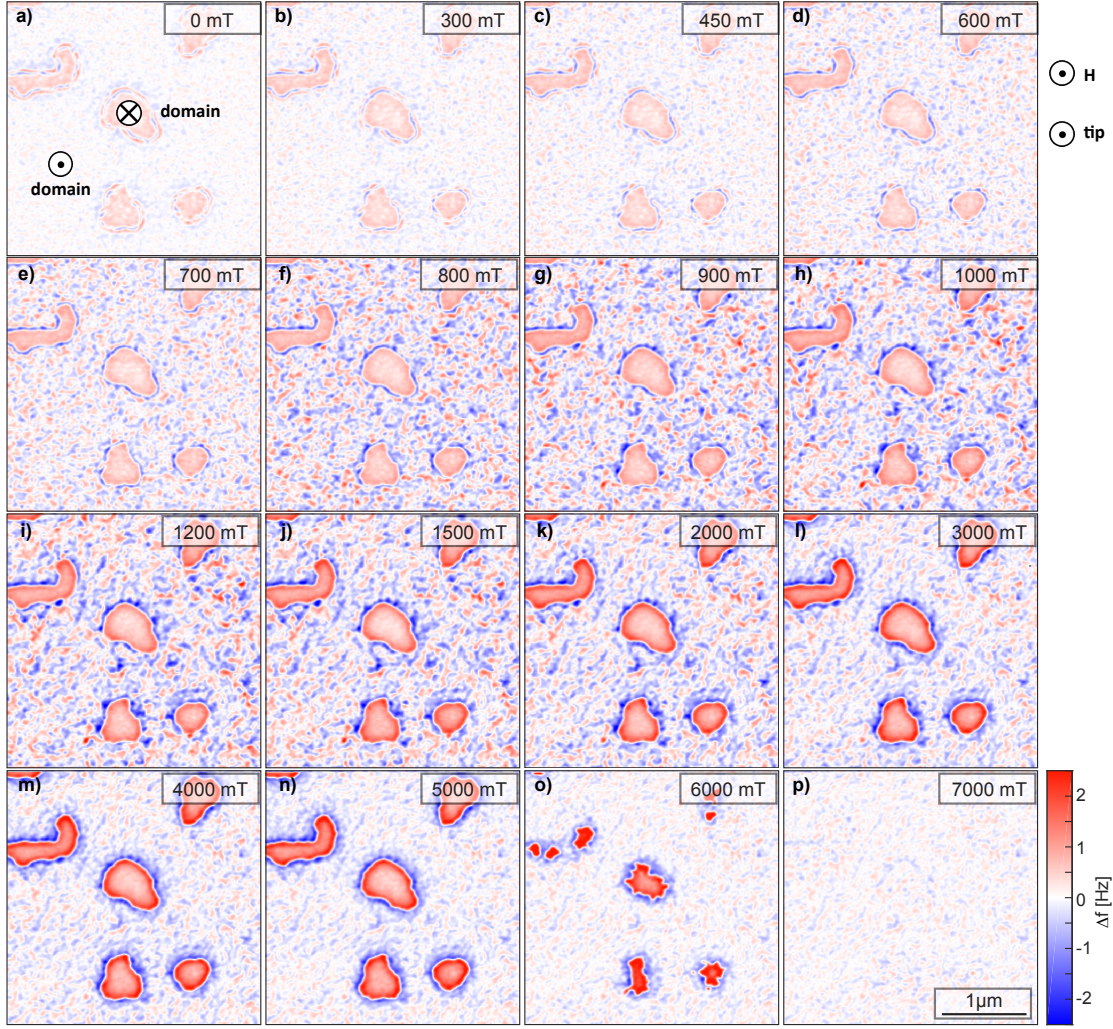
Figure 5.15: Measured frequency shift Δf_{mag} of $3\,\mu\mathrm{m}\times 3\,\mu\mathrm{m}$ MFM-scan on the sample S4, for which the topography-induced contrast is subtracted from the raw images. The color scale of -2.5 Hz to 2.5 Hz is the same for all the images, as given on the right edge of the figure.

decrease in fields from 3000 mT to 6000 mT as a result of the stage 3 compression of the iDW. Domain-wall-motion in the TbFe film starts around 6000 mT [o)], and is complete at 7000 mT [p)], which is also consistent with the magnetometry data in Fig. 5.2.

The frequency shift images show some common characteristics for samples S3-

$S6$, which indicate that the overall coupling strength between TbFe and Co/Pt is reduced but not removed by Pt spacer layers of up to 2.0 nm. Figures 5.15, 5.16, 5.17, and 5.18 show the series of field-dependent measurements of the samples. All were carried out under the same conditions as Fig. 5.5, and with the same calibrated tip, so that we can compare the contrast features.
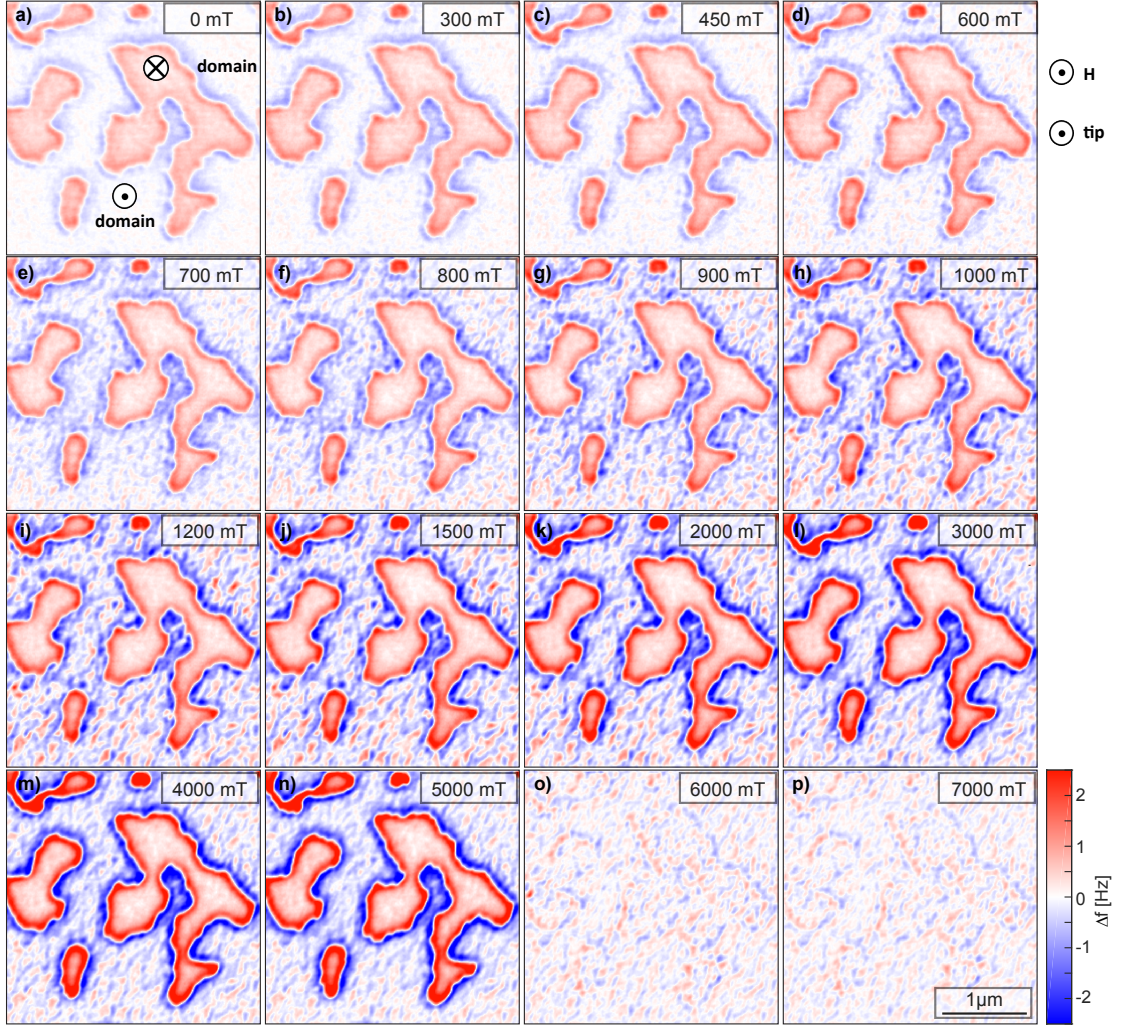
Figure 5.16: Measured frequency shift Δf_{mag} of 3 µm×3 µm MFM-scan on the sample TbFe/Pt$_{0.4\mathrm{nm}}$/[Co/Pt]$_{\times 5}$ ($S3$), for which the topography-induced contrast is subtracted from the raw images. The color scale of -2.5 Hz to 2.5 Hz is the same for all the images, as given on the right edge of the figure.
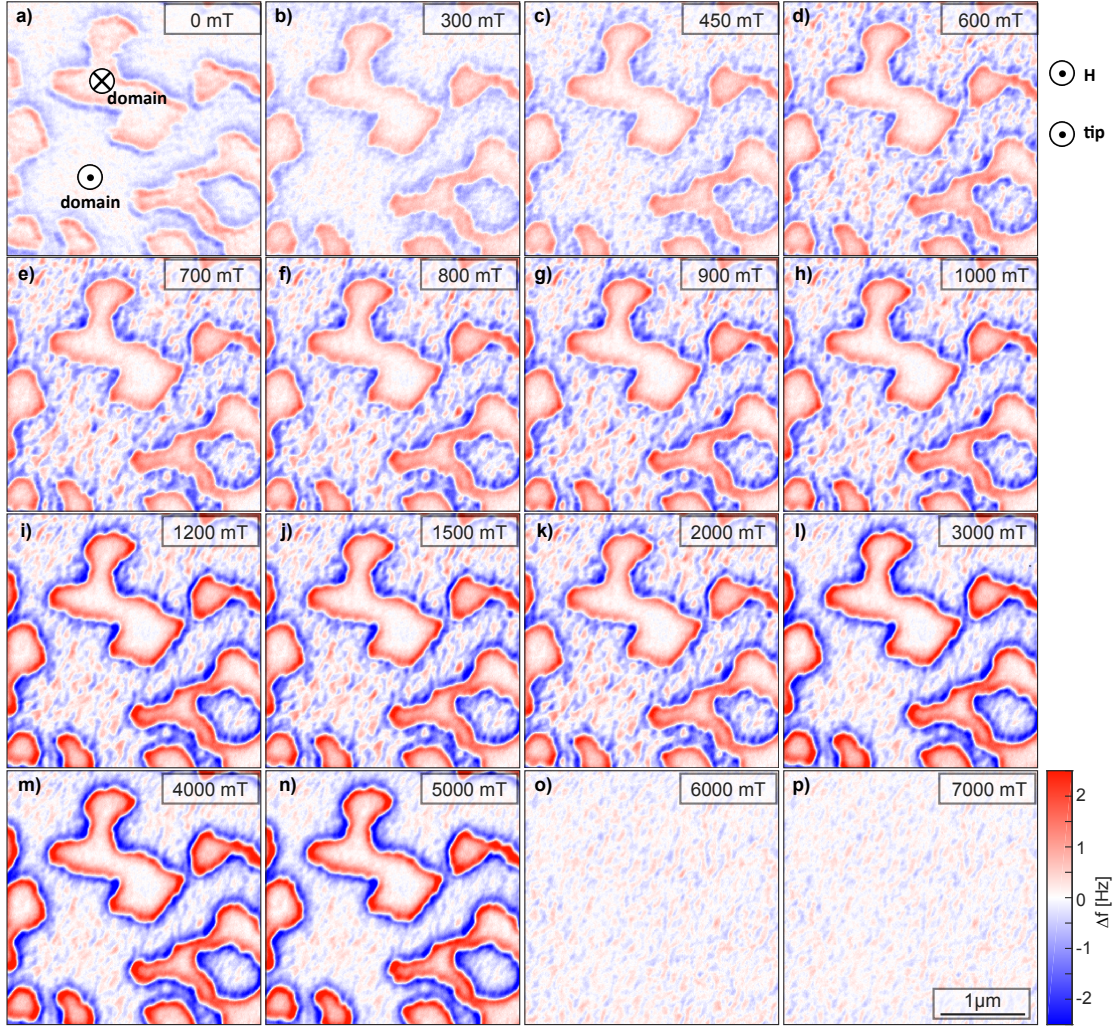
Figure 5.17: Measured frequency shift Δf_{mag} of $3\,\mu\mathrm{m}\times3\,\mu\mathrm{m}$ MFM-scan on the sample TbFe/Pt$_{1.2\mathrm{nm}}$/[Co/Pt]$_{\times5}$ ($S5$), for which the topography-induced contrast is subtracted from the raw images. The color scale of -2.5 Hz to 2.5 Hz is the same for all the images, as given on the right edge of the figure.

Firstly, the domain-level magnetic contrast increases monotonically with applied fields from 0 mT to 4000 mT. Secondly, the magnetic roughness inside the up domains increases in fields up to 1500 mT, then decreases from 1500 mT to 4000 mT. Thirdly, the domain wall contrast is low in 0 mT, and becomes higher in higher fields. These observations reproduce for $S3$, $S5$ and $S6$ the same stages already
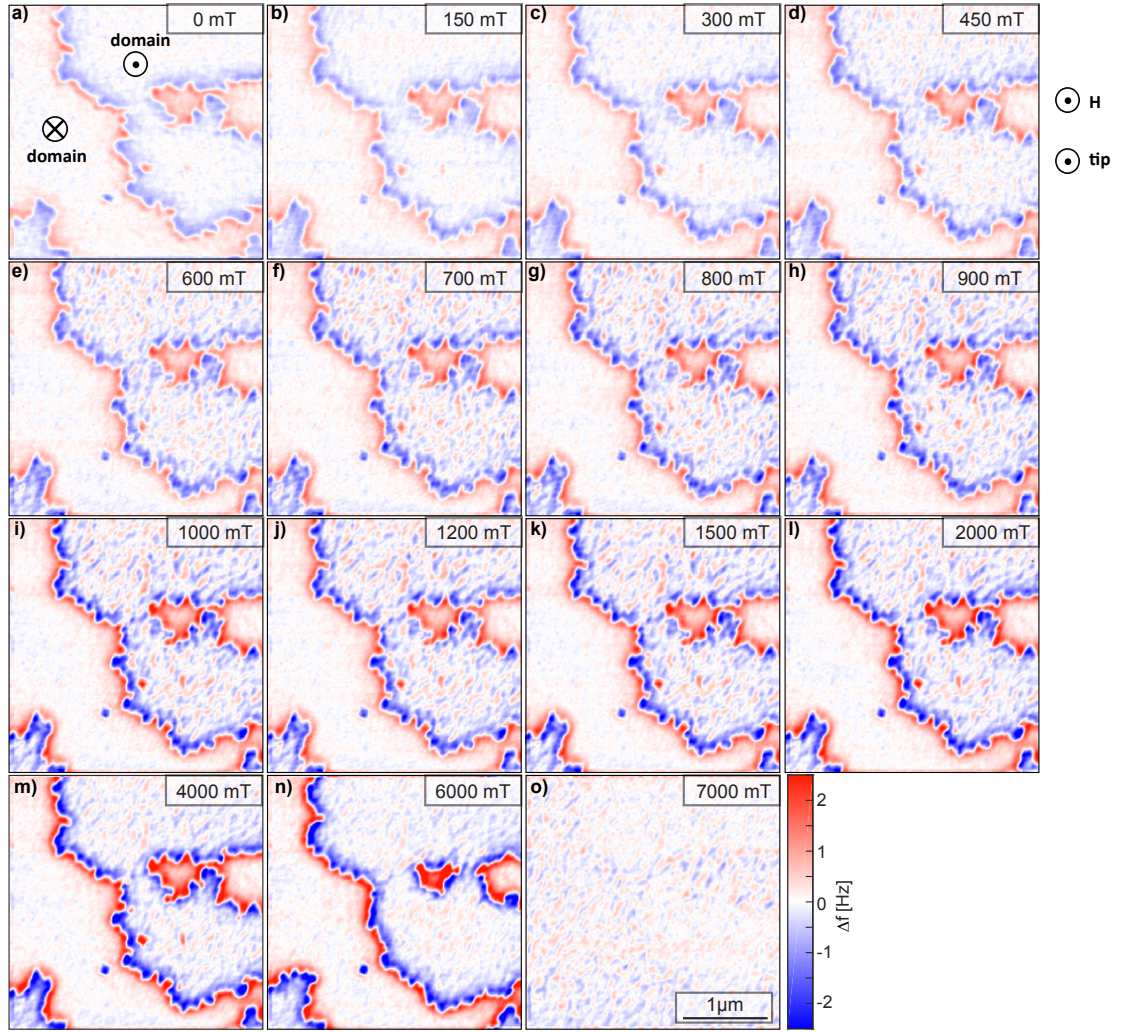
Figure 5.18: Measured frequency shift Δf_{mag} of $3\,\mu\mathrm{m}\times 3\,\mu\mathrm{m}$ MFM-scan on the sample TbFe/Pt$_{2.0\mathrm{nm}}$/[Co/Pt]$_{\times 5}$ (*S6*), for which the topography-induced contrast is subtracted from the raw images. The color scale of -2.5 Hz to 2.5 Hz is the same for all the images, as given on the right edge of the figure.

observed and discussed for sample *S2* and identified in *S4*.

Note that the onset of stage 2, characterized by the contrast increase and correlation loss (not shown) arising from the subdomains is initiated at different field levels for *S3*-*S6* than *S2*. The characteristic appearance of sub-domains occurs in lower fields for samples with thicker Pt interlayers. As much is indicated by

the onset of the increase of contrast roughness inside the up domains, in fields above 450 mT for samples *S3* and *S4*, and below 450 mT for samples *S5* and *S6*. This reduction of the threshold for the formation of sub-domains was to be expected, since the increasing thickness of Pt spacing layers will reduce the coupling strength whose inhomogeneity we associated with the appearance of local Co/Pt sub-domains.

Figure 5.19 provides an overview of samples *S3*, *S4*, *S5* and *S6* with Pt interlayer thicknesses of 0.4, 0.7, 1.2 and 2.0 nm, respectively. The MFM images over an area of 3 µm×3 µm in applied fields of 0, 450, 900, 1500 and 4000 mT are displayed for each sample. These fields are selected to demonstrate the magnetization reversal of the $[Co/Pt]_{\times 5}$-multilayer. The color scale of -2.5 Hz to 2.5 Hz is the same for all the images, as given on the right edge of the figure. The applied field and the tip magnetization are in the up direction, and the magnetizations of the domains are marked by the symbols $\odot$ (up) and $\otimes$ (down) in the zero field images for each sample. Note that the net magnetic moment of these ECDLs is dominated by the TbFe film, and thus the $[Co/Pt]_{\times 5}$ moments are antiparallel to the applied field at the location of the up domains.

5.4.4.2   Exchange-coupled systems with thick Pt interlayer

Sample *S7* comprises the thickest Pt spacer layer of the series, at 2.5 nm. The MFM images and the schematics for the magnetization reversal process of sample *S7* are presented in Fig. 5.20. The portrayal of the reversal in this case is complicated by the weakness of the coupling between TbFe and Co/Pt, due to which the sample switching coincides with the tip switching. As a result it was not possible to reproduce the same series of field measurements as for samples *S2*-*S6*.
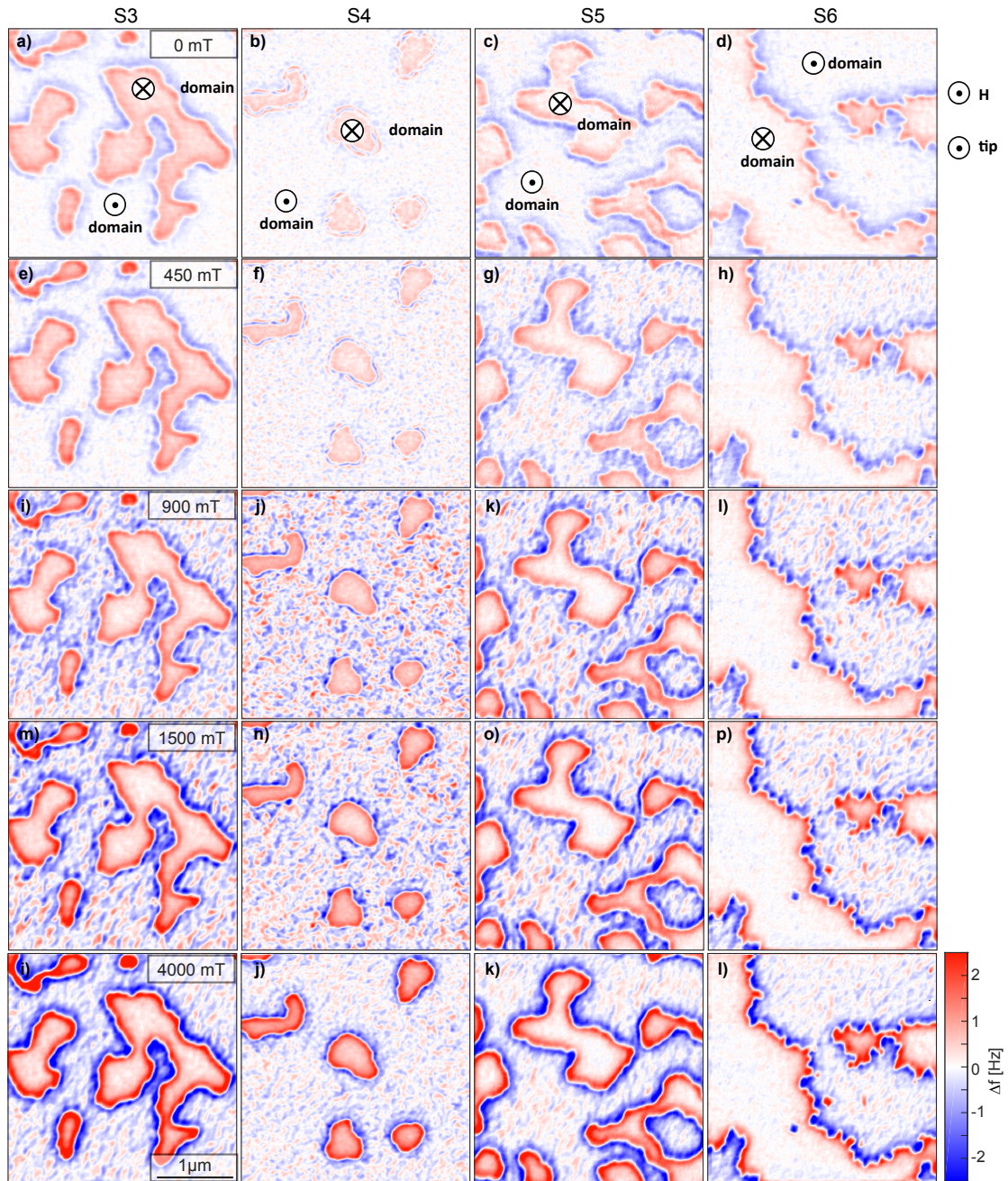
Figure 5.19: Overview of magnetic frequency shift Δf_{mag} images for samples *S3*, *S4*, *S5* and *S6* in columns from left to right, and in applied fields of 0, 450, 800, 1200, 2000 and 4000 mT are displayed in rows from top to bottom.
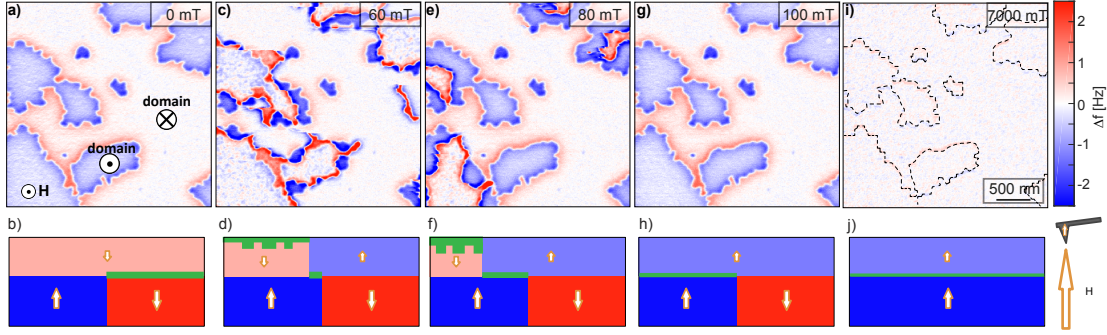
Figure 5.20: Illustration of the magnetization reversal process of sample *S7*, with MFM images in the top panels and schematics in the bottom panels. Note that the process is not directly comparable to that depicted for samples *S2-S6* on account of the fact that the Co/Pt was in a remanent state in 0 T (a consequence of creating a domain state in TbFe by driving the sample toward the TbFe coercivity at 6 T, thereby saturating Co/Pt).

The MFM images in Fig. 5.20 a) c) e) g) i) depict the magnetic frequency Δf_{mag} of sample *S7* in applied fields in the up direction. For prior MFM scans of this sample *S7* (not shown), fields as high as 1 T have been applied. These field levels are above the coercivity of the $[\mathrm{Co/Pt}]_{\times 5}$-multilayer and place the $[\mathrm{Co/Pt}]_{\times 5}$-multilayer in a remanent state comprising a single domain. Therefore, the MFM image in Fig. 5.20 a) shows the remanent state of the $[\mathrm{Co/Pt}]_{\times 5}$-multilayer and the domain state of the TbFe film in 0 T. Since (as samples *S2-S6*) the magnetic moment of the TbFe film is higher than the $[\mathrm{Co/Pt}]_{\times 5}$-multilayer, the up domains (e.g. the one marked by the symbol $\odot$) are TbFe up domains. Comparing image a) and g) indicates that in both cases the $[\mathrm{Co/Pt}]_{\times 5}$-multilayer is saturated, and consequently does not significantly contribute to the contrast. For an applied field of 60 mT [panel c)], a domain-wall-motion of the $[\mathrm{Co/Pt}]_{\times 5}$-multilayer was observed, and roughness is increased within the $[\mathrm{Co/Pt}]_{\times 5}$ domains which are overlapping the TbFe up domains. This roughness is attributed to the rotations of the Co/Pt magnetic moments in an applied field (highlighted in green in Fig. 5.20 d)). In

80 mT [panel e)], further domain-wall-motion of the $[Co/Pt]_{\times 5}$-multilayer was observed. Surprisingly, it follows from the direction of motion of the Co/Pt domain walls, that the coupling between TbFe and Co/Pt is antiparallel, and therefore cannot be dipolar in first instance. Again, a higher roughness is observed within Co/Pt domains which are overlapping the TbFe up domains. In 100 mT [panel g)], the $[Co/Pt]_{\times 5}$ domain walls have vanished and $[Co/Pt]_{\times 5}$ is saturated while the TbFe film is still in a multi-domain state. In 7000 mT, above the TbFe coercivity of about 6 T, the TbFe film is saturated [panel i)] (the dotted lines indicate the locations of TbFe domain walls before saturation).

The remanent state of the $[Co/Pt]_{\times 5}$-multilayer and the domain state of the TbFe film in 0 T is sketched in panel b). The domain-wall-motion and the sub-domain nucleation of the $[Co/Pt]_{\times 5}$-multilayer in 60 mT is illustrated in panel d). In 80 mT [panel f)], the $[Co/Pt]_{\times 5}$ down domains shrink further within which more iDW are formed. Panel h) shows the saturated state of the $[Co/Pt]_{\times 5}$-multilayer and the multi-domain state of the TbFe film in 100 T. In 7000 mT, the TbFe film is saturated [panel j)]. The iDW are marked in green at the locations where the antiferromagnetic exchange-coupling is broken.

Interestingly, the magnetization reversal process of sample *S7* with 2.5 nm thick Pt interlayer is very different from sample *S6* with 2 nm thick Pt interlayer. For the ECDLs of TbFe and $[Co/Pt]_{\times 5}$, the fine tunning of the exchange-bias and the understanding of the magnetization reversal mechanism can be of great interest for their potential applications in high density magnetic recording.

6 Summary and outlook

6.1 Summary

The studies presented in this thesis provide a first look at the microscopic characteristics of magnetic structures in the magnetron sputtered thin films of the ferrimagnet $Tb_{25}Fe_{75}$ and of ECDLs using this material and the $[Co/Pt]_{\times n}$-multilayer. The ferrimagnet is a high perpendicular-anisotropy material, which exchange couples antiferomagnetically the likewise perpendicular-anisotropy ferromagnetic Co/Pt.

We show by high resolution quantitative MFM at low temperatures that the reversal process in ECDLs involves four processes with corresponding field regions. There is an increase in the magnitude of the areal density of magnetic moments of the ferromagnet with applied field lower than $1\,T$, the local breaking of the coupling between ferrimagnet and ferromagnet between 1 and $2\,T$, the inhomogeneous compression of the resulting in-plane domain wall in higher fields, and finally the lateral domain-wall-motion within the ferrimagnet at fields in excess of $5\,T$.

We have investigated the possible influence of Pt spacing layers between ferro- and ferrimagnetic layers. These could be used to control the coupling between layers of the system. Our findings corroborate the partial decoupling conferred by Pt when the thickness increases from 0 to $2\,nm$. At $2.5\,nm$ the two layers are largely decoupled and lateral domain-wall-motion of each layer separately is possible.

The understanding we gained will aid the development of applications that exploit the strong non-frustrated coupling in these ECDLs.

A further important result from this work is the technical development steps we have taken in order to be able to carry out the research. We anticipate that these

achievements will find further use in the study of the reversal of magnetization in high fields and at a local scale. Specifically, having recognized the crucial nature of scanning at a controlled tip-sample distance of about 10 nm and below, and having assessed artifacts induced by dissipation mechanisms in applied magnetic fields, we implemented a frequency-modulated capacitive distance control method that allows the desired control robustness and accuracy. Moreover, we complemented this control method with techniques to reduce the influence of positional creep on the ability to carry out quantitative analysis of the data. We refined the quantitative MFM analytics techniques, making extensive use of the qMFM analytics package for Matlab (see http://qmfm.empa.ch).

6.2 Outlook

6.2.1 TbFe with various compositions

The magnetic properties of amorphous TbFe alloy thin films, for instance the compensation temperature, depend strongly on the composition. Because the driving force for reversal is the Zeeman energy, closeness to the compensation will affect the coercivity, in addition to the temperature dependent barriers to domain-wall-motion given by anisotropy and exchange stiffness. It is important to establish the generality of the observed reversal mechanisms by analyzing them in conjuntion with different TbFe compositions.

Moreover, the observed inhomogeneities in our TbFe film could be closely connected to the atomic ratio of 25 % Tb and 75 % Fe.

Given how inhomogeneity can affect reversal mechanisms, it is crucial to investigate into TbFe films with various compositions, with a special focus on these compositional inhomogeneities and the phase diagram. The nature of the various

contributions to the anisotropy in these films should be studied further by linking the inhomogeneity of the composition to the magnetic properties.

6.2.2 ECDLs of TbFe and [Co/Pt]$_{\times 5}$ with other interlayers

The polarization of Pt, in the [Co/Pt]-multilayer and as the interlayer, is not fully understood. To simplify the ECDLs systems with an interlayer, Cu and Ag might be used as interlayers.

6.2.3 Simulations of interfacial domain walls in TbFe/[Co/Pt]$_{\times 5}$

While it is clear from the data that in-plane interfacial walls exist in these ECDLs, we have not carried out a micromagnetic simulation thereof. Completing this task would be important when these systems are considered for devices in which the active cross section is small.

6.2.4 Investigation on the low-field feature of TbFe magnetometry

The low-field feature, i.e. strong variation of measured VSM signal at low fields [Section 4.3.1], is observed in the out-of-plane magnetization loops of all our TbFe alloy films and TbFe-based films. In this theses we attribute it to the instrument-specific artifacts. In principle, the MFM results are not affected by this low-field feature. However, the origin of this low-field feature needs more investigations.

There are possibilities that the low-field feature arises from the sample fabrication. For example, the coating on the sides of the Si substrates with a slanted surface could contribute a soft-phase or an in-plane component to the measured VSM loop. To avoid the former problem, various strategies could be used, some

142

of which are already being implemented, namely the use of masks or lithography to better define the edges of the sputtered area. Additional XMCD measurements will be used for confirming the magnetization loops.

List of Figures

144

145

146

147

3.2 Schematics of the PLL and side bands detection systems required for frequency-modulated capacitive distance control in high resolution MFM. The first PLL (blue box) mechanically drives the cantilever on its first flexural mode, f_c, and keeps the oscillation amplitude at A_0. The shift of resonance frequency $\Delta f(x,y)$ is a measure for the magnetic stray field of the sample. The z-feedback (z-PI) adjusts the tip-sample distance to keep the amplitudes of the side-bands at $f_c + 2f_{ac}$ and $f_c - 2f_{ac}$ constant. A measure of the topography is either obtained from the variation of the side-band amplitudes or by the z-feedback output, for slow or fast z-feedback parameters, respectively. The circuitry used for the control of the tip-sample distance is highlighted by the green box. Using two additional lock-in amplifiers (LIA 2 and LIA 3), the two side band amplitudes at $f_c + f_{ac}$ and $f_c - f_{ac}$ can be measured and zeroed by a Kelvin feedback ($U_{dc}^{(K)}$-PI). The latter adjusts the applied bias voltage to compensate the contact potential (yellow box). The setup has been implemented with a Zurich Instruments lock-in amplifier PLL system HF2LI [45] .

Bibliography

[1] Y Mimura, N Imamura, T Kobayashi, A Okada, and Y Kushiro. Magnetic properties of amorphous alloy films of fe with gd, tb, dy, ho, or er. *Journal of Applied Physics*, 49(3):1208–1215, 1978.

[2] KHJ Buschow and AM Van der Kraan. Magnetic properties of amorphous rare-earthâĂŤiron alloys. *Journal of Magnetism and Magnetic Materials*, 22(3):220–226, 1981.

[3] H Takagi, S Tsunashima, S Uchiyama, and T Fujii. Stress induced anisotropy in amorphous gd-fe and tb-fe sputtered films. *Journal of Applied Physics*, 50(B3):1642–1644, 1979.

[4] P Chaudhari, JJ Cuomo, and RJ Gambino. Amorphous metallic films for magneto-optic applications. *Applied Physics Letters*, 22(7):337–339, 1973.

[5] F Hellman and EM Gyorgy. Growth-induced magnetic anisotropy in amorphous tb-fe. *Physical review letters*, 68(9):1391, 1992.

[6] I Radu, K Vahaplar, C Stamm, T Kachel, N Pontius, HA Dürr, TA Ostler, J Barker, RFL Evans, RW Chantrell, et al. Transient ferromagnetic-like state mediating ultrafast reversal of antiferromagnetically coupled spins. *Nature*, 472(7342):205, 2011.

[7] Tian-Min Liu, Tianhan Wang, Alexander H Reid, Matteo Savoini, Xiaofei Wu, Benny Koene, Patrick Granitzka, Catherine E Graves, Daniel J Higley, Zhao Chen, et al. Nanoscale confinement of all-optical magnetic switching in

tbfeco-competition with nanoscale heterogeneity. *Nano letters*, 15(10):6862–6868, 2015.

[8] Ernst Meyer, Hans J. Hug, and Roland Bennewitz. *Scanning Probe Microscopy*. Springer Berlin, 2004.

[9] Y Martin and H Kumar Wickramasinghe. Magnetic imaging by âĂŸâĂŸ-force microscopyâĂŹâĂŹwith 1000 å resolution. *Applied Physics Letters*, 50(20):1455–1457, 1987.

[10] JJ Saenz, N_ Garcia, P Grütter, E Meyer, H Heinzelmann, R Wiesendanger, L Rosenthaler, HR Hidber, and H-J Güntherodt. Observation of magnetic forces by the atomic force microscope. *Journal of applied physics*, 62(10):4293–4295, 1987.

[11] Y Martin, D Rugar, and HK Wickramasinghe. High-resolution magnetic imaging of domains in tbfe by force microscopy. *Applied Physics Letters*, 52(3):244–246, 1988.

[12] P Grütter, E Meyer, H Heinzelmann, L Rosenthaler, H-R Hidber, and H-J Güntherodt. Application of atomic force microscopy to magnetic materials. *Journal of Vacuum Science & Technology A: Vacuum, Surfaces, and Films*, 6(2):279–282, 1988.

[13] D Rugar, H J Mamin, P Guethner, S E Lambert, J E Stern, I McFadyen, and T Yogi. Magnetic force microscopy: General principles and application to longitudinal recording media. *Journal Of Applied Physics*, 68(3):1169–16, 1990.

160

[14] C Schoenenberger, SF Alvarado, SE Lambert, and IL Sanders. Magnetic force microscopy and its application to longitudinal thin films. *Journal of Magnetism and Magnetic Materials*, 93:123–127, 1991.

[15] U Hartmann, T Göddenhenrich, and C Heiden. Magnetic force microscopy: Current status and future trends. *Journal of magnetism and magnetic materials*, 101(1-3):263–270, 1991.

[16] Peter Grütter, HJ Mamin, and D Rugar. Magnetic force microscopy (mfm). In *Scanning Tunneling Microscopy II*, pages 151–207. Springer, 1992.

[17] U Hartmann. Magnetic force microscopy. *Annual review of materials science*, 29(1):53–87, 1999.

[18] J Schwenk, M A Marioni, S Romer, N R Joshi, and Hans J Hug. Non-contact bimodal magnetic force microscopy. *Appl. Phys. Lett.*, 104(11):112412, March 2014.

[19] J Schwenk, X Zhao, M Bacani, M A Marioni, S Romer, and H J Hug. Bimodal magnetic force microscopy with capacitive tip-sample distance control. *Appl. Phys. Lett.*, 107:132407, 2015.

[20] Sascha Sadewasser and Thilo Glatzel, editors. *Kelvin Probe Force Microscopy*, volume 48 of *Springer Series in Surface Sciences*. Springer Berlin Heidelberg, Berlin, Heidelberg, 2012.

[21] M. Guggisberg, M. Bammerlin, Ch. Loppacher, O. Pfeiffer, A. Abdurixit, V. Barwich, R. Bennewitz, A. Baratoff, E. Meyer, and H.-J. GÃijntherodt. Separation of interactions by noncontact force microscopy. *Physical Review B*, 61(16):11151–11155, April 2000.

[22] Hans J Hug, B Stiefel, P. J. A van Schendel, A. Moser, R. Hofer, S. Martin, H. J. Güntherodt, Steffen Porthun, Leon Abelmann, J. C. Lodder, G. Bochi, and R. C. O,Handley. Quantitative magnetic force microscopy on perpendicularly magnetized samples. *J. Appl. Phys.*, 83(11):5609–5620, 1998.

[23] H-J Butt and Manfred Jaschke. Calculation of thermal noise in atomic force microscopy. *Nanotechnology*, 6(1):1, 1995.

[24] D Rugar, BC Stipe, HJ Mamin, CS Yannoni, TD Stowe, KY Yasumura, and TW Kenny. Adventures in attonewton force detection. *Applied Physics A: Materials Science & Processing*, 72(7):S3–S10, 2001.

[25] Johannes Schwenk. *Multi-modal and quantitative Magnetic Force Microscopy âĂŞ Application to Thin Film Systems with interfacial Dzyaloshinskii-Moriya Interaction*. PhD dissertation, Universit̃Ad̃ Basel, 2016.

[26] PJA van Schendel, H J Hug, B Stiefel, S Martin, and H-J Güntherodt. A method for the calibration of magnetic force microscopy tips. *J. Appl. Phys.*, 88(1):435–445, 2000.

[27] E De Castro and C Morandi. Registration of translated and rotated images using finite fourier transforms. *IEEE Transactions on pattern analysis and machine intelligence*, (5):700–703, 1987.

[28] A. Tikhonov. Solution of incorrectly formulated problems and the regularization method. In *Soviet Math. Doklady*, volume 4, pages 1035–1038, 1963.

[29] William H. Press, Saul A. Teukolsky, William T. Vetterling, and Brian P. Flannery. *Numerical Recipes 3rd Edition: The Art of Scientific Computing*. Cambridge University Press, New York, NY, USA, 3 edition, 2007.

[30] Dang Duc Trong, Cao Xuan Phuong, Truong Trung Tuyen, and Dinh Ngoc Thanh. TikhonovâĂŹs Regularization to the Deconvolution Problem. *Communications in Statistics - Theory and Methods*, 43(20):4384–4400, October 2014.

[31] Hans J Hug, B Stiefel, PJA Van Schendel, A Moser, S Martin, and H-J Güntherodt. A low temperature ultrahigh vaccum scanning force microscope. *Review of scientific instruments*, 70(9):3625–3640, 1999.

[32] H J Hug, A Moser, Th Jung, O Fritz, A Wadas, I Parashikov, and H J Güntherodt. Low temperature magnetic force microscopy. *Review Of Scientific Instruments*, 64(10):2920–7, 1993.

[33] Te-ho Wu. On the study of the magnetic domain pattern via the initial magnetization curve. *Journal of applied physics*, 81(8):5321–5323, 1997.

[34] X Zhao, J Schwenk, AO Mandru, M Penedo, M Baćani, MA Marioni, and HJ Hug. Magnetic force microscopy with frequency-modulated capacitive tip–sample distance control. *New Journal of Physics*, 20(1):013018, 2018.

[35] H J Mamin, D Rugar, J E Stern, B D Terris, and S E Lambert. Force microscopy of magnetization patterns in longitudinal recording media. *Applied Physics Letters*, 53(16):1563–4, 1988.

[36] Y MARTIN, D Rugar, and H K WICKRAMASINGHE. High-Resolution Magnetic Imaging of Domains in Tbfe by Force Microscopy. *Applied Physics Letters*, 52(3):244–246, 1988.

[37] S Porthun, L Abelmann, SJL Vellekoop, J C Lodder, and H J Hug. Opti-

mization of lateral resolution in magnetic force microscopy. *Applied Physics A-Materials Science & Processing*, 66:S1185–S1189, March 1998.

[38] Sumio Hosaka, Atsushi Kikukawa, Yukio Honda, and Hajime Koyanagi. Study of Magnetic Stray Field Measurement on Surface Using New Force Microscope. *Jpn. J. Appl. Phys.*, 31(Part 2, No. 7A):L908–L911, July 1992.

[39] R Giles, J P Cleveland, S Manne, P K Hansma, B Drake, P Maivald, C Boles, J Gurley, and V Elings. Noncontact force microscopy in liquids. *Appl. Phys. Lett.*, 63(5):617, 1993.

[40] I Schmid, M A Marioni, P Kappenberger, S Romer, M Parlinska-Wojtan, Hans J Hug, O Hellwig, M J Carey, and E E Fullerton. Exchange bias and domain evolution at 10 nm scales. *Phys. Rev. Lett.*, 105(19):197201–1–197201–4, November 2010.

[41] Andrea Benassi, Miguel A Marioni, Daniele Passerone, and Hans J Hug. Role of interface coupling inhomogeneity in domain evolution in exchange bias. *Sci. Rep.*, 4:4508–1–4508–7, 2014.

[42] B C Stipe, H J Mamin, T D Stowe, T W Kenny, and D Rugar. Magnetic Dissipation and Fluctuations in Individual Nanomagnets Measured by Ultrasensitive Cantilever Magnetometry. *Phys. Rev. Lett.*, 86(13):2874–2877, March 2001.

[43] S Rast, U Gysin, P Ruff, Ch Gerber, E Meyer, and D W Lee. Force microscopy experiments with ultrasensitive cantilevers. *Nanotechnology*, 17(7):S189–S194, March 2006.

[44] Y Liu and P Grütter. Magnetic dissipation force microscopy studies of magnetic materials. *J. Appl. Phys.*, 83(11):7333, 1998.

[45] http://www.zhinst.com/products/hf2li. We used a HF2LI Lock-in Amplifier from Zurich Instruments AG, Switzerland.

[46] T G Thomas and S C Sekhar. *Communication Theory.* Tata McGraw-Hill Publishing Company Limited, 2006.

[47] S Hudlet, M Saint Jean, C Guthmann, and J Berger. Evaluation of the capacitive force between an atomic force microscopy tip and a metallic surface. *EPJ B*, 2(1):5–10, March 1998.

[48] Hans J Hug, B Stiefel, P. J. A van Schendel, A. Moser, S. Martin, and H.-J. Güntherodt. A low temperature ultrahigh vaccum scanning force microscope. *Rev. Sci. Instrum.*, 70(9):3625–3640, 1999.

[49] C. D. Wright and E. W. Hill. Reciprocity in magnetic force microscopy. *Appl. Phys. Lett.*, 63(3):433–435, 1995.

[50] W B Zeper, F J A M Greidanus, P F Carcia, and C R Fincher. Perpendicular magnetic anisotropy and magneto-optical kerr effect of vapor-deposited co/pt-layered structures. *J. Appl. Phys.*, 65(12):4971–4975, 1989.

[51] S MANALIS, K Babcock, J MASSIE, V Elings, and M Dugas. Submicron Studies of Recording Media Using Thin-Film Magnetic Scanning Probes. *Applied Physics Letters*, 66(19):2585–2587, 1995.

[52] Roger Proksch, Erik Runge, Paul K Hansma, Sheryl Foss, and Brian Walsh. High field magnetic force microscopy. *Journal Of Applied Physics*, 78(5):3303–6, 1995.

[53] A Volodin, K Temst, C Van Haesendonck, and Y Bruynseraede. Observation of the Abrikosov vortex lattice in NbSe[sub 2] with magnetic force microscopy. *Applied Physics Letters*, 73(8):1134–4, 1998.

[54] Alexander Schwarz and Roland Wiesendanger. Magnetic sensitive force microscopy. *Nano Today*, 3(1-2):28–39, 2008.

[55] B D Belle, F Schedin, N Pilet, T V Ashworth, E W Hill, P W Nutter, H J Hug, and J J Miles. High resolution magnetic force microscopy study of e-beam lithography patterned Co/Pt nanodots. *Journal Of Applied Physics*, 101(9):09F517–3, May 2007.

[56] P Kappenberger, S Martin, Y Pellmont, H J Hug, J B Kortright, O Hellwig, and E E Fullerton. Direct imaging and determination of the uncompensated spin density in exchange-biased CoO/(CoPt) multilayers. *Physical Review Letters*, 91(26):267202, 2003.

[57] Casey Israel, Weida Wu, and Alex de Lozanne. High-field magnetic force microscopy as susceptibility imaging. *Applied Physics Letters*, 89(3):032502–3, July 2006.

[58] Weida Wu, Casey Israel, Namjung Hur, Soonyong Park, Sang-Wook Cheong, and Alex de Lozanne. Magnetic imaging of a supercooling glass transition in a weakly disordered ferromagnet. *Nature Materials*, 5(11):881–886, October 2006.

[59] P Kappenberger and I Schmid. Investigation of the exchange bias effect by quantitative magnetic force microscopy. *Advanced Engineering Materials*, 7:332–338, 2005.

[60] S. Okamoto, O. Kitakami, N. Kikuchi, T. Miyazaki, Y. Shimada, and Y. K. Takahashi. Size dependences of magnetic properties and switching behavior in FePt L10 nanoparticles. *Phys. Rev. B*, 67:094422–1–094422–7, 2003.

[61] S Romer, MA Marioni, K Thorwarth, NR Joshi, CE Corticelli, HJ Hug, S Oezer, M Parlinska-Wojtan, and H Rohrmann. Temperature dependence of large exchange-bias in tbfe-co/pt. *Applied Physics Letters*, 101(22):222404, 2012.

[62] C.-J. Lin, J. C. Suit, and R. H. Geiss. Micromagnetics of magnetization reversal in amorphous Tb-Fe films by lorentz microscopy . *J. Appl. Phys.*, 63(8):3835–3837, 1988.

[63] Neil Heiman, Kenneth Lee, Robert I Potter, JJ Becker, GH Lander, and JJ Rhyne. Exchange coupling in amorphous rare earth-iron alloys. In *AIP Conference Proceedings*, volume 29, pages 130–135. AIP, 1976.

[64] P Hansen, C Clausen, G Much, M Rosenkranz, and K Witter. Magnetic and magneto-optical properties of rare-earth transition-metal alloys containing gd, tb, fe, co. *Journal of applied physics*, 66(2):756–767, 1989.

[65] T Mizoguchi and GS Cargill III. Magnetic anisotropy from dipolar interactions in amorphous ferrimagnetic alloys. *Journal of Applied Physics*, 50(5):3570–3582, 1979.

[66] VG Harris, KD Aylesworth, BN Das, WT Elam, and NC Koon. Structural origins of magnetic anisotropy in sputtered amorphous tb-fe films. *Physical review letters*, 69(13):1939, 1992.

[67] Vincent G Harris and Taras Pokhil. Selective-resputtering-induced perpendicular magnetic anisotropy in amorphous tbfe films. *Physical review letters*, 87(6):067207, 2001.

[68] Naoki Nishimura, Tadahiko Hirai, Akio Koganei, Takashi Ikeda, Kazuhisa Okano, Yoshinobu Sekiguchi, and Yoshiyuki Osada. Magnetic tunnel junction device with perpendicular magnetization films for high-density magnetic random access memory. *Journal of applied physics*, 91(8):5246–5249, 2002.

[69] A Canizo Cabrera, Che-Hao Chang, Chih-Cheng Hsu, Ming-Chi Weng, CC Chen, CT Chao, Jong-Ching Wu, Yang-Hua Chang, and Te-Ho Wu. Perpendicular magnetic tunneling junction with double barrier layers for mram application. *IEEE transactions on magnetics*, 43(2):914–916, 2007.

[70] Lin-Xiu Ye, Ching-Ming Lee, Jia-Hol Lai, Alberto Canizo-Cabrera, Wen-Jauh Chen, and Te-ho Wu. Magnetic properties of mgo-based re-tm perpendicular magnetic tunnel junctions. *Journal of Magnetism and Magnetic Materials*, 322(7):L9–L11, 2010.

[71] DI Paul. Extended theory of the coercive force due to domain wall pinning. *Journal of Applied Physics*, 53(3):2362–2364, 1982.

[72] Dieter Suess, Josef Fidler, Karina Porath, Thomas Schrefl, and Dieter Weller. Micromagnetic study of pinning behavior in percolated media. *Journal of applied physics*, 99(8):08G905, 2006.

[73] CE Graves, AH Reid, T Wang, B Wu, S De Jong, K Vahaplar, I Radu, DP Bernstein, M Messerschmidt, L Müller, et al. Nanoscale spin reversal by

non-local angular momentum transfer following ultrafast laser excitation in ferrimagnetic gdfeco. *Nature materials*, 12(4):293–298, 2013.

[74] Harald Oezelt, Alexander Kovacs, Franz Reichel, Johann Fischbacher, Simon Bance, Markus Gusenbauer, Christian Schubert, Manfred Albrecht, and Thomas Schrefl. Micromagnetic simulation of exchange coupled ferri-/ferromagnetic heterostructures. *Journal of magnetism and magnetic materials*, 381:28–33, 2015.

[75] Birgit Hebler, Alexander Hassdenteufel, Patrick Reinhardt, Helmut Karl, and Manfred Albrecht. Ferrimagnetic tb–fe alloy thin films: Composition and thickness dependence of magnetic properties and all-optical switching. *Frontiers in Materials*, 3:8, 2016.

[76] I Schmid, MA Marioni, P Kappenberger, S Romer, M Parlinska-Wojtan, HJ Hug, O Hellwig, MJ Carey, and EE Fullerton. Exchange bias and domain evolution at 10 nm scales. *Physical review letters*, 105(19):197201, 2010.

[77] M Mansuripur. Magnetization reversal, coercivity, and the process of thermomagnetic recording in thin films of amorphous rare earth–transition metal alloys. *Journal of applied physics*, 61(4):1580–1587, 1987.

[78] Robert C O'handley. *Modern magnetic materials: principles and applications*. Wiley, 2000.

[79] JOHN MICHAEL DAVID Coey. Amorphous magnetic order. *Journal of Applied Physics*, 49(3):1646–1652, 1978.

[80] SM Watson, T Hauet, JA Borchers, S Mangin, and EE Fullerton. Interfacial

magnetic domain wall formation in perpendicular-anisotropy, exchange-spring films. *Applied Physics Letters*, 92(20):202507, 2008.

[81] Josep Nogués and Ivan K Schuller. Exchange bias. *Journal of Magnetism and Magnetic Materials*, 192(2):203–232, 1999.

[82] Andrea Benassi, Miguel A Marioni, Daniele Passerone, and Hans J Hug. Role of interface coupling inhomogeneity in domain evolution in exchange bias. *Scientific reports*, 4, 2014.

[83] M Aeschlimann, GL Bona, F Meier, M Stampanoni, A Vaterlaus, HC Siegmann, EE Marinero, and H Notarys. Exchange coupling of contacted ferromagnetic films: Fe on amorphous tbfe. *IEEE Transactions on Magnetics*, 24(6):3180–3184, 1988.

[84] S Mangin, G Marchal, C Bellouard, W Wernsdorfer, and B Barbara. Magnetic behavior and resistivity of the domain-wall junction gdfe (1000 å)/tbfe/gdfe (500 å). *Physical Review B*, 58(5):2748, 1998.

[85] S Mangin, G Marchal, and B Barbara. Evidence of exchange-bias-like phenomenon in gdfe/tbfe/gdfe domain wall junctions. *Physical review letters*, 82(21):4336, 1999.

[86] F Canet, S Mangin, C Bellouard, M Piécuch, and A Schuhl. Exchange bias phenomena in ferrimagnetic based bilayers. *Journal of Applied Physics*, 89(11):6916–6918, 2001.

[87] D Mauri, HC Siegmann, PS Bagus, and E Kay. Simple model for thin ferromagnetic films exchange coupled to an antiferromagnetic substrate. *Journal of Applied Physics*, 62(7):3047–3049, 1987.

[88] AP Malozemoff. Random-field model of exchange anisotropy at rough ferromagnetic-antiferromagnetic interfaces. *Physical review B*, 35(7):3679, 1987.

[89] S Mangin, C Bellouard, S Andrieu, F Montaigne, P Ohresser, NB Brookes, and B Barbara. Magnetization reversal in exchange-coupled gdfe/tbfe studied by x-ray magnetic circular dichroism. *Physical Review B*, 70(1):014401, 2004.

[90] J McCord, Y Henry, Thomas Hauet, F Montaigne, Eric E Fullerton, and S Mangin. Mechanism of chirality reversal for planar interface domain walls in exchange-coupled hard/soft magnetic bilayers. *Physical Review B*, 78(9):094417, 2008.

[91] Chao-Cheng Lin, Chih-Huang Lai, Ruo-Fan Jiang, and Han-Ping D Shieh. High interfacial exchange energy in tbfeco exchange-bias films. *Journal of applied physics*, 93(10):6832–6834, 2003.

[92] Chih-Huang Lai, Zhi-Hao Wu, Chao-Cheng Lin, and PH Huang. Thermally assisted-writing giant magnetoresistance with perpendicular magnetization. *Journal of applied physics*, 97(10):10C511, 2005.

[93] K Bussmann, GA Prinz, S-F Cheng, and D Wang. Switching of vertical giant magnetoresistance devices by current through the device. *Applied physics letters*, 75(16):2476–2478, 1999.

[94] S Mangin, D Ravelosona, JA Katine, MJ Carey, BD Terris, and Eric E Fullerton. Current-induced magnetization reversal in nanopillars with perpendicular anisotropy. *Nature Materials*, 5(3):210–215, 2006.

[95] F Garcia, J Sort, B Rodmacq, S Auffret, and B Dieny. Large anomalous enhancement of perpendicular exchange bias by introduction of a nonmagnetic spacer between the ferromagnetic and antiferromagnetic layers. *Applied physics letters*, 83(17):3537–3539, 2003.

[96] KC Schuermann, JD Dutson, SZ Wu, SD Harkness, B Valcu, H-J Richter, RW Chantrell, and K OâĂŹGrady. Exchange-coupling effects in perpendicular composite materials. *Journal of applied physics*, 99(8):08Q904, 2006.

[97] A Berger, N Supper, Y Ikeda, B Lengsfield, A Moser, and EE Fullerton. Improved media performance in optimally coupled exchange spring layer media. *Applied Physics Letters*, 93(12):122502, 2008.

[98] F Radu, R Abrudan, I Radu, D Schmitz, and H Zabel. Perpendicular exchange bias in ferrimagnetic spin valves. *Nature communications*, 3:715, 2012.

[99] MH Tang, Zongzhi Zhang, SY Tian, J Wang, B Ma, and QY Jin. Interfacial exchange coupling and magnetization reversal in perpendicular [co/ni]n/tbco composite structures. *Scientific reports*, 5, 2015.

Acronyms

LCF lever-canting-Function.

TF transfer function.

S1 TbFe thin film.

S2 TbFe/[Co/Pt]$_{\times 5}$.

S3 TbFe/Pt$_{0.4nm}$/[Co/Pt]$_{\times 5}$.

S4 TbFe/Pt$_{0.7nm}$/[Co/Pt]$_{\times 5}$.

S5 TbFe/Pt$_{1.2nm}$/[Co/Pt]$_{\times 5}$.

S6 TbFe/Pt$_{2.0nm}$/[Co/Pt]$_{\times 5}$.

S7 TbFe/Pt$_{2.5nm}$/[Co/Pt]$_{\times 5}$.

AFM atomic force microscopy.

a-TbFe amorphous TbFe ferrimagnets.

AF antiferromagnet.

ASA atomic-scale structural anisotropy.

BPM bit-patterned media.

CP contact potential.

CPD contact potential difference.

DAC digital-to-analog converter.

DM Dzyaloshinskii-Moriya.

DW domain wall.

ECDLs exchange-coupled double layers.

EDX energy dispersive X-ray analysis.

F ferromagnet.

Fi ferrimagnet.

FIB focused ion beam.

GMR giant magnetoresistance.

HAMR heat-assisted magnetic recording.

iDW interfacial domain walls.

KPFM Kelvin potential force microscopy.

LT-MFM low temperature magnetic force microscope.

MFM magnetic force microscope.

ML monolayers.

NM noble metal.

PEEM photoemission electron microscopy.

p-MTJ perpendicular tunnel junction.

PLL phase-locked loop.

PMA perpendicular magnetic anisotropy.

PSD position sensitive photodetector.

pUCS pinned uncompensated spins.

Q quality factor.

RBS Rutherford backscattering spectrometry.

RE rare earth.

SFM scanning force microscope.

SNR signal-to-noise ratio.

SQUID superconducting quantum interference device.

STM scanning tunneling microscopy.

STXM scanning transmission X-ray microscopy.

TEM transmission electron microscopy.

TEM transmission electron microscopy.

TM transition metal.

TMR tunneling magnetoresistance.

UHV ultra high vacuum.

VSM vibrating sample magnetometry.

XMCD X-ray Magnetic Circular Dichroism.

XRD X-ray diffractometry.

XRR X-ray reflectometry.

List of publications

- Zhao, X and Schwenk, J and Mandru, AO and Penedo, M Baćani, M and Marioni, MA and Hug, HJ
  Magnetic force microscopy with frequency-modulated capacitive tip–sample distance control
  New Journal of Physics 20 013018 (2018) doi:10.1088/1367-2630/aa9ca9

- J. Schwenk, X. Zhao, M. Baćani, M. A. Marioni, S. Romer, H. J. Hug
  Bimodal Magnetic Force Microscopy with Capacitive Tip-Sample Distance Control
  Applied Physics Letters 107(13) (2015) doi:10.1063/1.4932174

- P. Urwyler, X. Zhao, A. Pascual, H. Schift, B. Müller
  Tailoring surface nanostructures on polyaryletherketones for load-bearing implants
  European Journal of Nanomedicine, 6(1): 37-46, (2014) doi: 10.1515/ejnm-2014-0006

- P. Urwyler, X. Zhao, A. Pascual
  Comparing physical properties of PEKK and PEEK
  European cells and materials, 26 (Suppl. 4): 14-14, (2013) doi: 10.7892/boris.48939

- F. M. Weiss, X. Zhao, G. Kovacs, B. Müller
  Measuring the bending of asymmetric planar EAP structures
  Proc. SPIE 8687, Electroactive Polymer Actuators and Devices (EAPAD), 86871X (2013) doi: 10.1117/12.2009355

176

- X. Zhao, P. Urwyler, B. Müller

  Optimization of the optical readout of PEEK cantilevers

  European Cells and Materials, 23 (2), 40, (2012)

Xue ZHAO

Winterthurerstrasse 495, 8051 Zürich
+41 78 862 99 18
Born on 11th Jan.1988, Chinese

Education

2013-2017   Ph.D. in Experimental Physics, University of Basel
Thesis: "Magnetization reversal mechanism in strongly exchange coupled double layers of Co/Pt and TbFe"

2010-2013   M.Sc. in Physics, ETH Zürich
Thesis: "Cantilever-based sensing to quantify materials-cells interactions"

2006-2010   B.Sc. in Physics, joint B.Sc. program
- 2008-2010   Université Claude Bernard Lyon 1, France
- 2006-2008   Wuhan University, China

Professional Experience

12.2017-present   Postdoctoral Research Scientist, EMPA
- Fabricating and characterizing magnetic multilayer systems
- Simulating and modelling data by Matlab
- Collaborating with other universities and institutes in multiple projects on magnetic thin films
- Documenting and presenting research results
- Training incoming students and research staff

06.2013-11.2017   Associate Research Scientist, EMPA
- Fabricating magnetic thin films with ultra-high-vacuum DC magnetron sputtering
- Characterizing sample properties using quantitative magnetic force microscopy, atomic force microscopy (AFM), and physical property measurement system (PPMS)
- Processing acquired experimental data by Matlab
- Installing home-built ultra-high-vacuum low-temperature magnetic force microscope (MFM)
- Updating electronic systems such as lock-in amplifier and temperature controller
- Implementing and debugging of the scanning control software
- Developing techniques to overcome measurement limitations

10.2011-12.2011   Research Assistant, PSI
- Coating metallic layers onto polymer films by evaporation
- Characterizing Ultra-Violet-Ozone treated polymer films
- Reproducing line patterns on polymer films by hot embossing in a cleanroom environment

Languages

Chinese   Native language
English   Full professional proficiency
German   Professional working proficiency
French   Professional working proficiency

Laboratory Skills

- Expertise in DC magnetron sputtering, magnetic force microscopy (MFM), atomic force microscopy (AFM), vibrating sample magnetometry (VSM)
- Experience in electron beam evaporation, electrochemical etching, mass spectrometry, X-ray reflectometry (XRR), X-ray diffractometry (XRD), hot embossing, plasma treatment, ozone treatment
- Knowledge in superconducting quantum interference device magnetometry (SQUID), Rutherford backscattering spectrometry (RBS), scanning transmission electron microscopy (STEM), X-ray magnetic circular dichroism (XMCD)

IT Skills

Matlab, Mathematica, Python, LabView, C++
Microsoft Office, LaTeX, Adobe Illustrator, Origin, WSxM, NanoScope
Analysis